

Vibrational Stark Spectroscopy as a Tool for Probing Electrostatics at Protein Surfaces and Self Assembled Monolayers

vorgelegt von
Master of Science – Chemistry

Gal Schkolnik

Von der Fakultät II – Mathematik und Naturwissenschaften
der Technischen Universität Berlin
zur Erlangung des akademischen Grades

Doktor der Naturwissenschaften
Dr. rer. nat.

genehmigte Dissertation

Promotionsausschuss:
Vorsitzender: Prof. Dr. Roderich Süßmuth
Berichter: Prof. Dr. Peter Hildebrandt
Berichter: Prof. Dr. Stefan Franzen

Tag der wissenschaftlichen Aussprache: 15. Oktober 2012

Berlin 2012
D 83

I would like to dedicate this work to five women who have shaped me and brought me to where I today stand:

Neomi my mother, who has brought me to this confusing world and gave me the freedom to find my way in it and the support to pursue it; Java, an admirable woman who was as a grandmother to me, and who lovingly taught me how to find beauty in nature and be soulful, stubborn and insistent; Tova, my second mother and life-long confidant, who tried to teach me manners but had to do with my studiousness instead; Dvori, my high-school Chemistry teacher who has been doomed to reading my papers since the days when she gave me support, advice and encouragement in and after class; and Tova, my first ever Chemistry teacher from Junior High, who taught us how to fill atomic sub-orbitals in eighth grade, thus casting a lasting spell on my young heart that still lingers.

Real courage is moving forward
when the outcome is uncertain.

Table of contents

Abstract	II
Zusammenfassung	III
List of publications	V
List of abbreviations	VI
Symbols	VII
Physical constants	IX
1. Introduction	1
1.1 The Vibrational Stark effect – please disentangle before use!.....	2
1.2 Probing electric fields on protein surfaces – Outside looking in	3
1.3 Become the arrow – MBN-containing SAMs to elucidate SAM electrostatics.....	4
2. Theoretical Background	7
2.1 Self Assembled Monolayers (SAM).....	8
2.1.1 The tilt angle θ	10
2.1.2 Changes to the potential of zero charge (E_{pzc}) due to SAM coating	12
2.1.3 Electrostatic model of the electric field at the SAM/solution interface.....	15
2.2 Heme proteins	19
2.2.1 Cytochrome <i>c</i>	19
2.2.2 Dehaloperoxidase-hemoglobin A.....	23
2.2.3 Enzyme kinetics	25
2.2.3.1 DHP A kinetics	27
2.3 UV/Visible spectroscopy	28
2.4 Cyclic voltammetry	29
2.5 Vibrational spectroscopy	31
2.5.1 The harmonic oscillator – classical model.....	31
2.5.2 The harmonic oscillator – quantum model	32

2.5.2 FTIR spectroscopy	34
2.5.3 FTIR in ATR mode	35
2.5.4 Surface Enhanced IR Absorption (SEIRA) spectroscopy	37
2.5.4.1 Surface selection rule.....	38
2.5.4.2 Chemical enhancement.....	39
2.5.4.3 The electromagnetic mechanism	40
2.5.5 Surface Enhanced Raman Spectroscopy (SERS)	42
2.6 The Vibrational Stark Effect.....	43
2.6.1 Sensitivities of the nitrile stretch	45
2.6.1.1 The nitrile tuning rate	45
2.6.1.2 Phase and solvent effects	46
3. Materials and Methods	49
3.1 FTIR	50
3.1.1 For Cytochrome c	50
3.1.2 For Dehaloperoxidase (DHP) and the Stark label in solution	50
3.2 Spectro-electrochemistry in a Surface Enhanced IR Absorption (SEIRA) setup.....	51
3.2.1 SEIRA setup	51
3.2.2 Gold film deposition	53
3.2.3 Gold film electrochemical cleaning	54
3.2.4 SAM coating and protein adsorption	55
3.2.5 Cyclic Voltammetry in the SEIRA cell	56
3.2.6 Redox titration of Cyt-c in the SEIRA cell.....	57
3.2.7 Data analysis	57
3.3 DHP production and purification.....	57
3.3.1 Protein growth	57
3.3.2 Purification of 6XHisDHP	58
3.4 Labeling with 4-mercaptobenzonitrile (MBN)	59
3.4.1 Labeling of NACME with MBN and measurement of free and NACME-attached MBN in different fractions of buffer:DMSO	59

3.3.2 Protein labeling with MBN.....	59
3.5 Surface enhanced Raman Spectroscopy in a spectro-electrochemical cell	60
3.6 Molecular dynamics simulations.....	60
4. Results and Discussion	61
4.1 The Stark tuning rate and ν_0 in free and protein-bound water exposed MBN	62
4.2 Using the Stark effect to probe electric fields on the surface of Cytochrome c variants in solution and at a SAM surface.....	65
4.2.1 Cyt-c-MBN in solution.....	67
4.2.2 Cyt-c-MBN at SAM.....	68
4.3 The vibrational Stark effect of MBN as a tool for understanding the electrostatics of metal/SAM/solution interfaces	73
4.3.1 Formation of MBN-SAM on Au electrodes.....	73
4.3.2 Thiophenol:MBN mixed SAM preparation	76
4.3.3 MHA:MBN mixed SAM preparation.....	78
4.3.4 Solvent effects on the nitrile stretching modes in an MBN-SAM on Ag and Au.....	78
4.3.5 The nitrile stretching frequency in MBN-SAMs on Ag and Au under a series of applied potentials	80
4.3.6 The MBN nitrile stretching frequency in mixed SAMs on Au electrodes, under a series of applied potentials	81
4.3.7 Factors controlling the zero-field nitrile stretching frequency.....	84
4.3.8 Electrostatic model.....	87
4.3.9 The effective potential of zero charge	91
4.4 Catalytic efficiency of Dehaloperoxidase A is controlled by electrostatics – the vibrational Stark effect as a tool for understanding enzyme kinetics.....	94
4.4.1 FTIR spectra of MBN-labeled mutant and wild type DHP A.....	94
4.4.2 Connecting VSE and kinetic findings in DHP A.....	102
5. Conclusion	105
Acknowledgements	109
Bibliography	110

Abstract

The vibrational Stark effect (VSE) consists of a shift in the frequency of certain vibrational modes due to exposure to local electric fields. In the cases treated here, the electric-field dependent variation of the frequency can be considered to be linear. The CN stretching frequency of aromatic nitriles are particularly sensitive to electric fields, and so 4-mercaptobenzonitrile (MBN) has been chosen as a spectroscopic electric field probe for several systems in this work. After various nitrile Stark probes have been recently employed to investigate electric fields in the active sites of proteins and enzymes as well as conformational changes in proteins, in this work the electric fields at protein surfaces were probed by IR and surface enhanced IR absorption (SEIRA) spectroscopy, using a Stark label covalently bound to solution-exposed cysteine residues. In this way, it could be demonstrated that for double-function protein dehaloperoxidase-hemoglobin A charge mutations in the vicinity of the active site affected the global electrostatics of the protein, which in turn is the crucial parameter controlling substrate binding. This was reflected by a linear correlation between the mutation-induced Stark shift of the remote MBN label and the catalytic efficiency of the enzyme. In cytochrome *c*, the nitrile vibrational frequency of MBN-labeled cytochrome *c* mutants was measured both in solution and when bound to a self assembled monolayer (SAM) on an Au surface. Thus the electric field variation on the protein surface could be estimated, providing insight into the electrostatics in the protein/SAM/electrode interfaces. It is shown that the local electric field experienced by the protein in the diffuse double layer does not decay exponentially with the distance from the SAM surface. Further, pure and mixed SAMs of MBN were formed on Au and Ag electrodes in spectro-electrochemical setups, to study the electrostatics of different types of metal/SAM/solvent interfaces. In this way we could sort out the effect of solvent and hydrogen bonding interactions as well as the interfacial electric field. Potential-dependent measurements of the Stark shift were analyzed on the basis of an improved electrostatic model to relate the experimentally determined frequencies with the electric field on the SAM surfaces. The analysis also affords the effective potential of zero charge, a parameter that is very difficult to estimate using other techniques.

Zusammenfassung

Der Schwingungs-Stark-Effekt (VSE) führt zu einer Verschiebung der Frequenz bestimmter Schwingungsmoden aufgrund von Veränderungen des lokalen elektrischen Feldes. In den hier betrachteten Fällen kann die Änderung der Frequenzen mit der elektrischen Feldstärke als linear angesehen werden. Da die Frequenz der CN Streckschwingung aromatischer Nitrile besonders empfindlich auf die Veränderung des elektrischen Feldes reagiert, wurde in dieser Arbeit 4-Mercaptobenzonitril (MBN) als spektroskopische Sonde für das elektrische Feld verwendet. In letzter Zeit sind verschiedene Nitril Stark-Sonden zum Einsatz gekommen, um elektrische Felder und Konformationsänderungen in aktiven Zentren von Proteinen und Enzymen zu untersuchen. In der vorliegenden Arbeit wurden elektrische Felder an Proteinoberflächen mit IR und oberflächen-verstärkter IR Absorptions (SEIRA) Spektroskopie erforscht. Hierzu wurden Stark-Sonden kovalent an Cysteingruppen gebunden, die der Lösung zugänglich sind. So konnte für das Protein Dehaloperoxidase-Hämoglobin A gezeigt werden, dass Ladungsmutationen in der Umgebung des aktiven Zentrums die Elektrostatik des gesamten Proteins beeinflussen. Diese ist wiederum der entscheidende Parameter, um die Substratbindung zu kontrollieren. Es wurde eine lineare Korrelation zwischen der Mutations-induzierten Stark-Verschiebung der weit entfernten MBN-Sonde und der katalytischen Effektivität des Enzyms gefunden. Weitere Untersuchungen des VSE wurden mit MBN-markierten Cytochrom c Mutanten durchgeführt, sowohl an den Proteinen in Lösung als auch nach Immobilisierung auf Goldoberflächen, die zuvor mit selbstorganisierten Monolagen (SAM) beschichtet wurden. Dadurch konnten die auf die Proteinoberfläche wirkenden Veränderungen des elektrischen Feldes abgeschätzt werden, was das Verständnis der elektrostatischen Wechselwirkungen in den Protein/SAM/Elektrode Grenzflächen fördert. Es wurde gezeigt, dass das vom Protein wahrgenommene elektrische Feld in der diffusen Doppelschicht nicht exponentiell mit dem Abstand von der SAM-Oberfläche abnimmt. Die Elektrostatik von verschiedenen Metal/SAM/Lösungsmittel Systemen wurden an reinen und gemischten MBN-SAMs auf Gold- und Ag-Elektroden spektroelektrochemisch untersucht. So konnte zwischen Lösungsmittel- und Wasserstoffbrücken-Effekten auf die Nitril-Streckschwingungsfrequenz einerseits und

den Effekt des elektrischen Feldes in der Grenzschicht andererseits differenziert werden. Um die experimentell gefundenen Frequenzen mit dem elektrischen Feld auf der SAM-Oberfläche zu korrelieren, wurden Potential-abhängige Messungen der Stark-Verschiebung auf der Basis eines verbesserten elektrostatischen Modells analysiert. Diese Untersuchung lieferte zudem Werte für das effektive Potential der Nullladung, ein Parameter, der nur sehr schwer mit anderen Techniken zu bestimmen ist.

List of publications

Schkolnik, G., Salewski, J., Millo, D., Zebger, I., Franzen, S. and Hildebrandt, P. Vibrational Stark effect in the electric-field reporter 4-mercaptobenzonitrile as a tool for investigating SAM electrostatics, *Int. J. Mol. Sci.*, **13**, 7466-7482 (2012)

Schkolnik, G., Utesch, T., Salewski, J., Tenger, K., Millo, D., Kranich, A., Zebger, I., Schulz, C., Zimányi, L., Rákhely, G., Mroginski, M.A. and Hildebrandt, P. Mapping local electric fields in proteins at biomimetic interfaces, *Chem. Commun.*, **48**, 70-72 (2012)

List of abbreviations

Ag	Silver
ATR	Attenuated Total Reflectance
Au	Gold
BD	Bond dipole
CE	Counter electrode
CV	Cyclic Voltammetry or cyclic voltammogram
Cyt-c	Cytochrome <i>c</i>
DBQ	Dibromoquinone
DHP A	Dehaloperoxidase hemoglobyn A
DMSO	Dimethyl sulfoxide
FTIR	Fourier Transform IR
IR	Infrared
IR-RAS	Infrared reflection absorption spectroscopy
KPB	Potassium phosphate buffer
MBN	4-mercaptobenzonitrile
MCT	Mercury cadmium telluride
Me-THF	Methyl-tetrahydrofuran
MHA	6-mercaptohexanoic acid
NACME	N-acetyl- <i>L</i> -cysteine-methyl-ester
NCSU	North Carolina State University
NEXAFS	Near Edge X-ray Absorption Fine Structure
OPD	Optical path difference
RE	Reference electrode
RI	Refractive index
rmsf	Root mean square fluctuation
SAM	Self assembled monolayer
SEIRA	Surface enhanced IR absorption
SERS	Surface enhanced Raman spectroscopy
STM	Scanning tunneling microscope
TBP	2,4,6-tribromophenol
TP	Thiophenol
UV/Vis	Ultraviolet/visible spectroscopy
VSE	Vibrational Stark Effect
WE	Working electrode
WT	Wild type

Symbols

Symbol	Units	Significance
a	$C \cdot m^2 \cdot V^{-1}$	Polarizability
Δa	$C \cdot m^2 \cdot V^{-1}$	Difference polarizability
A	m^2	Area (unit cell, equivalent capacitor, working electrode)
A	unitless	Light absorption
B_{nm}	unitless	Transition probability
β	Degrees	Angle between molecular dipole and the surface normal
c	M	Concentration
C	F/cm^2	Capacity
C_{dl}	F/cm^2	Area-specific capacitance of the double layer
Γ	mol/m^2	Surface concentration of analyte
d	m	distance
d_c	m	SAM thickness
d_p	m	Penetration length
δ	m	Optical retardation
E	V	Electric potential
E_0	V	Effective potential of zero charge of SAM-coated metal
E^0	V	Formal Redox potential under specific conditions
E_a	V	Anodic peak position
E_c	V	Cathodic peak position
E_{pzc}	V	Potential of zero charge of bare metal
\vec{E}_F	V/m	Electric field
\vec{F}	V/m	Electric field
$\epsilon(\bar{\nu})$	$L \cdot mol^{-1} \cdot cm^{-1}$	Molar absorptivity
ϵ_c	unitless	Dielectric constant of SAM
ϵ_s	unitless	Dielectric constant of solution
Φ_{ref}	V	Reference electrode potential
I	mol/L	Ionic strength
I	Amp	Current
I	W/m^2	Transmitted light intensity
I_0	W/m^2	Source light intensity
I_{dl}	Amp	Capacitive current
λ	nm	Light wavelength
k	N/m	Spring constant
k_{cat}	s^{-1}	Number of substrate molecule turned over by enzyme per second
k_{cat}/K_M	s/M	Catalytic efficiency
k_i	Varies	Reaction rate constant for reaction i
k_i	unitless	Imaginary component of the refractive index of medium i
K_m	M	Michaelis-Menten constant

κ	m^{-1}	Reciprocal Debye length
l	m	Distance, optical path
μ	D	Dipole moment
μ_{\perp}	D	SAM dipole moment component perpendicular to surface
$\Delta\vec{\mu}$	$cm^{-1}/V/m$	Difference dipole or Stark tuning rate
n_i	unitless	Real component of the refractive index of medium i
ν	cm^{-1}	Vibrational frequency
ν	V/s	Scan rate
ν	unitless	Vibrational level
ν_0	cm^{-1}	Vibrational frequency in the absence of an electric field
p	D	Molecular dipole of SAM monomer
p_0	D	Molecular dipole of SAM monomer in the gas phase
q	C	Charge
R_s	W	Reflected intensity of s-polarized light
R_s	W	Reflected intensity of p-polarized light
R_k^{nm}	Cm	Transition dipole moment for transition from state m to state n
σ_0	C/m^2	Charge density at the SAM surface at $E=E_{pzc}$
σ_M	C/m^2	Charge density at the metal surface
σ_c	C/m^2	Charge density at the SAM surface
σ_s	C/m^2	Charge density at the bulk solution
T	Kelvin	Temperature
T	unitless	Transmission
θ	degrees	SAM tilt angle
θ	degrees	Angle of incidence
V_0	M/s	Initial reaction velocity
V_{max}	M/s	Maximal reaction velocity
ΔV_{vac}	eV	Potential difference across the dipolar SAM
Φ	eV	Work function
Φ_c	V	Potential at the SAM surface
Φ_M	V	Potential at the metal surface
Φ_s	V	Potential in the bulk solution
Φ_x	V	Potential at distance x from SAM surface
$\Delta\Phi$	eV	Change to work function due to SAM-coating
Ψ_m	$m^{-3/2}$	Wave function of state m
ω	rad/s	Angular frequency
x	m	Distance, displacement
z	unitless	Number of charges

Physical constants

Symbol	Significance	Value
ϵ_0	Permittivity of free space	$8.854187817 \times 10^{-12} \text{ C}^2/\text{Nm}^2$
e	Elementary charge	$1.60217646 \times 10^{-19} \text{ C}$
h	The Planck constant	$6.6261 \times 10^{-34} \text{ J s}$
k or k_B	Boltzmann constant	$1.3806503 \times 10^{-23} \text{ J K}^{-1}$
N_a	Avogadro number	$6.0221415 \times 10^{23} \text{ mol}^{-1}$

Introduction

1.1 The Vibrational Stark effect – please disentangle before use!

The vibrational Stark effect (VSE) has been slowly gaining importance as a tool for indirectly quantifying electric fields and describing their effect on systems that are either too small, too complex or too isotropic to be subjected to direct electric field measurements. VSE is described by the following equation:

$$(1.1.1) \quad \nu = \nu_0 - \Delta\vec{\mu} \cdot \vec{F} - \frac{1}{2}\vec{F} \cdot \Delta\vec{\alpha} \cdot \vec{F}$$

where ν and ν_0 are the vibrational frequencies of a certain vibrational mode in the presence and in the absence of an electric field F , respectively, $\Delta\mu$ is the difference dipole moment of the mode, also known as the Stark tuning rate, and $\Delta\alpha$ is its difference polarizability (Andrews & Boxer 2000a; Steven G. Boxer 2009). For many cases, the linear term has been shown to suffice (Schkolnik, Salewski, et al. 2012; Fafarman et al. 2012; Suydam & Steven G Boxer 2003), providing a potentially powerful tool for indirect electric field measurements: if a probe molecule bearing a functionality with an electric-field sensitive vibrational mode can be introduced into the system of interest without causing significant perturbation, and assuming that we know the tuning rate and the vibrational frequency of that particular vibrational mode in the absence of an electric field, then by measuring the vibrational frequency of the mode while exposed to the system of interest, we should be able to quantify the electric field that our Stark probe functionality is exposed to.

Alas, the situation is always more complex than it seems. Even if our first assumption is true, and the system of interest is not perturbed by the addition of a Stark probe molecule, which can be verified spectroscopically, electrochemically or by molecular dynamics simulations, there is still the question of how $\Delta\mu$ and ν_0 are affected by factors other than the electric field. As the electric-field sensitive modes show a Stark effect exactly because they are polarizable (Reimers & Hush 1999; Brewer & S. Franzen 2003), their vibrational frequency, as well as its sensitivity to electric fields, may be affected by the kind of substrate the probe molecule is attached to (Schkolnik, Salewski, et al. 2012), by the depolarizing effect of neighboring molecules (Aschaffenburg & Moog 2009; Levinson et al. 2012) and by hydrogen bonding interactions (Aschaffenburg & Moog

2009; Ghosh et al. 2009; Fafarman et al. 2010; Fafarman et al. 2012; Levinson et al. 2012). Thus in order to be able to quantify electric fields by measuring the vibrational frequency of a Stark probe, one must first take into account the effect that its immediate environment might have on the “invariables” of the VSE equations (Eq. 1.1.1). In this work, this question is addressed for the Stark probe molecule we employ, 4-mercaptobenzonitrile (MBN), which in the systems that we investigate is water-exposed and bound to protein surfaces, or alternatively embedded in a self assembled monolayer (SAM) on a noble metal substrate.

1.2 Probing electric fields on protein surfaces – Outside looking in

Stark probes have been increasingly used to probe electric fields inside the active site of proteins, either by covalently binding the Stark probe, integrating nitrile-containing artificial amino-acids, or introducing a nitrile-functionalized inhibitor (Fafarman et al. 2012; Fafarman & Boxer 2010; Suydam et al. 2006; Xu et al. 2011). While this kind of information is very helpful for the understanding of local mechanisms in the active site, in order to examine mechanisms involving overall protein electrostatics or to probe electrostatics in the environment of the protein (Tucker et al. 2004), the Stark probe must be attached to the protein surface. In this work we attach MBN to cytochrome *c* (Cyt-*c*) mutants (Schkolnik, Utesch, et al. 2012) and to dehaloperoxidase-hemoglobin A (DHP A) variants. In the latter case, we covalently bind MBN to a surface cysteine naturally occurring on the surface of this double-function globin-peroxidase enzyme and of its single charge mutants, and find that MBN can sense single charge changes across the protein, and that indeed it senses changes to overall protein electrostatics, affecting kinetic efficiency of this diffusion-controlled enzyme (Ma et al. 2010). For Cyt-*c*, an electron shuttle involved in mitochondrial respiration, we covalently bind MBN in two different positions to which a surface cysteine has been introduced by site-directed mutagenesis, and measure the difference electric field in the nitrile bond direction across the protein. As we attach the protein to a SAM in a spectro-electrochemical cell, we can also observe the differences in the electric field at the two positions on the

surface of the specifically oriented SAM-bound Cyt-c (Xu & Bowden 2006). As one position is in the protein binding patch, close to the SAM, and the other one on the far side of the protein from the SAM, this enables us to examine the existing electrostatic model describing electric fields at protein-coated SAMs (Murgida & Hildebrandt 2001).

1.3 Become the arrow – MBN-containing SAMs to elucidate SAM electrostatics

One of the great advantages spectro-electrochemical methods provide is the ability to spectroscopically probe electrode-attached species, such as SAMs, while applying an electric potential. This possibility, in combination with the VSE, turned out to be particularly useful for improving our understanding of SAM electrostatics. SAMs have been known to modify the electrostatics of noble metal electrodes (Love et al. 2005) by changing their energy level distribution (de Boer et al. 2005; Heimel et al. 2007) and by creating a dielectric barrier between the SAM-modified electrode and the electrolyte solution, thereby altering its double layer capacitance (Ramírez et al. 2007). The result is altered potential of zero charge (E_{pzc}) and potential profile at the metal/SAM/solution interface. These depend on the metal, the SAM, the electrolyte, the ionic strength and the applied potential. Electrostatic models (Smith & White 1992; Murgida & Hildebrandt 2001) have been developed in order to explain these potential profiles and to predict the magnitude of the electric field at the SAM/solution interface. However, quantifying these electric fields has been complicated by the size of the system and by the multitude of factors affecting it. Moreover, the direct measurement of the potential of zero charge of the SAM-modified metal has been complicated due to the formation of an interfacial potential at the SAM surface, where solvent molecules and counter ions orient according to the electrode charge (Smith & White 1992). By creating pure and mixed MBN-containing SAMs on both Ag and Au, and by probing them spectroscopically under solvent gradients and at different applied potentials, we disentangle several factors affecting the MBN nitrile stretching frequency, allowing us to estimate the effective potential of zero charge of the SAM-coated metal separately from the interfacial potential, and to report electric field magnitudes at the SAM surface. It is also interesting to note how in a specifically oriented SAM the complexity of the

spectroscopic manifestation of the Stark effect is greatly reduced, compared to that observed in isotropically oriented populations in frozen organic glasses (Andrews & Boxer 2000a; Suydam & Boxer 2003).

The following work therefore demonstrates how the vibrational Stark effect can be used, in combination with aqueous-phase or surface enhanced vibrational spectroscopy, electrostatic models and enzyme kinetics, to probe and elucidate surface electrostatics in SAMs and proteins, thus contributing to our understanding of their properties and function.

Theoretical Background

2.1 Self Assembled Monolayers (SAM)

A self assembled monolayer (SAM) is a one-molecule-thick layer composed of spontaneously-organized monomers, attached to a surface. SAMs have been gaining much attention over the last two decades, due to their versatile uses, allowing to modify metal surfaces in order to allow the adsorption of proteins, DNA or anti-bodies to the metal, while maintaining biological function (Samanta & Sarkar 2011; Murgida & Hildebrandt 2005; Sezer et al. 2012), but also to avoid protein adsorption to metal surfaces (Chapman et al. 2000), as components in etching and photolithography processes and in nano-electronics (Love et al. 2005). While many different kinds of monomers can be used (Love et al. 2005; Heimel et al. 2007; Samanta & Sarkar 2011), in this work we concentrate on SAMs comprising organo-thiol monomers deposited on either Au or Ag surfaces. The monomer is composed of a thiol head group, an organic tail and various possible terminal groups or functionalities. For schemes of the monomers used here, see fig. 2.1.1.

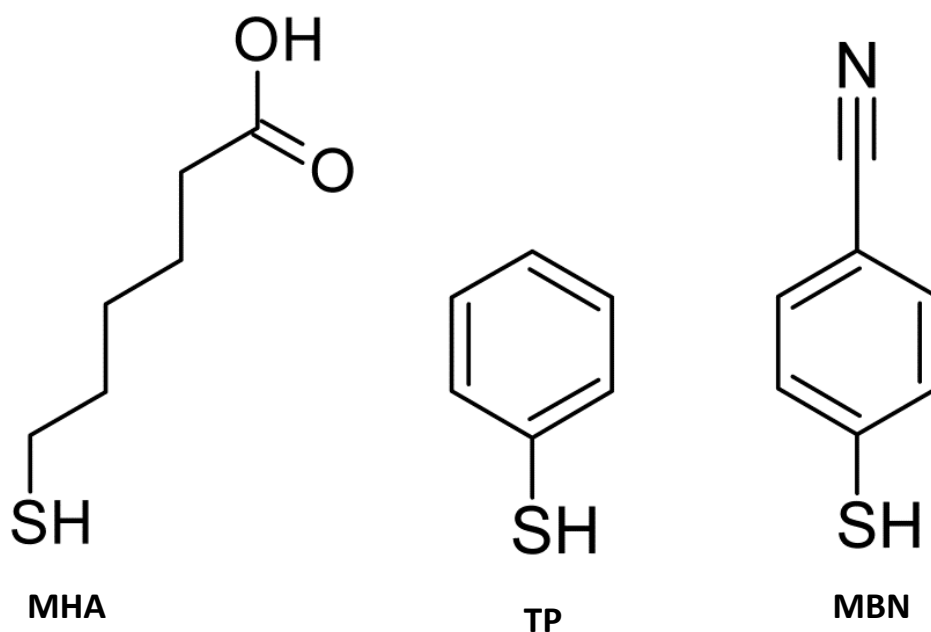


Figure 2.1.1. The three SAM monomers used in this work: mercaptohexanoic acid (MHA), thiophenol (TP) and 4-mercaptobenzonitrile (MBN)

The reaction for SAM-adsorption on the metal surface involves the reduction of the S-H bond as follows:



This process, however, may be followed by the following reversible reaction:



Allowing an exchange between monomers in the solution and the ones already attached to the metal (in form of a dimer). This exchange process allows the SAM, which is first deposited in a less than ideal order level, to reorder until the packing reaches its optimum. This process may take hours, and so normally the SAMs are left to form overnight. Depending on the metal and on the monomer, the exchange process may require the application of a potential to the metal, which can be controlled, allowing the potential-assisted formation of mixed SAMs (Meunier-Prest et al. 2010; F. Ma & Lennox 2000).

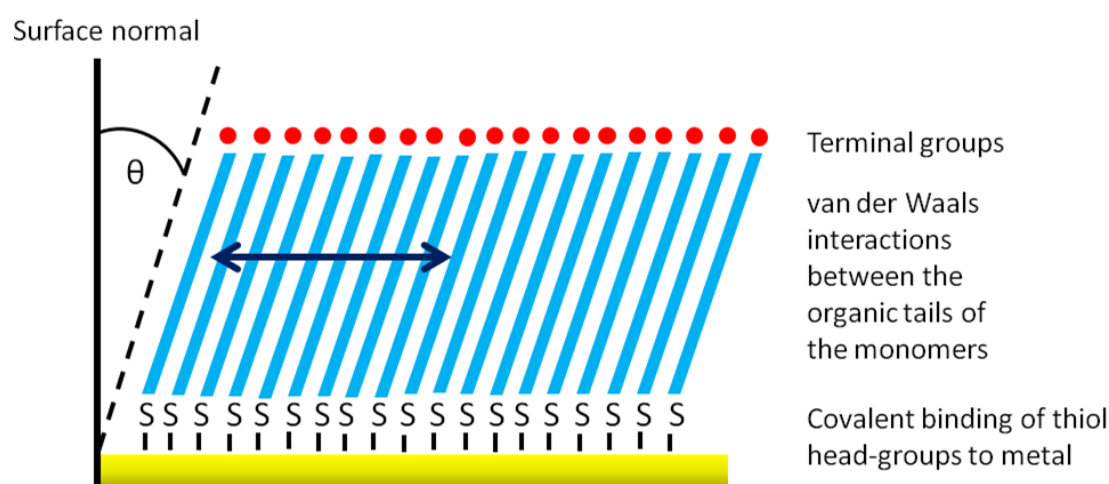


Figure 2.1.2. Schematic representation of an organo-thiol SAM on a gold surface

The high level of ordering inherent to SAMs arises predominantly from the affinity of the monomer to the surface. Organo-thiol monomers have shown high affinity to coinage metals (Laibnis et al. 1991) and Hg (Demoz & Harrison 1993), and in this work

we shall focus on SAMs adsorbed to Au and Ag surfaces. A scheme of an organo-thiol SAM on Au is shown in fig. 2.1.2, where the different parts of the SAM and the interactions involved are depicted.

To deposit a single-component SAM, the metal surface is brought in contact with a homogenous solution of the monomer in an organic solvent, and left to incubate for several hours (Wisitruangsakul et al. 2008). Me-S bonds are formed, binding the monomers to the surface, and van der Waals interactions between the organic tail groups bring the monomers together, till they are closely packed.

2.1.1 The tilt angle θ

From *ab initio* calculations it arises that the monomers are ordered in a herringbone structure, with two repeating lines of almost identical tilt angles (θ in fig. 2.1.2), leaning in opposite directions (Jiang et al. 2009; Heimel et al. 2007; Schalnath & Pemberton 2010). The tilt angle is determined by several factors, including the metal-S-C bond angle, hydrophobic interactions with an aqueous phase with which the SAM may be brought into contact, and a voltage that may be applied to the metal surface, attracting or repulsing charged or partially charged terminal groups, if such exist (see for example section 4.3).

The tilt angle is also different for different kinds of monomers and for different chain-lengths. Different tilt angles are also found for different substrates. The tilt angle is measured using various techniques. Surface spectroscopy, such as IR-RAS (Infrared reflection absorption spectroscopy), SEIRA (surface enhanced IR absorption) or SERS (surface enhanced Raman spectroscopy), are useful, thanks to the surface selection rule (see section 2.5.4.1) (Hallmann et al. 2008; Wan et al. 2000; Han et al. 2001). Near-edge X-ray absorption fine structure spectroscopy (NEXAFS) is another popular method, where the tilt angle can be deduced from the dependence of the π^* resonance intensities on the radiation angle of incidence. Other researchers use theoretical models (S. Franzen 2002), theoretical models in combination with scanning tunneling microscopy (STM) (Jiang et al. 2009) or surface plasmon spectroscopy (Ehler et al. 1997) to determine the tilt angle. Some results pertinent to our research are presented in table

2.1.1. As seen in the table, some variation between the different methods and monomers exists, however for all monomers and methods it is clear that the tilt angle is greater for SAMs on Au than on Ag. Also, for both Ag and Au, the tilt angle is greater for aromatic SAMs.

Table 2.1.1. Tilt angles of SAMs consisting of different monomers on Ag and Au substrates, and the methods used to measure them.

SAM monomer	Tilt angle (θ) on Ag substrate	Tilt angle (θ) on Au substrate	Measurement method	Reference
TP ^a		54	NEXAFS	(Käfer et al. 2007)
TP	24	49	NEXAFS	(Frey et al. 2001)
TP	27		SERS	(Han et al. 2001)
TP	29		UPS ^b	(Schalnat & Pemberton 2010)
4-fluorothiophenol		58	STM+DFT ^c	(Jiang et al. 2009)
HS(CH ₂) ₁₁ CH ₃ , HS(CH ₂) ₁₅ CH ₃	0 0	45 42	Surface Plasmon Spectroscopy	(Ehler et al. 1997)
HS(CH ₂) ₁₁ CH ₃		37	DFT	(S. Franzen 2002)
HS(CH ₂) ₁₅ CH ₃	11		IR-RAS	(Laibnis et al. 1991)
HS(CH ₂) ₁₁ CH ₃ , HS(CH ₂) ₁₅ CH ₃	11 12	30	IR-RAS	(Walczak et al. 1991)
HS(CH ₂) ₁₁ CH ₃ , HS(CH ₂) ₁₅ CH ₃		32 34	STM	(Pflaum et al. 2002)

^a Thiophenol

^b Ultraviolet photoelectron spectroscopy

^c Density function theory

2.1.2 Changes to the potential of zero charge (E_{pzc}) due to SAM coating

The potential of zero charge (E_{pzc}) of a metal surface is the potential at which the metal surface is not charged, which does not normally coincide with an arbitrarily determined 0 V potential against a certain reference electrode, nor necessarily with the potential of the metal at open circuit as measured in a specific electrochemical setup. E_{pzc} of the bare metal is determined by its work function, Φ , and depends on it as follows:

$$(2.1.3) \quad E_{pzc} = \Phi - K$$

where E_{pzc} is expressed in V vs. NHE and K is a constant that was determined to be 5.01 and 4.61 eV for Ag and Au, respectively (Emets & Damaskin 2009; Trasatti 1971). Recommended values for the work function of bare polycrystalline Ag and Au are 4.3 and 4.88 eV, respectively (Valette 1982; Trasatti 1984), yielding -0.71 V and +0.27 V vs. NHE for E_{pzc} of polycrystalline Ag and Au, respectively.

However, it has been shown by electrochemical measurements and UPS, that the work function, and therefore the E_{pzc} of a metal is changed when its surface is modified with a SAM (Ramírez et al. 2007; Heibel et al. 2007; L. Wang et al. 2009; Alloway et al. 2009). According to Heibel et al. (2007; 2008), the degree (and direction) to which the work function of the metal is changed, $\Delta\Phi$, is determined as follows:

$$(2.1.4) \quad \Delta\Phi = \Delta V_{vac} + BD$$

where BD is the metal-S bond dipole, and ΔV_{vac} is the potential difference across the dipolar SAM, as illustrated in fig. 2.1.3 for Au(111) (Heibel et al. 2007).

The bond dipole (BD) has its origin in two mechanisms: A) The so called “push-back” effect, where the metal surface dipole, created by electrons leaking out of the metal, is decremented due to the presence of other atoms (here sulfur) at the surface, and B) The change in charge density due to the transformation of the S-H bond into a Au-S bond. This change in charge density is limited to the metal-SAM interface, as it only reaches the first layer of atoms on each side of the interface, and does not propagate any further. Moreover, it is independent of the nature of the SAM itself, and is identical for different

monomers, so long as the head-group binding the monomer to the metal is sulfur (Heimel et al. 2008).

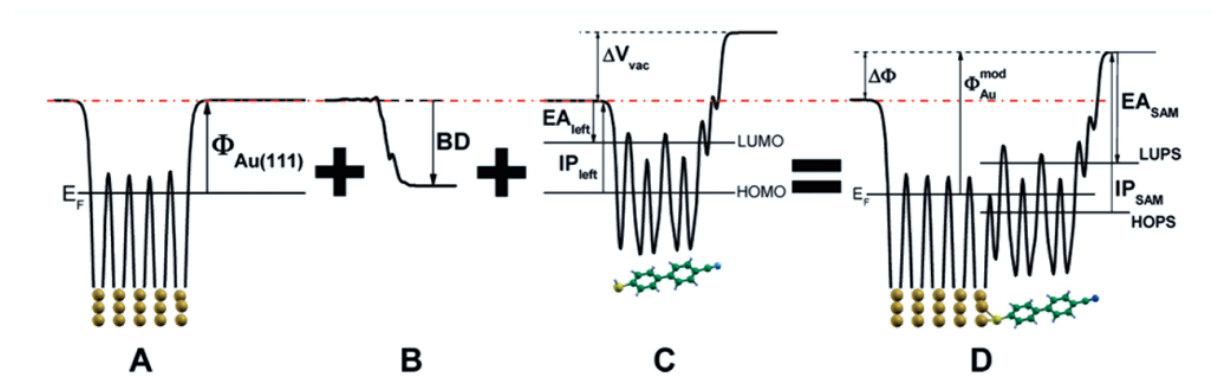


Figure 2.1.3. **A.** Bare Au(111), its Fermi level (E_F) and work function (Φ); **B.** The Au-S bond dipole; **C.** A dipolar *p*-cyanodiphenylthiol SAM, as modeled separately from any metal surface. IP_{left} and EA_{left} are the ionization potential and electron affinity corresponding to the HOMO and LUMO, respectively, of the SAM, on its side that would be eventually attached to the metal surface, and ΔV_{vac} is the potential difference across the SAM, resulting from its dipolar nature. **D.** The resulting change in the work function of the metal arising from its modification by the SAM, and the electron affinity and ionization potential of the combined system. From Heimel et al. 2007.

The other component of $\Delta\Phi$, ΔV_{vac} , is given by the Helmholtz equation:

$$(2.1.5) \quad \Delta V_{\text{vac}} = -\frac{\mu_{\perp}}{\epsilon_0 A}$$

where μ_{\perp} is the dipole moment component of the SAM parallel to the surface normal and A is the area of the unit cell (Heimel et al. 2007).

The SAM dipole moment, μ , is not equal to that of a single monomer, as each monomer in the SAM is depolarized by neighboring monomers, according to:

$$(2.1.6) \quad p = \frac{p_0}{1 + \frac{ak}{l^3}}$$

where p is the molecular dipole of a monomer in the SAM, p_0 is the molecular dipole of the monomer in the gas phase, a is the polarizability of the monomer, l is the distance between the monomers along one direction of periodicity, and k is an empirical constant depending only on the shape of the unit cell. For a square unit cell, k is estimated to be 9.034 (Natan et al. 2007). Although this is a classical model, completely neglecting any quantum effect, the results it supplies compare strikingly well with those obtained by DFT calculations (Natan et al. 2007; Natan et al. 2006).

Once μ for the SAM has been determined, either by equation 2.1.6 or with the aid of explicit DFT calculations (Natan et al. 2007), μ_{\perp} is the projection of μ on the surface normal, according to:

$$(2.1.7) \quad \mu_{\perp} = \mu \cos(\beta)$$

where β is the tilt angle of the molecular dipole of the monomer with respect to the surface normal (unlike θ , which is the tilt angle of the non-sulfur part of the monomer only).

It should be noted, however, that Wang et al. (2009) has shown that, most remarkably, for different SAMs, regardless whether aliphatic or aromatic, so long as the anchoring head-group (thiol in our case) and terminal group (nitrile) are maintained, the only parameter $\Delta\Phi$ depends on is $\cos(\beta)$, which is, evidently, different for the different monomers.

Once $\Delta\Phi$ is determined, the effective potential of zero charge of the SAM-coated metal is calculated by simply adding $\Delta\Phi$ to the right-hand side of equation 2.1.3.

2.1.3 Electrostatic model of the electric field at the SAM/solution interface

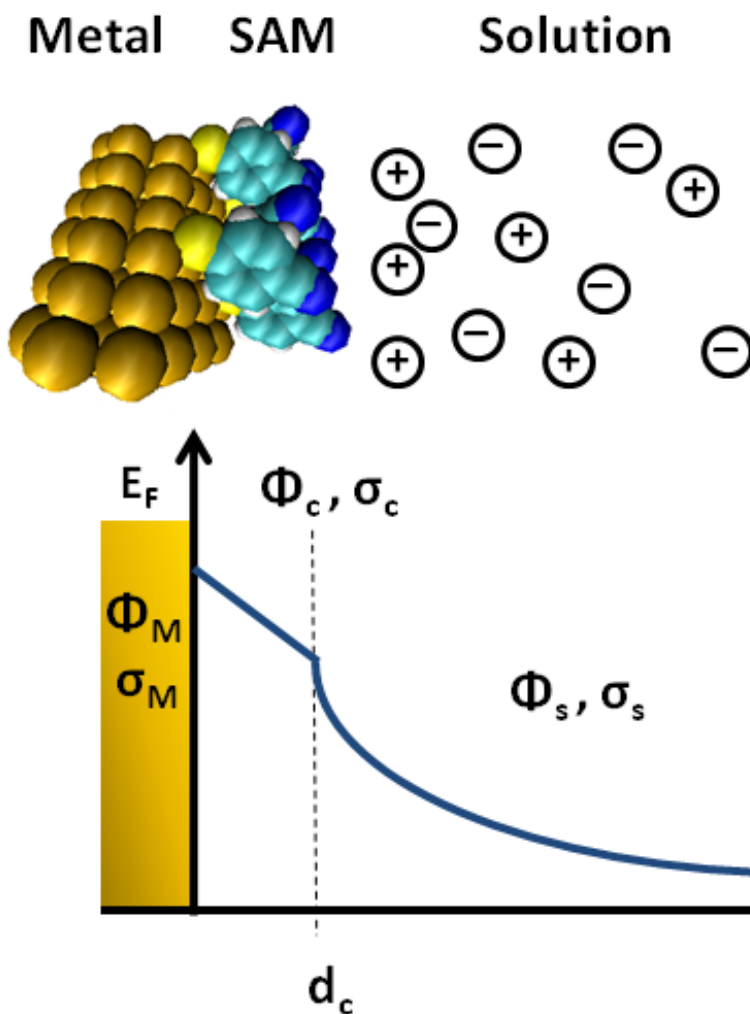


Figure 2.1.4. Schematic representation of the metal/SAM/solution interface, and the corresponding electric potential profile, according to the Gouy-Chapman model. x is the distance from the surface of the metal to the solution, d_c the monolayer thickness, Φ_i and σ_i are the potential (V) and charge density (Cm^{-2}) at a certain position, respectively, and M, c and s denote the metal surface, the SAM surface and the bulk solution, respectively.

In this section an electrostatic model will be discussed, which describes the potential distribution at the metal/SAM/solution interface, allowing to express the electric field

at the interface in terms of the intrinsic properties of the system and the potential applied to the electrode. This model is based on the one developed by Smith and White (1992). We assume that the charges are delocalized on the metal surface, and further that it is planar. Since the size of the nano-features of the electrode is tens to hundreds of nanometers (see section 2.5.4), while the SAM thickness, d_c , is on the scale of 1 nm, this is a reasonable assumption at a first approximation. ϵ_c and ϵ_s denote the dielectric constants of the SAM and the solution, respectively. The SAM in this model includes no charges of its own and is free from defects, which means the electrolyte cannot approach the metal surface closer than d_c . Therefore, the potential drops linearly along its profile. Furthermore, we neglect the contribution of molecular dipoles to the interfacial potential distribution. In the solution, the potential distribution is described by the Gouy-Chapman model as follows:

$$(2.1.8) \quad \tanh\left(ze\frac{\Phi_x - \Phi_s}{2kT}\right) = \tanh\left(ze\frac{\Phi_c - \Phi_s}{2kT}\right) e^{-\kappa(x-d_c)}$$

where Φ_x , Φ_s and Φ_c are the potential at a certain distance x from the SAM surface, in the bulk solution and at the SAM surface (see fig. 2.1.4), respectively, and κ is the reciprocal Debye length, defined as:

$$(2.1.9) \quad \kappa = \sqrt{\frac{2N_a e^2 I}{\epsilon_s \epsilon_c k_B T}}$$

where I is the ionic strength.

Considering the above described potential distribution, the electric field magnitude at each position in the model, according to $|E_F| = -\frac{dE}{dx}$ is:

$$(2.1.10) \quad \begin{aligned} |E_F| &= 0 && \text{for } x < 0 \\ |E_F| &= \frac{\Phi_M - \Phi_c}{d_c} && \text{for } 0 < x < d_c \\ |E_F| &= \kappa \left(\frac{2kT}{ze}\right) \sinh\left(\frac{\Phi_x - \Phi_s}{2kT}\right) && \text{for } x > d_c \end{aligned}$$

To express the electric field in terms of charge densities, one may use Gauss's Law:

$$(2.1.11) \quad \oint |E_F| \cdot dA = \frac{q}{\epsilon_0}$$

according to which, the electric flux through a closed surface enclosing a volume is the surface integral of the electric field projected perpendicular to the surface, and is also proportional to the charge enclosed in the volume. A convenient case of the law is the case of a box, with a planar, rectangular surface. To facilitate the discussion we build boxes that have faces parallel to the electrode surface (see fig. 2.1.5), so that the electric field has a non-zero scalar product only with the area vector elements of these faces.

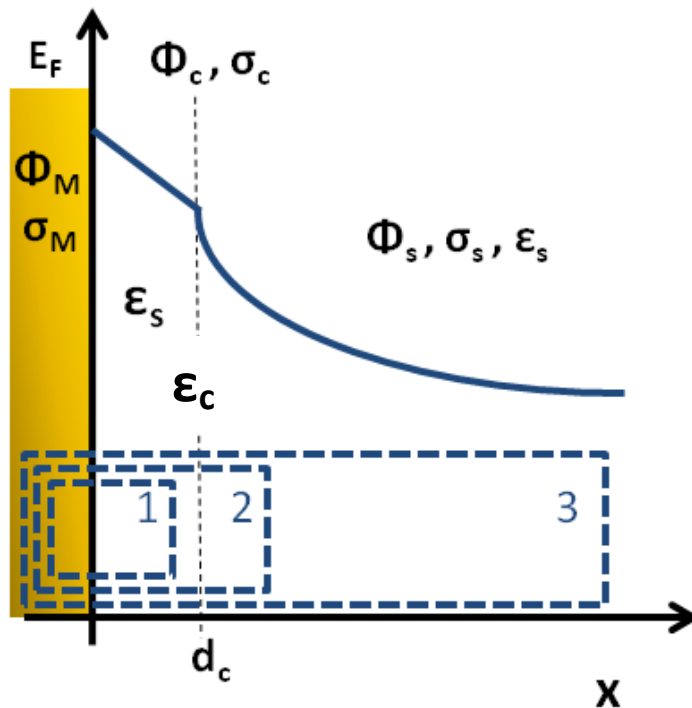


Figure 2.1.5. To employ Gauss's law for our model, enclosed volumes (boxes) 1, 2 and 3 are added to the model scheme.

With the aid of boxes 1, 2 and 3, as depicted in fig. 2.1.5, we relate charge densities and interfacial potentials as follows:

$$(2.1.12) \quad \text{Box 1:} \quad \sigma_M = \frac{\epsilon_0 \epsilon_c}{d_c} (\Phi_M - \Phi_c)$$

$$(2.1.13) \quad \text{Box 2:} \quad \sigma_s = -\epsilon_0 \epsilon_s \kappa \frac{2kT}{ze} \sinh \left(ze \frac{\Phi_c - \Phi_s}{2kT} \right)$$

$$(2.1.14) \quad \text{Box 3:} \quad \sigma_M + \sigma_c + \sigma_s = 0$$

To simplify equation 2.1.13, we take the case that $\Phi_c - \Phi_s$ is very small, which is the case for the region adjacent to the SAM surface, also known as the inner Helmholtz plane. In this case:

$$(2.1.15) \quad \sigma_s = -\varepsilon_0 \varepsilon_s \kappa (\Phi_c - \Phi_s)$$

Now, since $\Phi_M = E - \Phi_{ref}$ and $\Phi_s = E_{pzc} - \Phi_{ref}$, the combination of eqns. 2.1.12, 2.1.14 and 2.1.15 yields:

$$(2.1.16) \quad \sigma_M = \frac{\varepsilon_0 \varepsilon_c}{d_c} (E + \Phi_{ref} - \Phi_c)$$

$$(2.1.17) \quad \sigma_s = -\varepsilon_0 \varepsilon_s \kappa (\Phi_c - E_{pzc} - \Phi_{ref})$$

Summation of the above equations yields, after rearrangement:

$$(2.1.18) \quad \sigma_s = \sigma_M \frac{d_c \kappa \varepsilon_s}{\varepsilon_c} - \varepsilon_0 \varepsilon_s \kappa (E - E_{pzc})$$

Substituting with σ_s from eq. 2.1.14 and expressing σ_M as $\varepsilon_0 \varepsilon_c |E_F|$, one obtains:

$$(2.1.19) \quad |E_F| (\varepsilon_0 \varepsilon_c + \varepsilon_0 \varepsilon_s \kappa d_c) + \sigma_c - \varepsilon_0 \varepsilon_s \kappa (E - E_{pzc}) = 0$$

Or after rearrangement:

$$(2.1.20) \quad |E_F| = \frac{\varepsilon_s \kappa \varepsilon_0}{\varepsilon_0 (\varepsilon_c + \varepsilon_s \kappa d_c)} (E - E_{pzc}) - \frac{\sigma_c}{\varepsilon_0 (\varepsilon_c + \varepsilon_s \kappa d_c)}$$

The latter describes the electric field at an immediate proximity to the SAM surface only. To describe the electric field further into the solution one may apply an exponential decay model, which serves as a first approximation, as follows:

$$(2.1.21) \quad |E_F|_x = \kappa |E_F|_{d_c} e^{-\kappa x}$$

(Lorenz 2004)

2.2 Heme proteins

Heme proteins are proteins containing a heme prosthetic group, composed of an iron-porphyrin complex. There is a great variety of such proteins in nature, including electron shuttles, enzymes, oxygen carriers and more. The function of the protein is determined by the structure of the heme group and of the protein itself, as well as the interactions between them under different conditions. Heme proteins are widespread among all organisms, since they take part in both photosynthetic and respiratory processes. Due to the diversity in structure and function, as well as their high biological importance, heme-proteins have gained much attention over past decades.

A heme is composed of a porphyrin - a cyclic methine-bridged tetrapyrrole - and a central iron atom coordinated to the four pyrrole nitrogens (Siebert & Hildebrandt 2007). The porphyrin is highly conjugated, which allows for electron delocalization across its π -orbitals. Three types of heme exist, *a*, *b* and *c* (see Fig. 2.2.1). In heme *c*, the heme is attached to the protein covalently through thioether bonds with two cysteines, which are part of a conserved CXXCH sequence in the hydrophobic heme pocket (Paoli et al. 2002). The redox activity of the heme is based on the oxidation of Fe^{2+} (reduced, or ferrous) to Fe^{3+} (oxidized, or ferric) of the heme-iron and vice versus. The heme is located in a hydrophobic pocket in the protein (the heme pocket), and the iron atom is coordinated, apart from the four pyrrole nitrogens of the porphyrin, to the ϵ nitrogen in the imidazole functionality of a so called proximal histidine residue. In this way, a small molecule, such as oxygen, CO, water or hydrogen peroxide can bind to the iron in its sixth coordination position, stabilized by a distal residue (a residue on the other side of the heme), such as histidine or arginine. The heme pocket is divided to a proximal and a distal pocket, accordingly (Lecomte et al. 2005).

2.2.1 Cytochrome *c*

Cytochromes are heme-proteins, which are mostly involved in energy-transfer processes, such as metabolism, catalysis and photosynthesis. The particular function they fulfill is dictated by the specific protein structure and by the interactions between

the protein and the heme group, as well as the type of heme. Cytochromes may contain a *b* or *c* type heme (Lecomte et al. 2005).

Cytochrome *c* (Cyt-*c*) is a small cytochrome, containing one heme *c*, which acts as an electron shuttle in the mitochondrial respiratory chain. It is found near the mitochondrial inner membrane in Eukaryotes, and it transfers one electron from Cytochrome *bc1* to Cytochrome *c* oxidase. After four such cycles, oxygen can be reduced to water. In both its reduced (Fe^{2+}) and oxidized (Fe^{3+}) states, the iron is bound to its six ligands (the porphyrin nitrogens, Met80 and His18, see Fig. 2.2.2) (Siebert & Hildebrandt 2007). On the surface of Cyt-*c*, in the vicinity of its heme-pocket, there is a relatively high concentration of lysine residues, some of which participate in the binding of Cyt-*c* to Cytochrome *c* oxidase or to a SAM. These residues appear in blue in Fig. 2.2.2. Figure 2.2.3, taken from Xu and Bowden (2006), shows the orientation of Cyt-*c* while attached to a mercaptoundecanoic acid SAM, similar to the mercaptohexadecanoic SAM used in experiments presented here.

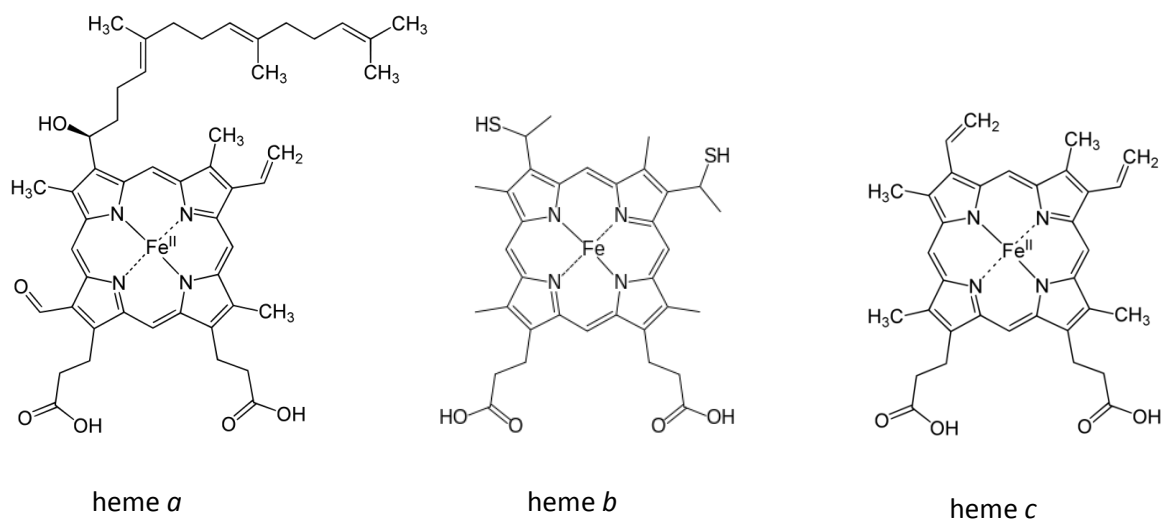


Figure 2.2.1. Types of heme

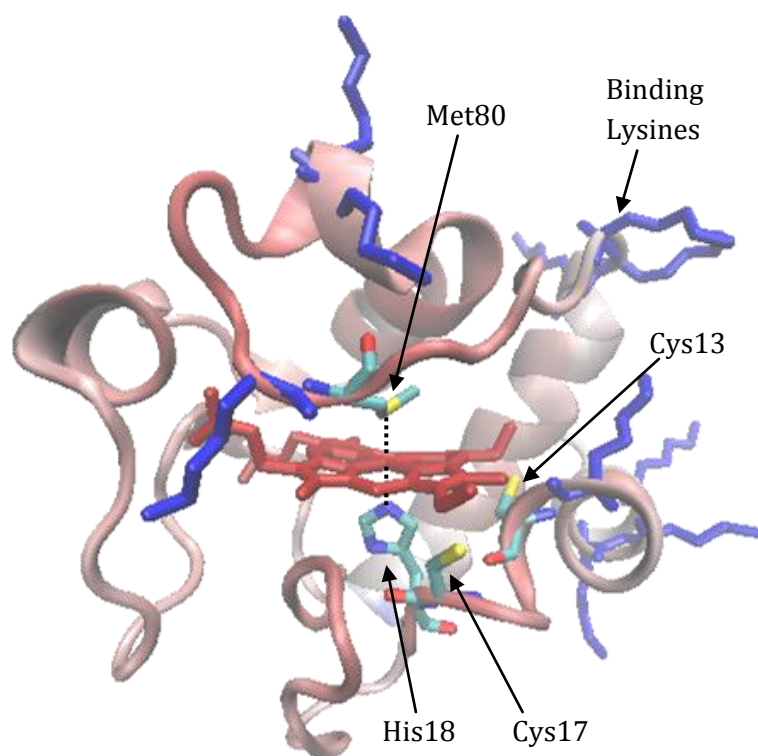


Figure 2.2.2. Horse heart Cyt-*c* [crystal structure 1HRC, (Bushnell et al. 1990)]. In red: the heme group, in blue: lysine residues 13, 86-88, 72, 73, 5, 7 and 8, which participate in Cyt-*c* binding (J. Xu & Bowden 2006). Highlighted are also His18 in the proximal position, Met80 in the distal position, and Cys 13 and 17 that covalently bind the heme to the protein.

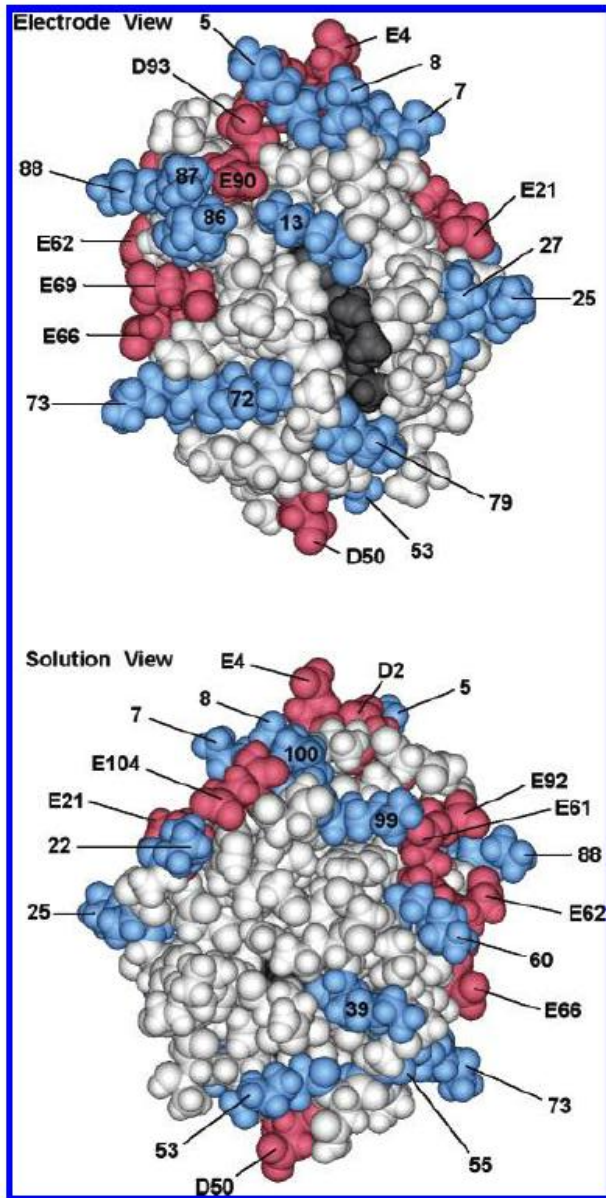


Figure 2.2.3. From Xu and Bowden (2006): Horse heart Cyt-c as oriented while attached to a mercaptoundecanoic acid SAM, in 4.4 mM potassium phosphate buffer, ionic strength 10 mM. **Top:** view from the SAM surface, with the heme group in black. **Bottom:** view from the solution. Blue: positively charged lysine residues. Red: negatively charged aspartate (D) and glutamate (E) residues. Lysines 13, 86-88, 72, 73, 79, 5, 7 and 8 have been shown to be involved in SAM binding of the protein. This was performed by Schiff-base methylation of lysines in the bound protein and subsequent digestion and LC-MS analysis of the protein fragments. Since only Lysines that were not involved in binding could be methylated, assignment of binding lysines was achieved. It is interesting to note that residue 8 takes part in the binding, while residue 39 is almost directly on the opposite side of the protein from the SAM surface (see section 4.2).

2.2.2 Dehaloperoxidase-hemoglobin A

Dehaloperoxidase-hemoglobin A (DHP A) is a double function protein found in the benthic organism *Amphitrite ornate* (Lebioda et al. 1999). It is a globin, characterized by the globin fold, which consists of 8 α -helices that form a globular structure around a heme prosthetic group. The heme is located in a hydrophobic pocket, due to the globular structure of this water soluble protein, where hydrophilic residues are concentrated on the surface of the protein. DHP A is predominantly a monomer in solution (Thompson et al. 2011). The protein has a double function in its native organism: on one hand it serves for oxygen storage and transport, and on the other, in its peroxidase function, for the oxidation of marine toxin 2,4,6-tribromophenol (TBP) to 2,6-dibromoquinone (DBQ), a less toxic compound. It can also similarly oxidize all the other 2,4,6-trihalophenols with varying efficiencies (Thompson 2011). Figure 2.2.4 shows the reaction it catalyzes. As seen in the figure, at physiological pH the substrate is negatively charged (pKa=6.0). It has been found that the isoelectric point of the entire protein is pH=6.8, indicating that at physiological pH it has an overall negative charge (Zhao et al. 2012). This may explain the observation that the kinetics of the enzyme at low substrate concentrations are diffusion controlled (Ma et al. 2010), since the mutual repulsion of the negatively charged enzyme and substrate is likely to cause substrate binding to become the rate limiting step.

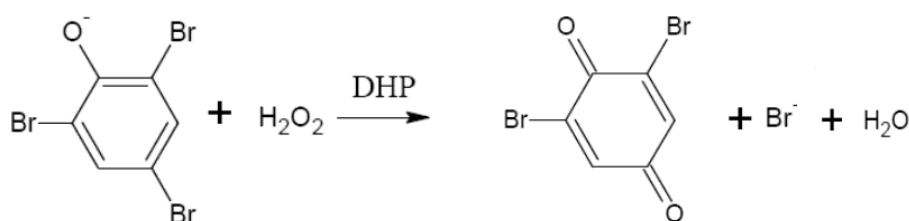


Figure 2.2.4. The reaction catalysed by DHP in its role as peroxidase.

As with many peroxidases, such as horseradish peroxidase and cytochrome *c* peroxidase, here too the distal stabilizing residue, His55 in DHP A, plays an active role in stabilizing intermediates leading to the creation of active compound I, as seen in Fig. 2.2.5. His55 in DHP A can assume a closed or open conformation, where only in the closed conformation dehaloperoxidase activity of the enzyme is allowed (Thompson, Davis, et al. 2010). When the substrate is present in the solution, His55 is pushed to the closed position, allowing dehaloperoxidase activity, unless an inhibitor, such as 4-bromophenol, is also present. This inhibitor is also present in the bentic environment, and it acts as an allosteric inhibitor, by entering the distal pocket and pushing His55 to the open conformation, where it cannot stabilize the heme-hydrogen peroxide intermediate necessary for catalysis (Thompson, Davis, et al. 2010). In DHP A, compound I and compound ES both consist of a Fe(IV)=O species (see Fig. 2.2.5) with a cation radical. However, in compound I the radical is located in the heme ring, while in compound ES it is found of Tyr34 (H. Ma et al. 2010; Thompson, S. Franzen, et al. 2010).

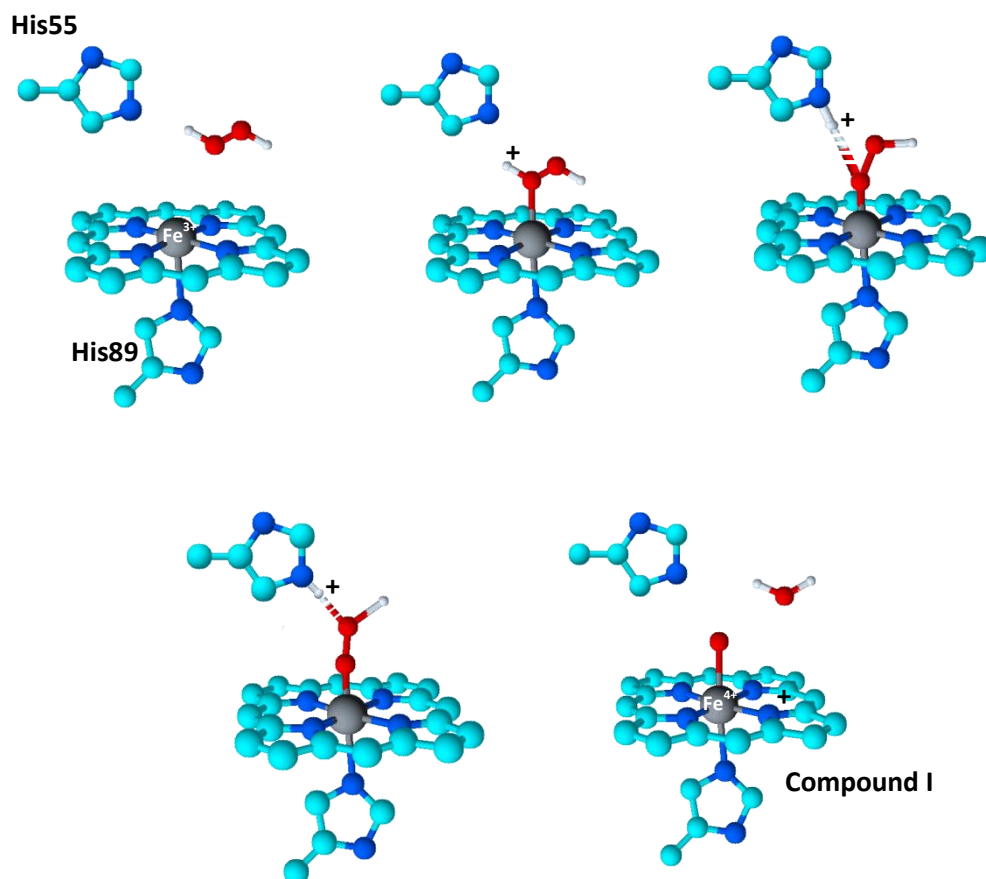
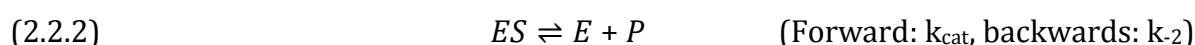
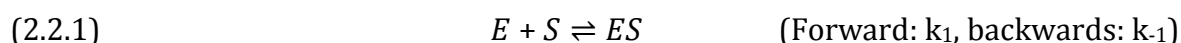


Figure 2.2.5. Intermediates on the way to active compound I in DHP A in its role as peroxidase.

2.2.3 Enzyme kinetics

Enzyme kinetics are commonly described by the Michaelis-Menten theory, which assumes that the enzyme (E) and substrate (S) must first meet to form the complex ES, and only then can the substrate be transformed into the product (P), as follows, for a simple two-step catalysis:



According to the Michaelis-Menten theory, if $[S] \gg [E]$, the initial reaction velocity is equal to the rate of ES breakdown, or:

$$(2.2.3) \quad V_0 = k_{cat}[ES]$$

where k_{cat} describes the number of substrate molecule turned over by the enzyme per second ($[s^{-1}]$), under ideal conditions. Both k_{cat} and $[ES]$ are not quantifiable, so that another expression must be developed as follows, starting from the rate equation for the formation of ES according to Eq. (2.2.1):

$$(2.2.4) \quad \frac{d[ES]}{dt} = k_1([E_T] - [ES])[S]$$

When $[E_T]$, the total enzyme concentration, is the sum of free and substrate-bound enzyme. Eq. (2.2.4) neglects ES concentration arising from the reverse reaction in Eq. (2.2.2), since for the calculation of the initial velocity, before any product was produced, $[P]$ can be assumed to be close to zero.

The rate equation for the decay of ES is then:

$$(2.2.5) \quad -\frac{d[ES]}{dt} = k_{-1}[ES] + k_{cat}[ES]$$

When assuming steady state, one obtains:

$$(2.2.6) \quad k_1([E_T] - [ES])[S] = k_{-1}[ES] + k_{cat}[ES]$$

and upon rearrangement:

$$(2.2.7) \quad \frac{([E_T] - [ES])[S]}{[ES]} = \frac{k_{-1} + k_{cat}}{k_1} = K_M$$

K_M is called the Michaelis-Menten constant, and the steady state concentration of [ES] is then:

$$(2.2.8) \quad [ES] = \frac{[E_T][S]}{K_M + [S]}$$

Combining (2.2.8) with (2.2.3), one obtains:

$$(2.2.9) \quad V_0 = k_{cat} \frac{[E_T][S]}{K_M + [S]}$$

and the maximum initial velocity, i.e. when $[S] \gg [E]$ and the enzyme is saturated is:

$$(2.2.10) \quad V_{max} = k_{cat}[E_T]$$

Substituting (2.2.10) into (2.2.9), one obtains the Michaelis-Menten equation:

$$(2.2.11) \quad V_0 = \frac{V_{max}[S]}{K_M + [S]}$$

From this equation one can also conclude that a reaction rate which is half the maximal rate is obtained when $[S]=K_M$, which is the concentration necessary for an efficient catalysis to occur (Lehninger 1970).

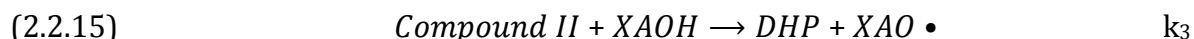
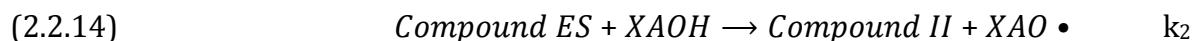
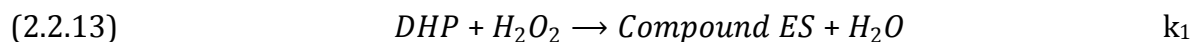
k_{cat}/K_M is called the catalytic efficiency, and it is large if either or both the rate of product formation from ES is high, or enzyme-substrate affinity is high (i.e. K_M is small). In dilute solutions, where $[S] \ll K_M$, eq. 2.2.9 can be transformed to:

$$(2.2.12) \quad V_0 = \frac{k_{cat}}{K_M} [E][S]$$

Since k_{cat}/K_M is a second-order rate constant, it can reach a maximum value, determined by the frequency of enzyme - substrate collisions. If a reaction reaches such a maximal rate, it is said to be diffusion-controlled, as every encounter between enzyme and substrate leads to the formation of a product molecule, and the only limitation on the catalytic efficiency is the rate at which substrate and enzyme can meet (Mathews et al. 2012).

2.2.3.1 DHP A kinetics

The kinetics of DHP A are somewhat more complicated than the above described general two-step case, as in this case three steps are involved, as follows:



Where XAOH is TBP or its other halogen homologues and XAO• is its radical, formed as an intermediate in the two electron transfer mechanism (Thompson, S. Franzen, et al. 2010; H. Ma et al. 2010).

Here compound ES is the Fe(IV)=O adduct, and the Michaelis-Menten equation is:

$$(2.2.16) \quad V_0 = \frac{V_{max}[XAOH]}{K_m + [XAOH]}$$

and since from step 1 it arises that:

$$(2.2.17) \quad V_{max} = k_1[H_2O_2][DHP_T]$$

The following equations may be derived:

$$(2.2.18) \quad k_{cat} = k_1[H_2O_2]$$

$$(2.2.19) \quad K_m = \left(\frac{1}{k_2} + \frac{1}{k_3}\right) k_1[H_2O_2]$$

$$(2.2.20) \quad \frac{k_{cat}}{K_m} = \frac{k_2 k_3}{k_2 + k_3}$$

As seen in the above expressions, V_{max} is independent of substrate binding rate constants, while K_m is dependent not only on the substrate binding rate constants, but also on $k_1[H_2O_2]$. Therefore, $\frac{k_{cat}}{K_m}$, or the catalytic efficiency, is the kinetic constant that is used for determining the efficiency of substrate binding to DHP A (Zhao et al. 2012).

2.3 UV/Visible spectroscopy

The transition of an electron from an occupied orbital to an unoccupied one (i.e. electronic transition) in a molecule is allowed when the transition dipole moment is non-zero. The transition dipole moment has the form:

$$(2.3.1) \quad R_k^{nm} = \int \Psi_n^* \mu_k \Psi_m dk$$

where k is the spatial coordinate, meaning that the dipole moment is anti-symmetric and therefore the selection rule for transition is that the product $\Psi_n^* \Psi_m$ is also anti-symmetric, or that the parity of the two orbitals is opposite.

The transition probability is then:

$$(2.3.2) \quad B_{nm} = \frac{8\pi^3}{3h^2(4\pi\epsilon_0)} |R^{nm}|^2$$

For each wavenumber, a molar absorptivity $\epsilon(\tilde{\nu})$ is defined as follows:

$$(2.3.3) \quad \int_{\tilde{\nu}_1}^{\tilde{\nu}_2} \epsilon(\tilde{\nu}) d\tilde{\nu} = \frac{N_A h \tilde{\nu}_{nm} B_{nm}}{\ln 10}$$

where N_A is the Avogadro number and h is the Planck constant.

When light in a frequency coinciding with one of the allowed transitions of the molecules is incident on a cuvette containing a sample (e.g. in a UV/Vis spectrometer), the light is absorbed by the sample according to the Beer-Lambert law:

$$(2.3.4) \quad A = \log_{10} \left(\frac{I_0}{I} \right) = \epsilon(\tilde{\nu}) cl$$

where I_0 is the intensity of the incident light, I that of the transmitted light, c is the concentration of the sample and l is the path length of the light in the sample (the dimension of the cuvette).

In heme proteins such as Cyt-c and DHP A, not only the concentration, but also the oxidation state of the protein can be determined from the UV/Vis spectrum. The wavelength of a strong transition from the ground to the second excited electronic state of the heme, also known as the Soret band, has typical values for each protein and oxidation state. For example, for DHP A, the Soret band is at 408 nm for the oxidized

(ferric) state, and at 418 nm for the reduced (ferrous) state. When the oxidized state has been poisoned with cyanide, the Soret band is red shifted to 423 nm. The concentration is determined using Eq. 2.3.4, by measuring A at a certain wavelength when l is given for the cuvette used and $\varepsilon_{(\nu)}$ is known for the relevant wavelength.

2.4 Cyclic voltammetry

In cyclic voltammetry (CV), a triangle-wave potential is applied to a three-electrode cell, in our case to the SEIRA cell depicted in Fig. 3.2.1, and the current is measured. The rate at which the applied potential is changed is called scan rate (v). For a diffusionless system, where the analyzed redox species is attached to the electrode, scanning from negative to positive, as we did in all our CV measurements, the following occurs: As the voltage at the working electrode (WE) becomes more positive, reduced species at the WE become oxidized, and a current is detected. When they become depleted, the current decreases to its previous level, and the process results in the so called anodic peak. Scanning back, from positive to negative, the opposite occurs (cathodic peak), and a symmetric cyclic voltammogram should result, with a minimal peak separation governed by the rate of electron transfer from the electrode-bound species to the WE. The average between the positions of the anodic and cathodic peaks (E_a and E_c , respectively) is E^o' , the formal potential of the system under its specific conditions.

Since the amount of analyte adsorbed to the electrode is small, a significant feature of a CV in a diffusionless system is the capacitive current, arising from charging and discharging the electrode and the subsequent formation of the counter-ion double layer at the electrode surface (a non-Faradaic process). If the opposite charges that are ordered at an electrode interface (electrons or holes at the metal electrode and counter-ions at the inner Helmholtz layer in the interfacial electrolyte) are modeled as an equivalent capacitor, its capacity is:

$$(2.4.1) \quad C = \frac{\varepsilon\varepsilon_0A}{d}$$

where ε_0 is the permittivity of vacuum, ε the dielectric coefficient of the substance separating the counter-ion double layer from the metal surface, A the area of the equivalent capacitor, and d the distance between the counter-ion double layer and the

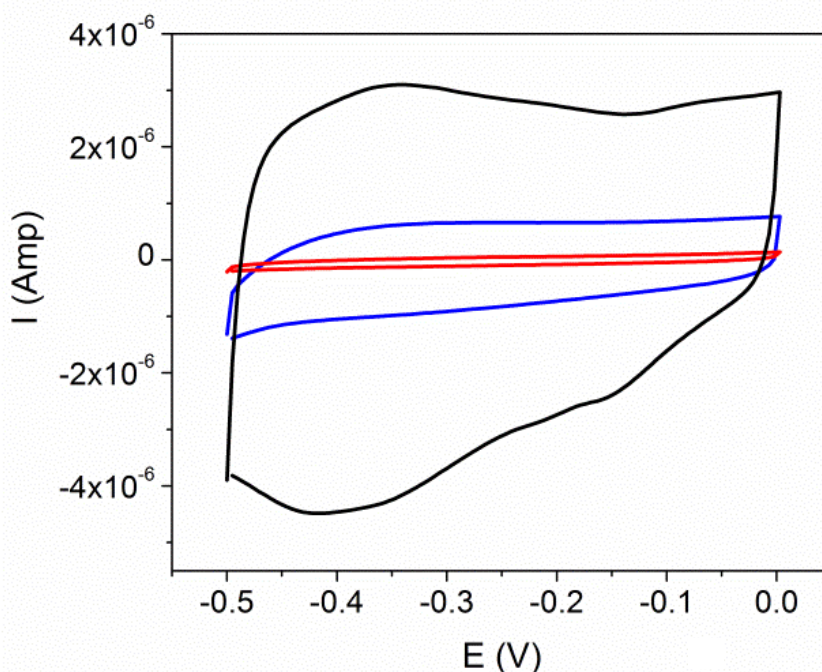
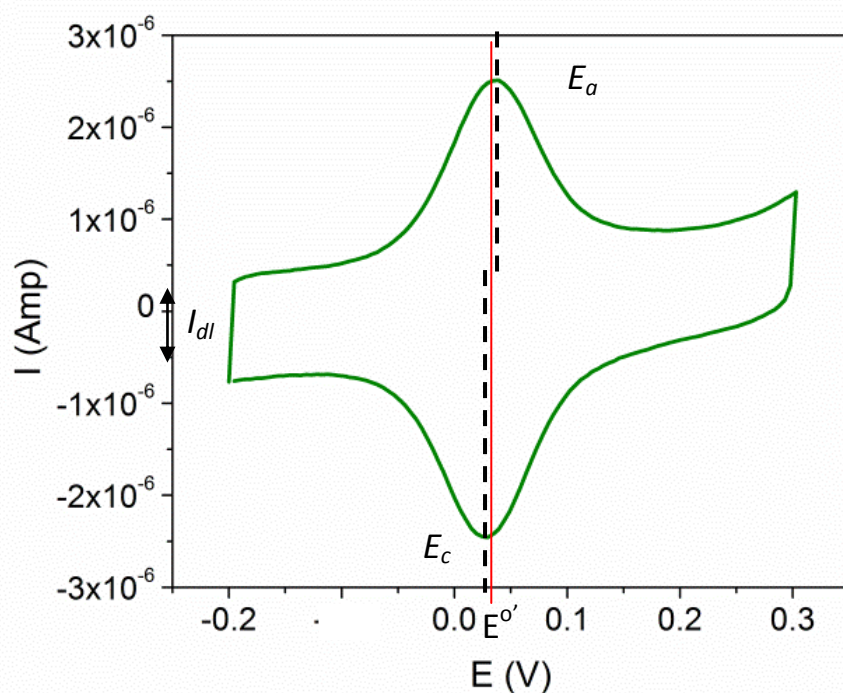


Figure 2.4.1. Cyclic voltammograms. Scan rate 50 mV/sec, voltage measured against Ag/AgCl. **Top:** Au film electrode coated with MHA, with Cytochrome *c* immobilized. The peaks are nearly symmetric, typically of a diffusionless system. Peak separation arises from the electron transfer rate only and the capacitive current is clearly seen. **Bottom:** Bare Ag disc electrode (black) and the same electrode coated with MHA SAM (blue) and with mercaptoundecanoic acid SAM (red). The decrease in the capacitive current with SAM length can be clearly seen.

metal surface. From the above equation it is then clear that the capacitance, and therefore the capacitive current of the system is greatly decreased when the electrode is coated with a SAM, as the SAM works to both increase d and reduce ϵ (in comparison to the aqueous medium). The capacitive current depends on the double layer capacitance as follows:

$$(2.4.2) \quad I_{dl} = 2AvC_{dl}v$$

where I_{dl} is the capacitive current (Amp), v the scan rate (V/s), A the area of the WE (cm^2) and C_{dl} the area-specific capacitance of the double layer at the SAM (F/cm^2) (Leopold 2000). In figure 2.4.1 different CVs are shown, demonstrating the above discussed phenomena and quantities.

2.5 Vibrational spectroscopy

2.5.1 The harmonic oscillator – classical model

The potential energy of a harmonic oscillator can be defined as follows:

$$(2.5.1) \quad V_{(x)} = \frac{1}{2}kx^2$$

where x is the displacement from the point of equilibrium, and k is the spring constant. When the harmonic oscillator is a molecule, the spring constant is the force constant of the chemical bond. The x coordinate is transformed to a mass dependent coordinate:

$$(2.5.2) \quad q = m^{1/2}x$$

and so the potential energy is expressed as:

$$(2.5.3) \quad V_{(q)} = \frac{1}{2}\omega^2q^2 = V_0 + \left(\frac{dV}{dq}\right)_0(q - q_0) + \frac{1}{2}\left(\frac{d^2V}{dq^2}\right)_0(q - q_0)^2 + \dots$$

as expanded in a Taylor series around the point of equilibrium, where $\omega^2 = \frac{k}{m}$ and the first derivative term is therefore zero. Hence:

$$(2.5.4) \quad V_{(q)} \cong \frac{1}{2} \left(\frac{d^2V}{dq^2} \right)_0 (q - q_0)^2$$

and:

$$(2.5.5) \quad \omega^2 = \frac{1}{2} \left(\frac{d^2V}{dq^2} \right)_0$$

2.5.2 The harmonic oscillator – quantum model

When discussing harmonic oscillations, i.e. vibrational motion, in a chemical bond, the energy is quantized, and can be described as:

$$(2.5.6) \quad E_n = \hbar\omega\left(\nu + \frac{1}{2}\right) \quad \text{with} \quad \omega = \sqrt{\frac{k}{m}} \quad \text{and} \quad \nu = 0, 1, 2, \dots$$

As a consequence, the energy of the oscillator is never zero, even at the lowest vibrational state. Transitions between the vibrational levels are dictated by the following integral describing the electrical dipole moment, expanded as a Taylor series to the first order (as q is small near the point of equilibrium, the higher terms are negligible):

$$(2.5.7) \quad \int_{-\infty}^{\infty} \psi_{i(q)} \mu_{(q)} \psi_{j(q)} dq = \mu_0 \int_{-\infty}^{\infty} \psi_{i(q)} \psi_{j(q)} dq + \int_{-\infty}^{\infty} \psi_{i(q)} \left(\frac{d\mu}{dq} \right)_0 q \psi_{j(q)} dq$$

where ψ is the wave function, i and j are two vibrational states, and μ is the dipole moment. Since the wave functions are alternately symmetrical and anti-symmetrical, it arises that the transition selection rules is $\Delta\nu = \pm 1$. This is true for a harmonic oscillator, but when anharmonicity is involved, overtones, i.e. transitions of $\Delta\nu > \pm 1$ may result. Since the first term in the Taylor expansion is zero due to the orthogonality of the wave function of different states, we are left with a term that depends on the difference dipole moment, also denoted $\Delta\mu$. This means that a vibrational transition can only be observed if it is accompanied by a change in the dipole moment.

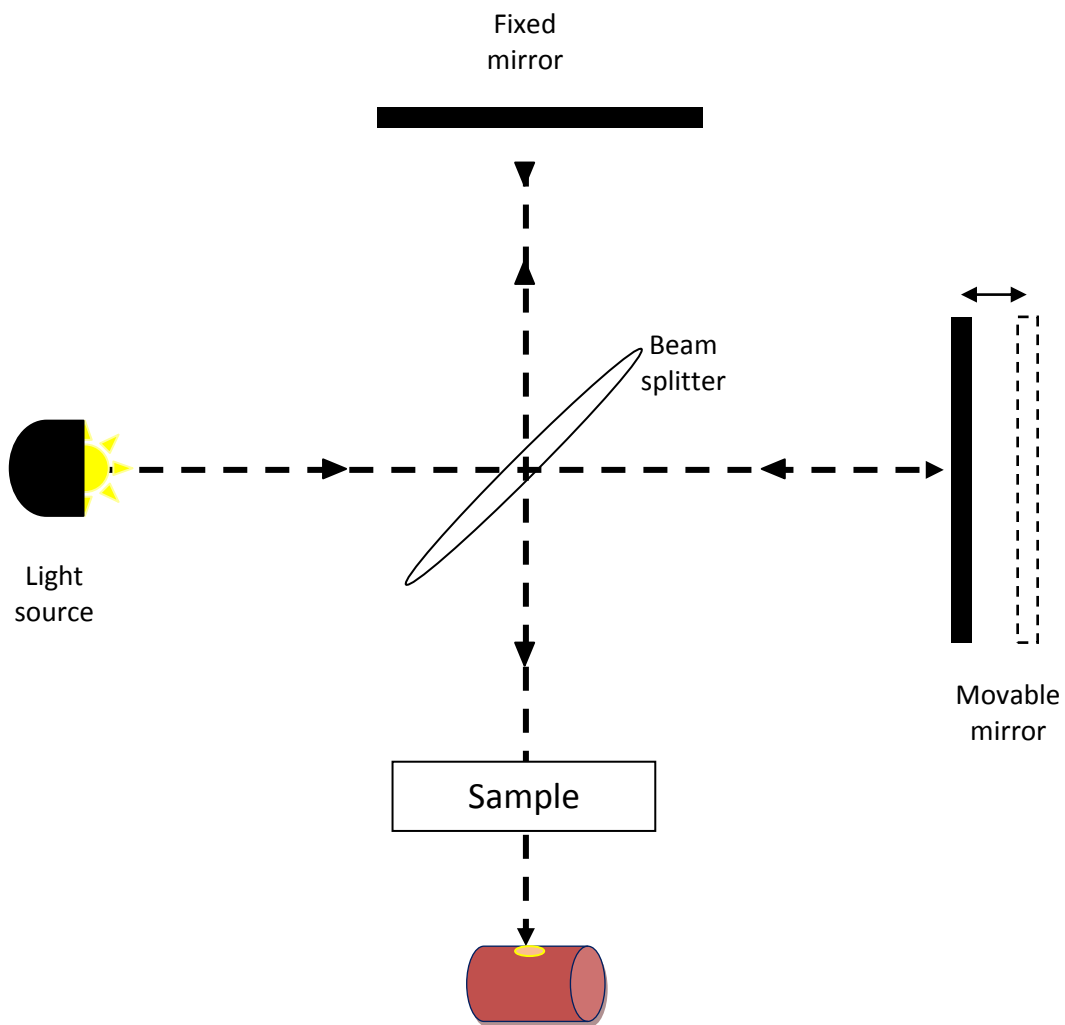


Figure 2.5.1. Scheme of a Michelson interferometer, the main component of an FTIR spectrometer.

2.5.2 FTIR spectroscopy

When a light of the appropriate frequencies is incident on a molecule, some of its energy will be absorbed by the molecule due to vibrational transitions. When scanning over a certain spectral range, this gives rise to an infra-red (IR) absorption spectrum. The light absorption A obeys the Beer-Lambert law:

$$(2.5.8) \quad A = -\log_{10} \frac{I}{I_0} = \epsilon dc$$

where I_0 is the intensity of the light source, I is the light intensity after having passed through the sample, ϵ is the molar absorptivity of the sample, d the length of the path the light has to go through and c is the concentration of the sample.

In IR spectroscopy, light in different frequencies passes through a sample and through a “background” (i.e. a setup featuring exactly the same as the sample setup, but without the analyte). The absorption is calculated in the same way as above, but this time I_0 is the intensity of the light after having passed the background setup. Transmission spectra can also be recorded, and the quantity measured in this case is:

$$(2.5.9) \quad T = \frac{I}{I_0}$$

The difference between IR spectroscopy and Fourier Transform IR (FTIR) is that in IR spectroscopy the light source is a monochromator shining one wavelength at a time, while in FTIR many wavelengths are used simultaneously, and are later separated by the mathematical transformation known as the Fourier transform.

An FTIR spectrometer is based on the Michelson interferometer, a device comprising a beam-splitter and two flat mirrors situated perpendicularly to each other (see Fig. 2.5.1). The beam-splitter is situated on the crossing of the two light beams, the one going from the light source to the moveable mirror and the other going from the fixed mirror to the detector. The fixed mirror, as suggested by its name, stays fixed during the measurement, while the movable mirror is moved towards the beam-splitter and away from it. The beam emanating from the light source is half transmitted and half reflected by the beam-splitter, so that it is effectively divided in two, and reflected by both mirrors. Then it recombines at the beam splitter, and moves on to the sample and detector. Since the optical path length the light beam passes is determined by the

position of the mirrors, a difference in the optical path length between the two mirrors is created as the movable mirror is moved. That difference is called the “optical path difference” (OPD) or “optical retardation” (δ). At $\delta=0$, the optical path length of the two mirrors is identical, so that the beams are in phase when they meet at the beam-splitter, and constructive interference results. This means that when the movable mirror is at the 0 position, the maximal amount of light reaches the detector and the signal intensity is high. For a monochromatic light source:

$$(2.5.10) \quad I_{(\delta,\tilde{\nu})} = I_{(\tilde{\nu})}[1 + \cos(2\pi\tilde{\nu}\delta)]$$

When $\delta=\lambda/4$, the light intensity reaching the detector is zero, and when it reaches $\lambda/2$, the light intensity is maximal again. By moving the movable mirror in pre-determined fractions and recording the light intensity reaching the detector, an interferogram is obtained, which is a graph of the light intensity at the detector vs. δ . When a polychromatic light source is used, the highest intensity is obtained for $\delta=0$, since this is the only δ for which the cosines of all the different wavelengths are equal to 1. This region in the interferogram is called “centerburst”.

For a polychromatic light source, the total light intensity at the detector is:

$$(2.5.11) \quad I_{(\delta)} = \int_0^{\infty} I_{(\delta,\tilde{\nu})} d\tilde{\nu} = \int_0^{\infty} I_{(\tilde{\nu})}[1 + \cos(2\pi\tilde{\nu}\delta)] d\tilde{\nu}$$

To obtain a spectrogram, one can easily extract the frequency domain out of the bulk polychromatic light intensity recorded at the detector, using an inverse cosine Fourier transform:

$$(2.5.12) \quad I_{(\tilde{\nu})} = 4 \int_0^{\infty} [I_{(\delta)} - \frac{1}{2}I_{(\delta=0)}] \cos(2\pi\tilde{\nu}\delta) d\delta$$

2.5.3 FTIR in ATR mode

In attenuated total reflectance (ATR), the IR beam hits the curved part of a semi-cylindrical prism, or the sloped wall of a trapezoidal one, so that the angle of its incidence on the planar wall of the prism is greater than the critical angle for this wavelength in the specific medium of the prism. If the medium on the other side of the

prism has a smaller index of refraction than that of the prism, a standing wave is produced in the prism, due to the multiple reflections of the light, back and forth from the prism walls. However, a portion of this standing wave propagates to the less refractive medium, and is called the “evanescent wave”. The amplitude of the evanescent field decays exponentially with distance from the surface of the prism, as follows:

$$(2.5.13) \quad E = E_0 e^{-z/d_p}$$

where E_0 is the amplitude of the standing wave in the prism, z is the distance outside the prism surface, and:

$$(2.5.14) \quad d_p = \frac{\lambda}{2\pi n_1 \sqrt{\sin^2 \theta - \left(\frac{n_2}{n_1}\right)^2}}$$

where λ is the wavelength of the light, θ is the angle of incidence, and n_1 and n_2 are the refractive indices of the prism and of the medium the evanescent wave propagates in, respectively (Goormaghtigh et al. 1999). For an illustration, see fig. 2.5.2.

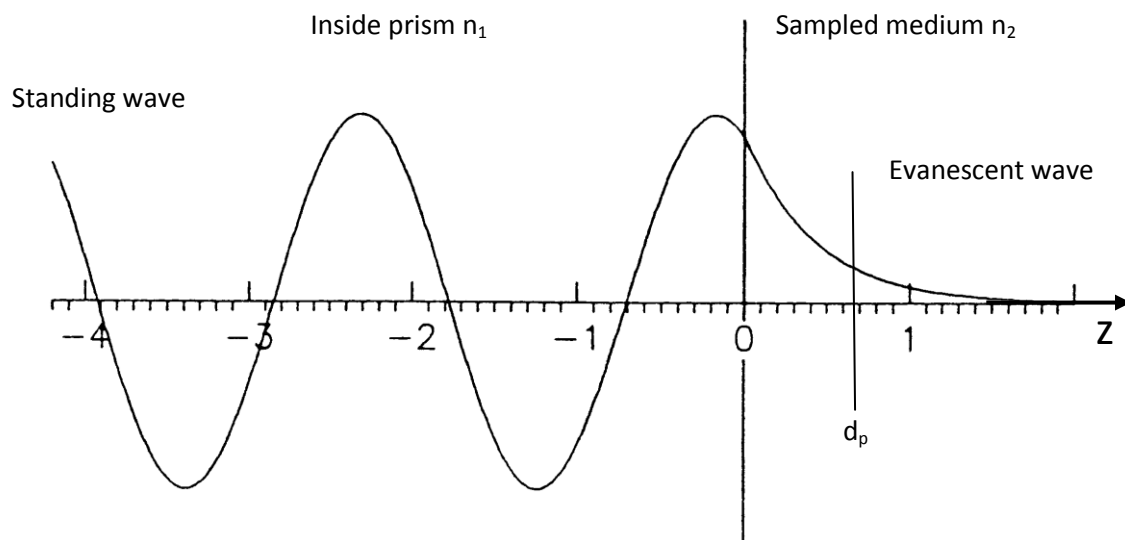


Figure 2.5.2. Scheme of the evanescent wave used for detection of species close to the surface in ATR-FTIR. Adapted from Goormaghtigh et al. (1999).

The evanescent wave can then be used to selectively probe species that are close to the prism surface (see Fig. 3.2.5). Prisms can be made of Ge, Si or ZnSe, with refractive indices of 4.0, 3.4 and 2.4, respectively. The penetration depth, d_p , varies according to the refractive index of the prism, the relevant wavelengths for the measurement and the angle of incidence. ATR-FTIR is commonly used as an easy and straightforward method to probe samples, whether surface-bound or otherwise deposited on it (Gershevit & Sukenik 2004; Goormaghtigh et al. 1999).

2.5.4 Surface Enhanced IR Absorption (SEIRA) Spectroscopy

Surface enhanced IR absorption (SEIRA) spectroscopy is performed by depositing a nano-structured metal film on a substrate, such as an ATR prism or a CaF window, coating it with the analyte and probing it with an IR beam, either in the form of ATR-FTIR or in the form of IR reflection-absorption spectroscopy (IR-RAS). Coinage metals are normally used (Osawa 2001; Miyake et al. 2002), but also other transition metals can be employed (Lu et al. 2000; Aroca & Price 1997; Bjerke et al. 1999). When compared to spectra of the same analyte adsorbed to the bare substrate or to the smooth metal, the reported enhancement factors for the relevant bands vary from 20-50 (Lu et al. 2000; Aroca & Price 1997; Bjerke et al. 1999) to 400-500 (Osawa 2001; Miyake et al. 2002; Schmidt 2006). This enhancement may be attributed to a combination of several factors, including: surface roughness, surface selection rule, electromagnetic mechanism and chemical enhancement.

The surface roughness of the metal film composed of metal islands can contribute to absorption intensity simply by allowing more analyte molecules to be attached to the surface. However, as reported surface roughness tends to range around 2.5-3.5 (Osawa 2001; Miyake et al. 2002; Lu et al. 2000), this cannot account for the entire enhancement. A discussion of the three other enhancement mechanisms follows.

2.5.4.1 Surface selection rule

The surface selection rule for IR absorption by molecules attached to a metal surface has been previously developed for IR-RAS measurements, according to the Fresnel Equations (Hoffmann 1983). The complex refractive index of the metal is $RI=n+ik$, while for the case of metals and IR radiation it may also be assumed that $n^2+k^2 \gg 1$. From the Fresnel equations one then obtains:

$$(2.5.15) \quad R_s = \frac{(n-\sec\phi)^2+k^2}{(n+\sec\phi)^2+k^2}$$

$$(2.5.16) \quad R_p = \frac{(n-\cos\phi)^2+k^2}{(n+\cos\phi)^2+k^2}$$

$$(2.5.17) \quad \tan(d_p - d_s) = \frac{2k \tan\phi \sin\phi}{\tan^2\phi - (n^2+k^2)}$$

where R_s and R_p are the reflected light intensity for s-polarized and p-polarized light, respectively. In p-polarized light the electric field component is perpendicular to the surface normal, while in s-polarized light it is parallel to the surface.

When plotting the phase shift vs. the angle of incidence, according to the above equations, the source of the surface selection rule becomes clear. For the s-polarized component of the light, there is a constant phase shift of ca. 180° upon reflection, resulting in destructive interference (see Fig. 2.5.3). Therefore, no s-polarized light is reflected, and the p-polarized component of the light alone can be used for detection. The result is that only vibrational modes whose dipole moments have a component parallel to the surface normal can be detected. Since SEIRA is subjected to the same surface selection rule, with the electric field of the p-polarized component parallel to the surface normal at each point on the metal nano-particles deposited on the substrate, the intensity of the absorbed IR radiation is proportional to the square of the cosine of the angle between the dipole moment of the probed vibrational mode and the surface normal, as follows:

$$(2.5.17) \quad I \propto \Gamma \left| \frac{d\mu}{dQ} \right|^2 |E_p|^2 \cos^2\theta$$

where θ is the angle between the difference dipole and the surface normal and Γ is the surface concentration of the analyte.

This means that vibrational modes oriented parallel to the surface normal will be enhanced 3-fold compared to randomly oriented vibrational modes.

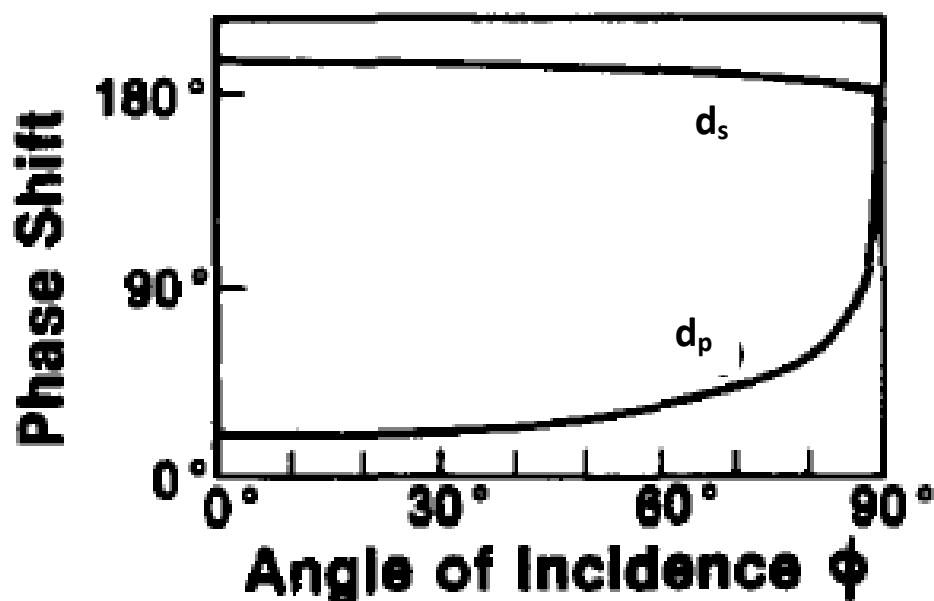


Figure 2.5.3. The phase shift in light reflected from a metal surface, as a function of the angle of incidence. d_s and d_p refer to the phase shifts in the s- and p- polarized components, respectively. From Hoffman [1983].

2.5.4.2 Chemical enhancement

Chemical enhancement may also play a part when attaching molecules, especially highly polarizable ones, to a metal surface, due to charge transfer from the metal to certain bonds in the molecule. This mechanism may be pertinent to the signal enhancement in the case of 4-mercaptobenzonitrile (MBN) directly attached to the metal surface, since this molecule is conjugated and has delocalized electrons and a polarizable nitrile function. In the case of proteins attached to the metal surface this enhancement mechanism is probably less significant. Furthermore, this mechanism is unlikely to

explain the enhancement of IR absorption intensities of an analyte adsorbed to a nano-structured surface, compared to the same analyte while adsorbed to the smooth metal, as observed by Bjerke and Griffiths (1999) for platinized vs. untreated platinum surfaces. The maximal enhancement factors that they report were 15-19, still too large to be attributable to the combination of surface roughness and molecular orientation. To explain these in full, one must turn to the electromagnetic mechanism.

2.5.4.3 The electromagnetic mechanism

When light is incident upon metal particles, its electric field component induces a dipole in delocalized electrons in the metal, and the dipole, in turn, induces an additional electromagnetic intensity in the same frequency, a phenomenon also known as localized surface plasmons (for illustration see fig. 2.5.4) (Osawa et al. 1993, 2002). If the particle is much smaller than the incident wavelength (which is the case in SEIRA), then the field induced by surface plasmons that are confined to the particles, i.e. to structures much smaller than the excitation wavelength, is enhanced compared to a field induced by plasmons in larger particles or in a continuous film (Schmidt 2006). Vibrational modes in the analyte layer close to the metal become excited by the total electric field, i.e. the sum of the incident and the induced electric field (Osawa 2001).

The size, shape and separation of metal particles in the metal film used for SEIRA play a crucial role in the electromagnetic enhancement. Effective medium approximations are used to describe the dielectric function of the metal-analyte-host system in terms of the polarizability of the metal islands, α . α depends on the dielectric functions of the metal islands, analyte and host medium, on the volume ratio between the coated and uncoated metal particle, and on the depolarization of the particles caused by their elliptic shapes (Osawa et al. 1993). The latter has been calculated by Stoner (1945). The Maxwell-Garnett effective medium approximation model affords the following dependence of the dielectric function on α :

$$(2.5.18) \quad \varepsilon_{MG} = \varepsilon_h \frac{3+2F\alpha}{3-F\alpha}$$

Where F is the packing density of the metal in the composite medium. The Maxwell-Garnett approximation is valid only for films where the metal islands do not form a

continuous film. To describe thicker, denser films, more elaborate models, such as the Bruggemann model, are needed (Osawa 2001, 1993).

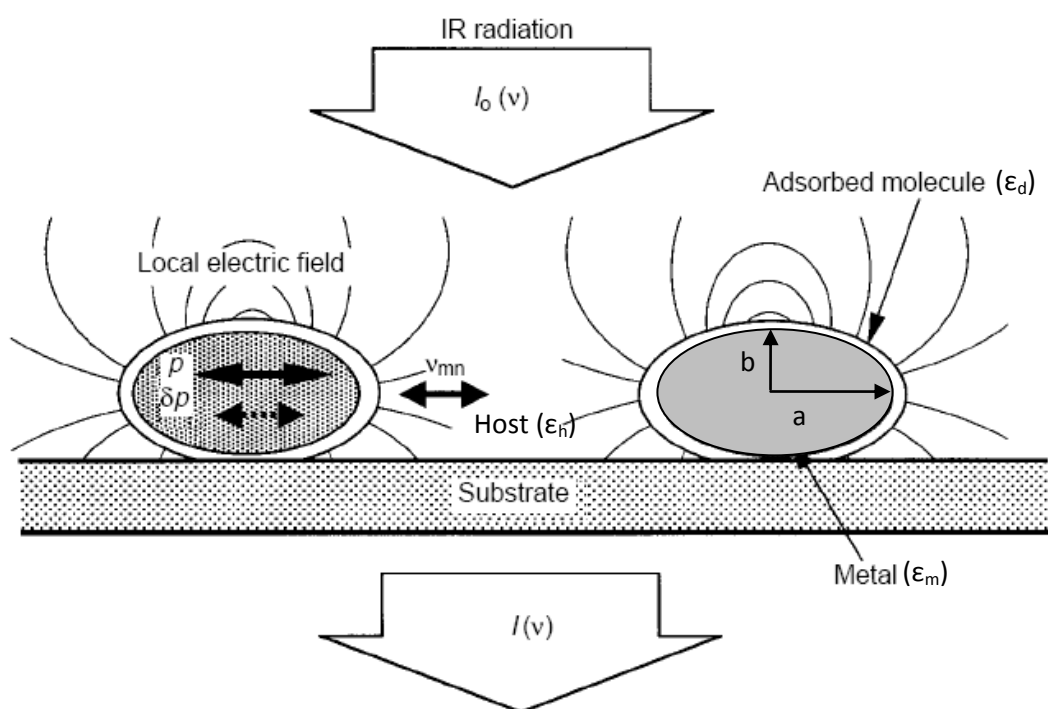


Figure 2.5.4. Illustration of the electromagnetic mechanism of SEIRA. Metal islands are deposited on a substrate and coated with a layer of analyte. The metal has a dielectric function of ϵ_m , the analyte of ϵ_d , and the host medium of ϵ_h . The incident electromagnetic radiation with an electric intensity I_0 produces an oscillating dipole p in the particle (also known as localized plasmon), which in turn generates an oscillating electric field in the same frequency. Incident radiation with the frequency ν_{mn} equal to that of a vibrational mode in the analyte layer excites those vibrational modes, inducing an additional dipole δp in the metal island. a and b are the lengths of two axes of the ellipsoid metal particles. Adapted from Osawa (2001).

2.5.5 Surface Enhanced Raman Spectroscopy (SERS)

Surface enhanced Raman spectroscopy (SERS) has preceded SEIRA and is in more common use, perhaps thanks to the greater simplicity of surface preparation (no ATR crystal required), or to the larger enhancement, which can reach over five orders of magnitude. SERS is performed predominantly on nanostructured Ag, either in colloidal form (Sivanesan et al. 2011), or on roughened Ag surfaces (Ly et al. 2011). In SERS the enhancement can be also attributed to a chemical effect (up to 100-fold enhancement) (Haynes et al. 2005), but more importantly to an electromagnetic mechanism arising from the excitation of localized surface plasmons in metal particles subjected to electromagnetic radiation of a wavelength much larger than the particle size. When radiation in an adequate frequency range is incident upon such particles, the conductance electrons start resonating with the radiation, creating a dipole in the particle, and therefore an induced electric field, $E_{ind(\nu_0)}$, which depends on the exciting field, $E_{0(\nu_0)}$, as follows:

$$(2.5.18) \quad E_{ind(\nu_0)} = 2 \cdot E_{0(\nu_0)} \frac{\tilde{\epsilon}_r(\nu_0)^{-1}}{\tilde{\epsilon}_r(\nu_0)^{+2}}$$

where $\tilde{\epsilon}_r(\nu_0)$ is the product between the complex frequency dependent dielectric constant of the metal and the square of the refractive index of the surrounding medium. The enhancement therefore depends on the refractive index of the metal and the radiation frequency. The best results are obtained for Ag at 400 nm and for Au at 560 nm. However, not only the incident radiation is enhanced in this way, but also the Raman scattered radiation. Since the light intensity is proportional to the square of the electric field component, it arises that even for a 10-fold enhancement of the electric field, an enhancement of 10^4 of the Raman signal results (Siebert & Hildebrandt 2007). In SERS the same surface selection rule described for SEIRA exists.

2.6 The Vibrational Stark Effect

The Stark effect is the term used to describe a phenomenon where the absorption frequency of certain transitions is affected by local (static) electric fields (synonyms are electrochromism, electroabsorption and electro-optic absorption) (Bublitz & Boxer 1997). The vibrational Stark effect (VSE) refers to changes in the vibrational transition frequencies of certain modes, according to:

$$(2.6.1) \quad \nu = \nu_0 - \Delta\vec{\mu} \cdot \vec{F} - \frac{1}{2} \vec{F} \cdot \Delta\vec{\alpha} \cdot \vec{F}$$

where ν and ν_0 are the vibrational frequencies of the mode in the presence and in the absence of the electric field F , respectively, $\Delta\mu$ is the difference dipole moment of the mode, and $\Delta\alpha$ its difference polarizability between the ground and excited states (Andrews & Boxer 2000). Since for cases where the quadratic term can be neglected (linear VSE regime), the difference dipole moment describes the sensitivity of the mode to electric fields, $\Delta\mu$ is also often referred to as the “Stark tuning rate”.

$\Delta\mu$ for many classes of compounds has been determined by the Boxer group in Stanford University, by dissolving the compound in an organic solvent, e.g. 2-methyltetrahydrofuran (Me-THF), and creating a slab of frozen amorphous glass of the solution, sandwiched between the windows of a spectro-electrochemical FTIR cell (Bublitz & Boxer 1997; Andrews & Boxer 2000; Suydam & Boxer 2003). Since the modes immobilized in the frozen glass are isotropically oriented, for some molecules their frequency is red- and for some blue-shifted under the influence of the directional electric field (while for some it remains unchanged). The result is a peak shape that can be described as the sum of three peak derivatives – 0th, 1st and 2nd - centered at the same frequency ν_0 . By analyzing the line-shape according to an analytical procedure (Andrews & Boxer 2000; Boxer 2009), the different components are determined and $\Delta\mu$ can be calculated. For a graphical illustration, see Figure 2.6.1. For $\Delta\mu$ for various compounds, see Table 2.6.1.

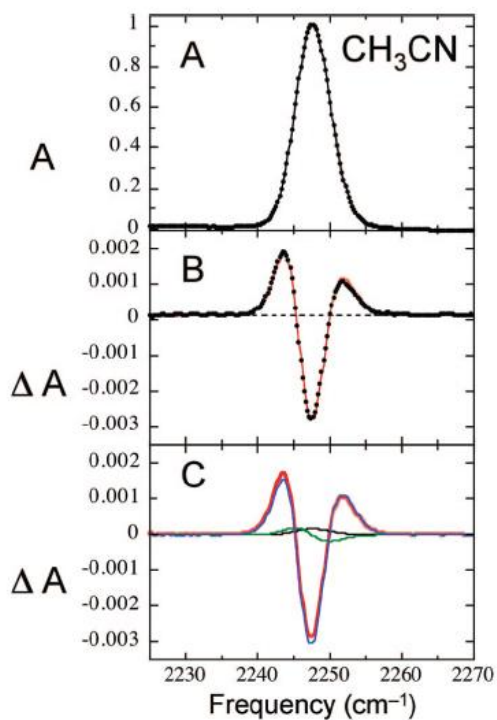
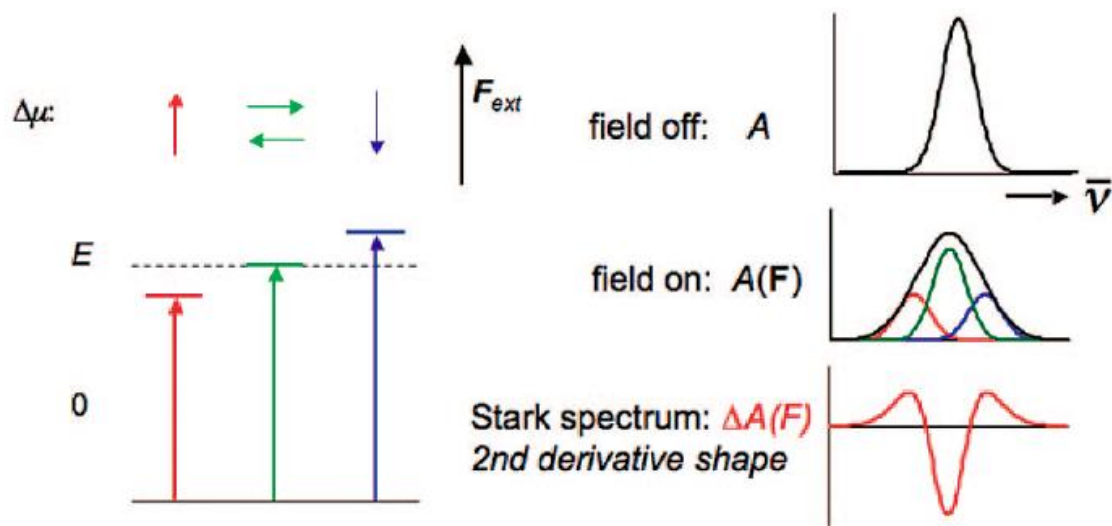


Figure 2.6.1. Stark effect in frozen film. **Top:** When applying an electric field to isotropically oriented modes, some experience a red shift, and some a blue shift, resulting in a difference absorption spectrum named a Stark spectrum. **Right: A)** Vibrational spectrum of CH_3CN ; **B)** Stark spectrum of CH_3CN ; **C)** The shape of the Stark spectrum can be described as the sum of 0th (black), 1st (green) and 2nd (red) derivatives, which can then be analytically calculated to provide the Stark tuning rate for the mode. Figure taken from Boxer (Boxer 2009).

Table 2.6.1. Zero field vibrational frequency and Stark tuning rate for various modes under different conditions

Compound	Conditions	Stretch mode	Peak position (cm ⁻¹)	$\Delta\bar{\mu}$ (cm ⁻¹ /V/m)
Fluorobenzene ^a	Me-THF frozen glass	C-F	1214.2	$8.4 \cdot 10^{-9}$
3-fluoropyridine	Me-THF frozen glass	C-F	1223.6	$4.0 \cdot 10^{-9}$
1-fluoro-4-nitrobenzene ^a	Me-THF frozen glass	NO ₂	1530	$12.6 \cdot 10^{-9}$
4-cyanopyridine ^a	Me-THF frozen glass	C≡N	2237.2	$4.2 \cdot 10^{-9}$
<i>p</i> -tuloidine ^a	Me-THF frozen glass	C≡N	2227.2	$7.1 \cdot 10^{-9}$
4-mercaptobenzonitrile (MBN) ^a	Me-THF frozen glass	C≡N	2227.9	$7.4 \cdot 10^{-9}$
<i>p</i> -amino-benzonitrile ^b	Me-THF frozen glass	C≡N	2207	$11.8 \cdot 10^{-9}$
EtSCN ^c	Me-THF frozen glass	C≡N	2156	$7.2 \cdot 10^{-9}$
KSI-SCN hydrophobic environment ^c	50% glycerol/water	C≡N	2156	$7.0 \cdot 10^{-9}$
KSI-SCN hydrophilic environment ^c	50% glycerol/water	C≡N	2168	$5.8 \cdot 10^{-9}$

^a Suydam and Boxer (2003)

^b Levinson et al. (2012)

^c Fafarman et al. (2012), KSI = ketosteroid isomerase

2.6.1 Sensitivities of the nitrile stretch

Thanks to its relatively high Stark tuning rate and its conveniently located stretching frequency, away from absorptions of other modes pertinent to biophysical research, the nitrile stretch has been extensively used for VSE-based measurements of electric fields in the active sites of various proteins (Fafarman et al. 2012; Fafarman et al. 2006; Fafarman & Boxer 2010; Suydam et al. 2006; Jo et al. 2010). In this work it is used for probing electric fields on protein surfaces and at SAM interfaces (Schkolnik, Salewski, et al. 2012; Schkolnik, Utesch, et al. 2012). It is, however, important to note that in order to be able to quantify the local electric field according to eq. 2.6.1, measuring ν is not sufficient, as ν_0 and $\Delta\mu$ under the conditions of the measurement must be known, as well as the angle between the two vectors $\Delta\mu$ and F .

2.6.1.1 The nitrile tuning rate

As seen in Table 2.6.1, the tuning rate is dependent on the hydrophilicity of the environment the VSE probe is exposed to, and possibly also, to a lesser extent, on the molecule it is attached to. Unfortunately, the number of literature resources on this

issue is limited, and so the available literature (Fafarman et al. 2012) will be used for estimating approximated tuning rate values in this work.

2.6.1.2 Phase and solvent effects

In nitriles, the vibrational frequency in the absence of electric field, ν_0 , is affected by various factors, such as the substrate the molecule is attached to (see sections 4.1 and 4.3.4), its phase and solvent interactions. For example, benzonitrile has a vibrational frequency of 2238 cm^{-1} in the gas phase (Stein 2003), but of 2226 cm^{-1} in DMSO and 2236 cm^{-1} in water (Fafarman & Boxer 2010). For 4-mercaptobenzonitrile (MBN), the Stark probe used in this work, the vibrational frequency is 2226 cm^{-1} in the solid phase and 2228 cm^{-1} in DMSO (Schkolnik, Utesch, et al. 2012). In an aqueous solution, the nitrile stretching frequency of free MBN was determined to be 2233.6 (Schkolnik, Salewski, et al. 2012). These solvation effects are divided into protic and aprotic solvation effects, arising from hydrogen bonding interactions and from solvation field, respectively (Aschaffenburg & Moog 2009).

For aprotic solvents, the effect arises from the polarizability of the nitrile bond and from the permittivity of the solvent, as described by the Onsager (or reaction) field:

$$(2.6.2) \quad F_{\text{Onsager}} = \frac{\mu_0}{a^3} \left[\frac{2(\epsilon-1)(n^2+2)}{3(2\epsilon+n^2)} \right]$$

where F_{Onsager} is the field experienced by the nitrile due to solvation, as the solute occupies a spherical cavity of radius a in a continuous dielectric medium representing the solvent. μ_0 is the gas-phase dipole moment of the solute, and n is its refractive index. ϵ is the dielectric constant of the solvent (Levinson et al. 2012). According to Levinson et al. (2012), for several aromatic nitriles in a series of aprotic solvents, when plotting the vibrational frequency of the nitrile stretch in each solvent against the Onsager field, as described in Eq. 2.6.2, a linear correlation is found, where the slope is equal to the Stark tuning rate. These results are in line with those of Aschaffenburg and Moog (2009), who have been able to reach a similar correlation for benzonitrile in different solvents. They have also shown that for protic solvents, while the reaction field effect remains, an asymmetric broadening of the peaks and their shift to higher frequencies are caused by hydrogen bonding interactions of the nitrile with the solvent.

Ghosh et al. (2009) have reported similar findings obtained by 2D IR for benzonitrile in different solvents. In both works the nitrile stretch in organic protic solvents is composed of two peaks: the solvated (at ca. 2230 cm^{-1}) and the hydrogen bonded (at ca. 2235 cm^{-1}) nitrile stretches, whereas in water the peak is more symmetric and appears at 2236 cm^{-1} (Ghosh et al. 2009). To explain these findings, quantum mechanical considerations must be invoked. From *ab initio* calculations performed by Cho et al. (1998) for acetonitrile, it seems that upon hydrogen bonding, which occurs with the nitrile nitrogen as an electron donor, electron density is transferred from an anti-bonding orbital that the nitrogen lone pair is involved in, reducing the anti-bonding character of the nitrile bond. As the anti-bonding character of the nitrile bond decreases, the bond becomes stronger, and the stretching force constant becomes larger, causing an increase in the vibrational frequency (see section 2.5.1). The effect is quite dramatic, and can cause a blue shift of ca. 10 cm^{-1} (Fafarman et al. 2010; Aschaffenburg & Moog 2009; Ghosh et al. 2009).

Materials and Methods

3.1 FTIR

3.1.1 For Cytochrome *c*

For all measurements involving Cytochrome *c* (Cyt-*c*), Fourier Transform Infra-red (FTIR) spectra were recorded in the Technische Universität Berlin using a Bruker Tensor 27 spectrometer, equipped with a liquid nitrogen-cooled photoconductive MCT detector, at a spectral resolution of 4 cm⁻¹, while purging the sample compartment with dried air. The sample was held in a temperature-controlled (10°C) gas-tight IR cell for liquid samples (volume ~ 7 µL, path length = 50 µm), equipped with CaF₂ windows. 20,000 scans were accumulated for each spectrum. Each measurement was repeated twice and an average value is reported. The corresponding standard deviation is 0.15 cm⁻¹ for both mutants. Peak positions in the IR spectra were determined either using a second derivative of the peak or by fits of Gaussian functions to the spectra after background subtraction. Both approaches yield identical results. Note that there are variations in the shape of the peak due to an asymmetric broadening. Therefore, in order to perform a fit, in some cases additional Gaussian functions with weak amplitudes are required. For the analysis, only the main peak frequency was considered. For an example, see Figure 4.2.1.

3.1.2 For Dehaloperoxidase (DHP) and the Stark label in solution

For all measurements involving hemoglobin-dehaloperoxidase A (DHP A) or bound and unbound 4-mercaptobenzonitrile (MBN) in different solutions, FTIR measurements were performed at the North Carolina State University (NCSU) in a split-beam cell for liquid samples (path length 25 µm) equipped with CaF₂ windows, using a Digilabs FTS-6000 spectrometer with a photoconductive MCT detector. The spectral resolution was 2 cm⁻¹. The spectrometer was purged with dry air. 1,000-1,500 scans were accumulated for each spectrum.

For measurement of labelled DHP mutants, the split beam cell was loaded with the labelled wild type (WT) protein in one compartment and a labelled mutant in the other,

to enable comparison of the MBN nitrile stretching frequency in the mutant with that of the WT protein. A spectrum of the split beam cell compartment loaded with the relevant buffer was used for background subtraction, to obtain an absorption spectrum.

The MBN nitrile stretching band position was determined by Gaussian peak fit, after baseline subtraction of the absorption spectrum. Each mutant was measured 5 times and averaged. The mean standard deviation was determined to be $\pm 0.1 \text{ cm}^{-1}$.

3.2 Spectro-electrochemistry in a Surface Enhanced IR Absorption (SEIRA) setup

3.2.1 SEIRA setup

The spectro-electrochemical cell used for surface enhanced IR absorption (SEIRA) measurements, sometimes at an applied potential or concomitantly with cyclic voltammetry, was constructed according to a design previously described (Miyake et al. 2002; Ataka & Heberle 2007; Wisitruangsakul et al. 2008; Schkolnik, Utesch, et al. 2012). In short, it consisted of a hemi-cylindrical or trapezoidal Si ATR (attenuated total reflectance) prism, on top of which a gold film was deposited (see section 3.2.2). The gold film was nano-structured by electrochemical cycling (see section 3.2.3), which provided surface enhancement of the IR signal for species attached to the surface. At the same time, by physical contact with a gold plate fastened to the coated ATR prism as well as the electrochemical cylindrical glass cell by two O-rings, the gold film also served as the working electrode (WE) for a three-electrode electrochemical cell. The reference electrode (RE) in all our experiments was Ag/AgCl stored in 3 M KCl (>99.5% Sigma), and the counter electrode (CE) was a platinum wire attached to platinum mesh. The cell was sealed with a septum, and purged with Ar using two syringe needles, for inlet and outlet. The diameter of the Au film exposed to the solution was ca. 8 mm, and the working volume of the cell was 3 mL.

SEIRA spectra were recorded at a range from 4000 to 1000 cm^{-1} , with a spectral resolution of 4 cm^{-1} on a Bruker IFS66v/s spectrometer or a Bruker Tensor 27

spectrometer, both equipped with a photoconductive MCT detector. 400 scans were co-added for each spectrum. Electrode potentials were controlled by an Autolab PGSTAT 12 potentiostat with its GPES software.

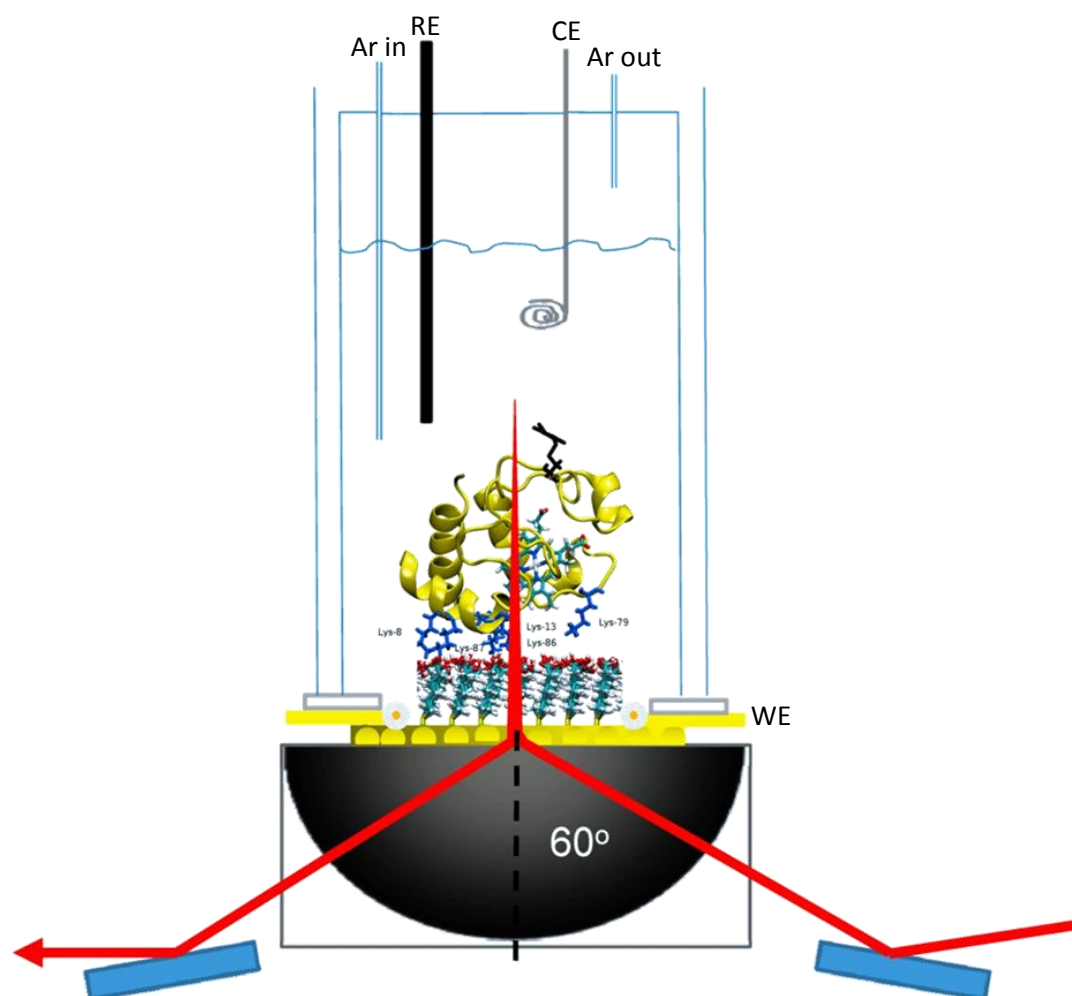
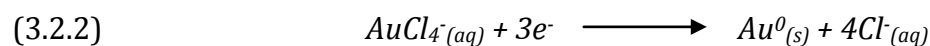
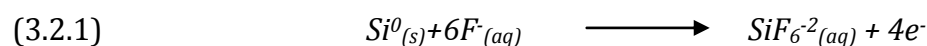


Figure 3.2.1 Rough sketch of the SEIRA setup. The spectro-electrochemical cell was set on the flat side of an ATR Si prism, on top of which a nano-structured Au film had been deposited. The Au film is used simultaneously for surface enhancement of the IR signal and as a working electrode, through contact with a gold plate (yellow slabs). The gold film can also be SAM-modified, and depending on the SAM composition, a protein such as Cyt-c can be immobilized on it for spectro-electrochemical measurements. Such measurements can also be performed on MBN, either while attached to the protein or as a SAM component.

3.2.2 Gold film deposition

Electroless deposition, as described by Miyake et al (2002), was employed in order to deposit a gold film on a Si prism, to be used simultaneously as a working electrode and a surface for SEIRA measurements (see above). The Si prism was either cylindrical or trapezoidal, measuring, in both cases, 20 x 25 x 10 mm (W x L x H). All glassware was soaked in 1:1 HNO₃:H₂SO₄ (conc.) at least overnight prior to use in the following procedure. The planar face of the Si prism was polished by rubbing it with aluminum oxide slurry (1-5 μm grain size), for 2 min or till the surface seemed totally non-wetting to water (Milli-Q, resistivity > 18 MΩ). Then the prism was rinsed with Milli-Q water, and subsequently submerged in 40% wt. NH₄F for 2 min. This was done to remove the oxide layer existing on the Si surface, so that the Si surface became H-terminated. Then the prism was washed with water again and placed in a water tub thermostated at 65°C. The following plating solution: 0.3 M Na₂SO₃ + 0.1 M Na₂S₂O₃·5H₂O + 0.1 M NH₄Cl (all Sigma) was mixed with 0.03 M NaCl₄Au·2H₂O (99%, Aldrich) and HF 2% (v/v, Fluka), at 1:1:1 (v/v). The final mixture was dropped onto the H-terminated Si surface using a pipette, and left to act for 45 sec, or till an Au film was formed on the Si to a thickness not too great to still discern the blackness of the Si surface under it. The reactions by which the Au film was created are:



To stop the reaction after formation of the Au film, the plating mixture-droplet was washed away from the surface with water.

3.2.3 Gold film electrochemical cleaning

After Au film formation, the prism was incorporated in the SEIRA cell setup, as described in section 3.2.1, and the spectro-electrochemical cell was filled with 3 mL H_2SO_4 0.1 M. After connecting the reference, counter and working electrodes (the latter being the deposited Au film), cyclic voltammetry (CV) of the Au surface was performed, with initial potential at 0.1 V and vertex potential at 1.4 V (both vs. Ag/AgCl), at 0.05 V/s. The CV was repeated 6 times (see Figure 3.2.2 for a typical cyclic voltammogram). The first scan served to remove impurities from the surface by electrochemically oxidizing organic species, whereas the subsequent scans were used also to nano-structure the Au surface, as in every cycle of Au oxidation and reduction the Au is organized in nano-beads on the Au film surface (Leopold 2000). All CVs were performed under Ar. The solution was first bubbled with Ar for 15 min before scanning, and while scanning an Ar atmosphere was maintained above the solution. However, strictly anaerobic conditions could not be achieved, such that often residual oxygen species developed in the solution in the progress of the 6 scans, as can be seen from the peak at 1.1 V in Fig. 3.2.2.

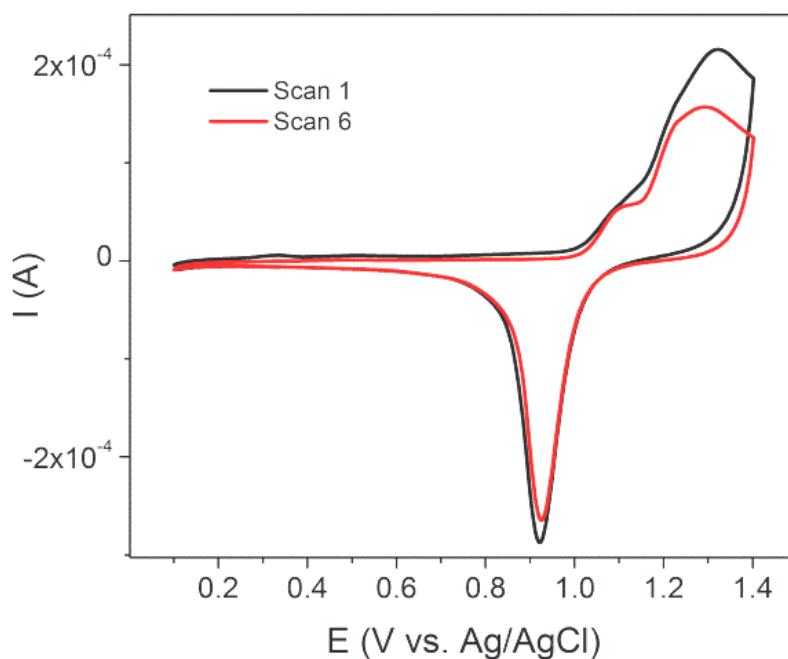


Figure 3.2.2 Cyclic voltammogram of bare gold film in H_2SO_4 0.1 M. On the first scan (black) impurities are oxidized, and by the 6th scan (red) the only peaks seen are those of Au oxidation and reduction, and that of the residual oxygen species in the solution.

3.2.4 SAM coating and protein adsorption

In order to coat the gold film serving as WE with a self assembled monolayer (SAM), the cell was incubated overnight with the respective SAM – mercaptohexanoic acid (MHA, Dojindo), 4-mercaptobenzonitrile (MBN, Apin Chemicals), or thiophenol (TP, Aldrich) – dissolved at ~ 1 mM in either spectroscopy grade ethanol (in the case of MHA. Ethanol purchased from Merck) or in anhydrous dimethylsulfoxide (DMSO, used in the case of MBN or TP. DMSO purchased from Fluka). The next day the cell was successively washed with DMSO (if used for SAM deposition), ethanol and Milli-Q water, and filled with 10 mM potassium phosphate buffer, pH=7.0 (henceforth denoted as “buffer”; KH_2PO_4 and K_2HPO_4 >99% purchased from Merck) unless otherwise reported. According to the nature of the planned measurements, a background SEIRA spectrum was recorded either or both before SAM deposition and/or after the cell was filled with buffer.

In order to prepare a mixed SAM, the initial SAM (MHA or TP) was deposited as described above, and the cell filled with buffer. Then MBN was added to the cell to reach a final nanomolar concentration. This was performed under a controlled potential, serving to partly reduce the existing SAM and allow the exchange of some of its monomers with MBN molecules. For further details, see section 4.3.

Some of the measurements (see section 4.2) were conducted with MBN-labeled cytochrome *c* (Cyt-*c*) variants electrostatically bound to a MHA SAM (see Fig. 3.2.1 for an illustration of the resulting setup). To do so, a solution of the protein in sodium phosphate buffer (150 mM, pH=7.0), supplied by Katalin Tenger from the Zimányi group at the Institute of Biophysics, Biological Research Center, Szeged, Hungary (Schkolnik, Utesch, et al. 2012), was added to the buffer-filled cell, after SAM adsorption, to a final concentration of 2 μM . Protein adsorption was immediately detectable by the prominent amide I and amide II bands in the SEIRA spectra (see Fig. 4.2.1). After about 30 min of protein adsorption, the cell was washed three times with buffer and a spectrum was recorded to make sure that the protein was indeed bound to the surface. As seen in Fig. 3.2.3, although the amide peaks diminish slightly due to re-equilibration of the bound protein with the protein-free solution, Cyt-*c* is clearly bound to the MHA

SAM. To make sure the protein had not been denatured, its function was determined by either CV or redox titration (see Fig. 4.2.3).

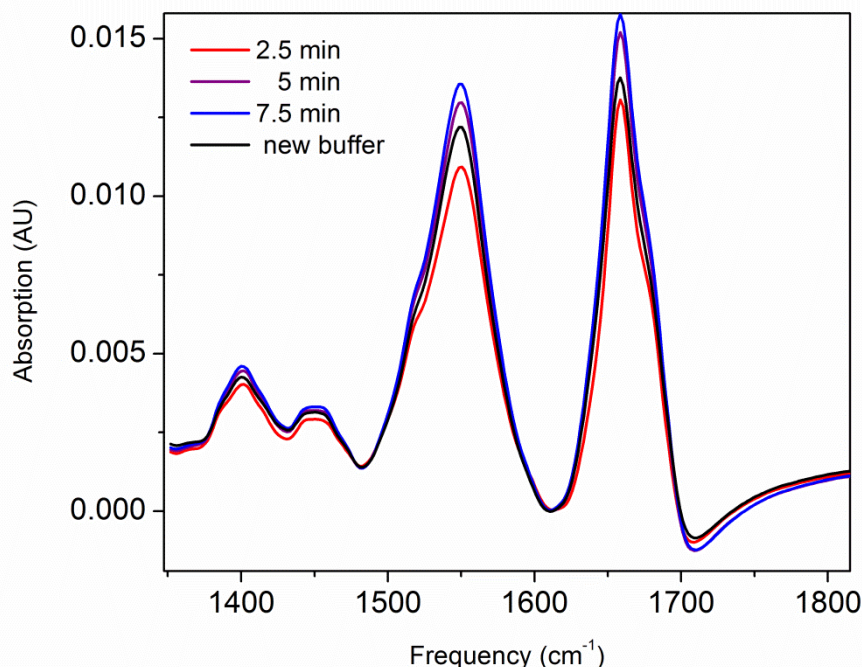


Figure 3.2.3 SEIRA spectra following the adsorption of Cyt-c to MHA SAM in spectro-electrochemical cell. Red, purple and blue: protein adsorption after 2.5, 5 and 7.5 min, respectively. Amide I and Amide II bands at 1549 and 1658 cm⁻¹, respectively, gradually increase in intensity as the protein adsorbs to SAM. Black: After the cell has been washed with buffer and filled with new buffer free of protein, the Amide bands diminish slightly, as the adsorbed protein re-equilibrates with the protein-free buffer. The protein, however, remains adsorbed to the SAM.

3.2.5 Cyclic Voltammetry in the SEIRA cell

Cyclic voltammetry (CV) was performed in the SEIRA spectro-electrochemical cell to ascertain SAM adsorption/desorption (see section 4.3), or to ensure Cyt-c activity (see section 4.2). Electrode potentials were controlled by an Autolab PGSTAT 12 potentiostat, using the instrument's GPES software installed on a PC. Buffer was used as electrolyte. All potentials reported were measured against an Ag/AgCl RE stored in KCl 3 M solution. All CVs were repeated 3 times, and the second CV was used for evaluation. The scan rate used was 0.05 V/s, unless stated otherwise.

3.2.6 Redox titration of Cyt-c in the SEIRA cell

In order to ensure Cyt-c activity, also redox titration was performed for SAM-attached Cyt-c in the SEIRA cell. To this end, potentials from -80 to +100 mV (vs. Ag/AgCl) were applied, at a 20 mV step, and at each potential a SEIRA spectrum was recorded. The spectrum recorded at -80 mV was used as the reference spectrum, and was subtracted from all the other spectra, in order to obtain a series of spectra demonstrating structural changes to the protein during oxidation.

3.2.7 Data analysis

Two methods were used to determine nitrile stretching (and other) peak positions. Either a second derivative was calculated using the Savitzky-Golay algorithm, supplied by the OPUS software (Bruker) with a smoothing of 9 points; or a multi-Gaussian peak fit was obtained after baseline subtraction, both done using the Peak Analyzer tool found in OriginPro 8.0 software. Both methods give essentially identical results (see Fig. 4.2.1 b).

3.3 DHP production and purification

3.3.1 Protein growth

For Cyt-c, mutants were prepared, produced and purified by Katalin Tenger at the Institute of Biophysics, Biological Research Centre, Szeged, Hungary, as described by Schkolnik, Utesch et al. (2012).

For DHP A, mutants were prepared by Junjie Zhao, according to the procedure described in Zhao et al (2012). Single colonies of either the wild type or mutants were isolated and transferred to 2mL starter growth vials containing LB broth (Miller) and 100 µg/mL ampicillin (Fisher. 3 vials in total for each batch). These 2 mL growth vials

were incubated for about 8 hours at 37° C. 1 mL from each starter growth vial was then used to inoculate a 1 L flask (6 flasks in total for each batch) of 2xYT broth (Fisher) containing 100 µg/mL of ampicillin. The 6 flasks were incubated at 37° C while shaking for 15 hours. The cells were collected by centrifugation at 7000 rpm and 4° C for 20 minutes and then frozen overnight at -20° C.

3.3.2 Purification of 6XHisDHP.

The frozen E. coli cell pellet produced as described above was re-suspended in lysis buffer at 2 mL/gram-cell-pellet (Lysis buffer composition: 50 mM NaH₂PO₄, 98%, Acros; 300 mM NaCl 99%, VWR; 10 mM imidazole 99.4%, Fisher; buffer pH=8) and lysozyme (Sigma) was added to a final concentration of 1 g/L. 500 µL of DNase I (10 g/L, Roche) and RNase A (16 g/L, Roche) were added. The cell slurry was stirred at 4° C for at least 1 hour. The cells were centrifuged at 18000 rpm for 45 minutes, and the supernatant was collected. The crude DHP solution was applied to a Ni-NTA agarose column (VWR), washed with a washing buffer (50 mM NaH₂PO₄, 300 mM NaCl, 20 mM imidazole, pH 8), and eluted with an elution buffer (50 mM NaH₂PO₄, 300 mM NaCl, 250 mM imidazole, pH 8). The 6XHis DHP isolated from the column was oxidized by mixing with an excess potassium ferricyanide (K₃[Fe(CN)₆]). Excess oxidant was removed by gel filtration using a Sephadex G-25 size separation column, which at the same time served for the purpose of buffer exchange, into 10 mM potassium phosphate buffer (Dipotassium hydrogen phosphate, K₂HPO₄, ≥ 99%, and potassium dihydrogen phosphate, KH₂PO₄, ≥ 99%, Fisher), pH=7.0.

3.4 Labeling with 4-mercaptobenzonitrile (MBN)

3.4.1 Labeling of NACME with MBN and measurement of free and NACME-attached MBN in different fractions of buffer:DMSO

4-mercaptobenzonitrile (MBN, Apin Chemicals, UK) bound to N-acetyl-*L*-cysteine-methyl-ester (NACME) was used as a proxy for protein-bound MBN. MBN was dissolved in anhydrous DMSO (Fluka) at 15 mM and divided into two glass vials. 15 mM NACME was added to one of them, and both were incubated in a shaker overnight. The vial not containing NACME was used as blank and to measure the IR spectrum of free MBN. FTIR measurements of the resulting solution were performed as described in section 3.1.2. Three repetitions were made, with pure DMSO serving as background. Fractions of KPb, from 10% to 90% (v/v) were added to the two solutions, and FTIR spectra were recorded for each fraction, with KPb:DMSO in the corresponding ratio as background. The STDEV over three measurements was $\pm 0.15 \text{ cm}^{-1}$ for NACME-MBN and $\pm 0.03 \text{ cm}^{-1}$ for pure MBN.

3.3.2 Protein labeling with MBN

For DHP A only (both WT and mutants), after having oxidized the protein (see 3.3.2), the oxidation state of the purified protein was verified by a UV/Vis measurement, using a Hewlett-Packard 8453 multi-wavelength spectrometer. Once it was determined that the Soret band of the protein was at $407 \pm 1 \text{ nm}$, a small excess of potassium cyanide was added to the mixture, so that it irreversibly bound to the heme, in order to avoid any uncontrolled changes to the oxidation state of the heme. A second UV/Vis measurement was performed to ascertain that the cyanide was bound to the heme, resulting in a Soret band at $423 \pm 1 \text{ nm}$.

For both proteins (either DHP A or Cyt-c, for both WT and mutants), a 100-fold molar excess of MBN dissolved in DMSO was added to the protein solution. The mixture was shaken overnight at 4° C . Centrifugation at 4,800 g was used to separate the protein-containing aqueous phase from the fraction of precipitated MBN. This step was

repeated at least 3 times, or until no more precipitate could be visually detected. Subsequently, the supernatant was dialyzed against potassium phosphate buffer, 10 mM, pH=7.0, in order to remove any residual unbound label, as well as for buffer exchange.

3.5 Surface enhanced Raman Spectroscopy in a spectro-electrochemical cell

Surface enhanced Raman Spectroscopy (SERS) measurements in an electrochemical setup have been conducted by Johannes Salewski at our group, as described in Schkolnik, Salewski et al. (2012), according to a procedure previously published (Murgida & Hildebrandt 2001). The cell was machined from Delrin featuring quartz windows. A rotating Ag ring served as the WE. Platinum and Ag/AgCl electrodes were used as counter and reference electrodes, respectively. Spectra were recorded with a confocal Raman spectrometer equipped with a liquid nitrogen cooled CCD detector, using the 413-nm excitation line of a Krypton ion laser, with a spectral resolution $> 2 \text{ cm}^{-1}$. The power of the focused laser beam on the sample was 1 mW. The accumulation time was 60 s. All SERS measurements were repeated four times.

3.6 Molecular dynamics simulations

All Molecular dynamics (MD) simulations discussed in this work have been performed by Tillmann Utesch in our group. MD simulations discussed in section 4.2 are described in detail in Schkolnik, Utesch et al. (2012), while those described in section 4.4 are as yet unpublished.

Results and Discussion

4.1 The Stark tuning rate and ν_0 in free and protein-bound, water exposed MBN

Measured by FTIR in solution, a nitrile stretching frequency in the absence of electric field (ν_0) of $2227.7 \pm 0.03 \text{ cm}^{-1}$ was observed for MBN dissolved in DMSO, in agreement with Schkolnik, Utesch et al. (2012) and Suydam and Boxer (2003). However, for NACME-MBN (N-acetyl-L-cysteine-methyl-ester-MBN), serving as an equivalent for uncharged-peptide bound MBN, the frequency was found to be $2226.8 \pm 0.15 \text{ cm}^{-1}$. The values refer to average and STDEV over 3 measurements. This implies that the binding of MBN to a cysteine causes a red-shift of about 1 cm^{-1} in its CN stretch frequency. This red shift may arise from changes caused to the nitrile bond by the loss of the thiol hydrogen and the formation of a disulfide bond between MBN and the NACME cysteine. Such a shift is to be expected also when attaching MBN to a cysteine residue on a protein surface.

The nitrile stretching in MBN is affected not only by binding the molecule to a substrate, but also by hydrogen bonding interactions (see also sections 2.6 and 4.4). In various nitriles, ν_0 has been reported to increase ca. 10 cm^{-1} in protic solvents, compared to aprotic ones (Aschaffenburg & Moog 2009; Ghosh et al. 2009; Fafarman et al. 2010; Levinson et al. 2012). This occurs since, in most configurations, hydrogen bonding removes electron density from the anti-bonding orbital of the nitrogen atom (Cho et al. 1998).

Since all our experiments were conducted in potassium phosphate buffer (10 mM, pH=7.0, see following sections), we wanted to measure ν_0 in cysteine-bound, buffer-exposed MBN, in the absence of external electric fields and charges. To do so, both MBN and NACME-MBN dissolved in DMSO were titrated with buffer, and changes to the nitrile stretching frequency were recorded (Fig. 4.1.1a). In both cases, the nitrile stretching frequency has linearly increased with increasing buffer content, in the range of 0-30% buffer in DMSO (v/v). At 40% buffer, both compounds started precipitating, and from 50% on, the observed frequency is that of solid MBN, at $2225.1\text{-}2225.9 \text{ cm}^{-1}$, as reported previously [2226 cm^{-1} measured by Raman for solid MBN (Schkolnik, Utesch et al. 2012)]. When fitting the linear portion of the titration curve (0-30%, Fig 4.1.1b) and extrapolating to 100% buffer, 2233.6 cm^{-1} is obtained for the nitrile stretch

in cysteine-bound, buffer-exposed MBN, which may serve as an approximated ν_0 for MBN in protein surface labeling. This is a reasonable value at 7 cm^{-1} blue-shift compared to cysteine bound MBN in DMSO, which agrees with the aforementioned increase in nitrile stretching frequency due to hydrogen bonding interactions. This value is also similar to that measured for peptide bound *p*-PheCN in buffer by Fafarman and Boxer (2010), which was 2231.5 cm^{-1} .

$\Delta\mu$, or the Stark tuning rate, has been previously determined to be $7.4 \times 10^{-9} \text{ cm}^{-1}/\text{V}/\text{m}$ for the nitrile stretching in MBN dissolved in 2-methyl-tetrahydrofuran (Me-THF) (Suydam & Boxer 2003). However, in a later work, the same group reported (Fafarman et al. 2012) that for protein-bound SCN, which was used as a Stark label, the tuning rate was $7.0 \times 10^{-9} \text{ cm}^{-1}/\text{V}/\text{m}$ when the protein-bound label was in a hydrophobic environment in the protein but $5.8 \times 10^{-9} \text{ cm}^{-1}/\text{V}/\text{m}$ when the label was exposed to the aqueous phase, and $6.7 \times 10^{-9} \text{ cm}^{-1}/\text{V}/\text{m}$ for a mixed hydrophilic-hydrophobic environment. A tuning rate of $7.2 \times 10^{-9} \text{ cm}^{-1}/\text{V}/\text{m}$ was found for SCN in Me-THF (Suydam & Boxer 2003). In the work itself (Fafarman et al. 2012) the authors dismiss these differences in the Stark tuning rate and claim that $\Delta\mu$ is “an intrinsic property” of the vibrational mode, however, no explanation is supplied to this assertion, and from the series of tuning rates, which decrease monotonically with increasing exposure to hydrogen bonding interactions over four measurements, we conclude that the Stark tuning rate is not constant, and that it, too, depends on the nature of the solvent the Stark label is exposed to. This is likely to arise from a decrease to the nitrile bond polarizability upon hydrogen bonding, due to the aforementioned removal of electron density from the anti-bonding orbital at the nitrogen atom (Cho et al. 1998).

This observation may be applied to MBN as well. In the absence of data concerning the tuning rate of MBN in a protic solvent, we use the ratio of the tuning rate of SCN in a protic solvent to that in Me-THF, to calculate $\Delta\mu$ for water-exposed MBN from the literature value which was measured for MBN in Me-THF. Thus we obtain $\Delta\mu = 6.0 \times 10^{-9} \text{ cm}^{-1}/\text{V}/\text{m}$ for MBN in an aqueous environment. This value is in agreement with the value of $5.9 \times 10^{-9} \text{ cm}^{-1}/\text{V}/\text{m}$ reported by Fafarman and Boxer (2010) for *p*-cyanophenylalanine-RNase in 50:50 glycerol:water (v/v), which may be considered as homologous to the protein-bound and water exposed MBN.

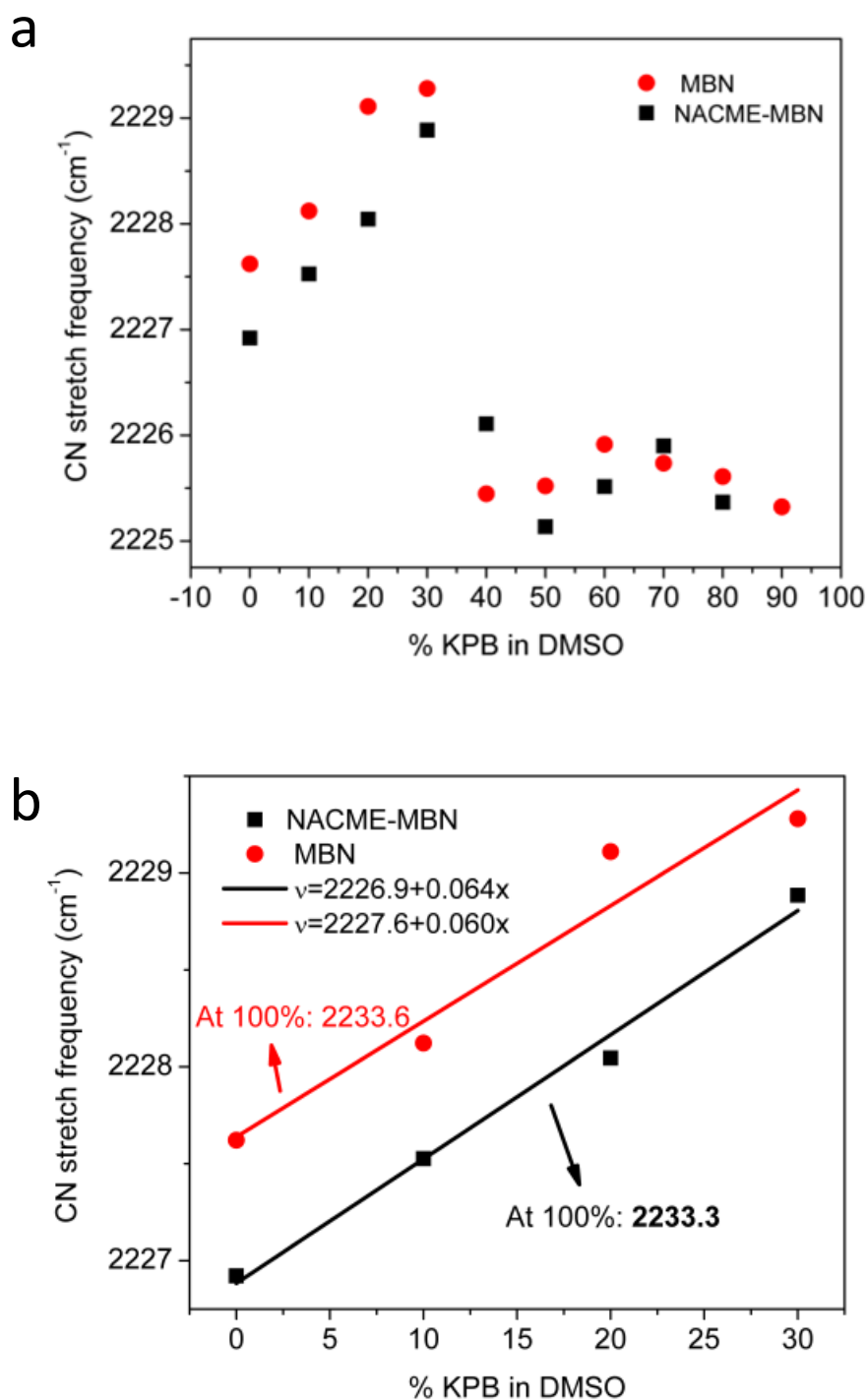


Figure 4.1.1. a) Titration graph for MBN and NACME-MBN dissolved in DMSO with fractions of potassium phosphate buffer (10 mM, pH=7.0). At first the nitrile stretching frequency increases linearly, as the involvement of the nitrile in hydrogen bonding interactions increases. At 40% buffer (v/v) the frequency drops to ca. 2225-2226 cm⁻¹ as these water insoluble compounds precipitate. b) Linear fit of the titration curve between 0 and 30% buffer, with values obtained from extrapolation to 100% KPB.

4.2 Using the Stark effect to probe electric fields on the surface of Cytochrome *c* variants in solution and at a SAM surface

In IR and SEIRA spectra of 4-mercaptobenzonitrile (MBN) labeled horse heart cytochrome *c* (Cyt-*c*) variants (K8C and K39C) in solution a weak but clearly identifiable peak is seen between the frequencies 2200 and 2300 cm^{-1} . There are no other peaks in this optical window, however it includes a strong background absorption (Fig. 4.2.1). This is why we have used the second derivatives of the spectra, where minima correspond to IR absorption peak maxima (Figs. 4.2.1). We have also tried to analyze the spectra using Gaussian fits after background subtraction. Both approaches yield identical results. One may note that there is an asymmetrical broadening in the peaks. This makes additional, weak Gaussian peaks necessary for a satisfactory fit. However, for the analysis, only the main peak frequency was considered. As the broadening changed from experiment to experiment, the precision of the nitrile stretching frequency was, over all measurements, $\pm 0.3 \text{ cm}^{-1}$. As measured by Francisco Velazquez Escobar in our group using Raman spectroscopy (Schkolnik, Salewski, et al. 2012), non-covalently bound (solid) MBN displays a band at 2225.7 cm^{-1} , i.e. ca. 8 cm^{-1} lower than that of the covalently bound, buffer exposed label. Such a band is present in the protein spectra immediately after labeling, however it disappears upon purification of the labeled protein. It is therefore easy to check the spectra for protein purity after removing the unbound MBN from the solution using the post-labeling purification procedure (see section 3.3.2). We have also tried to label the variant K87C, but in this case a nitrile stretching peak was undetectable, and it was concluded that the labeling failed.

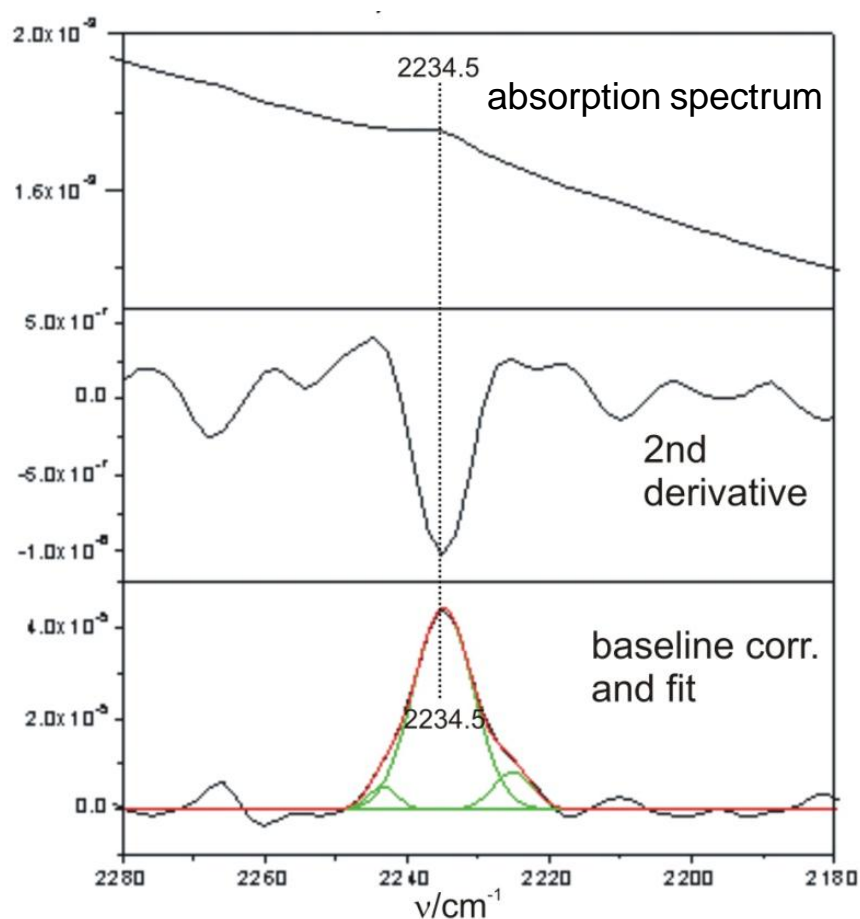
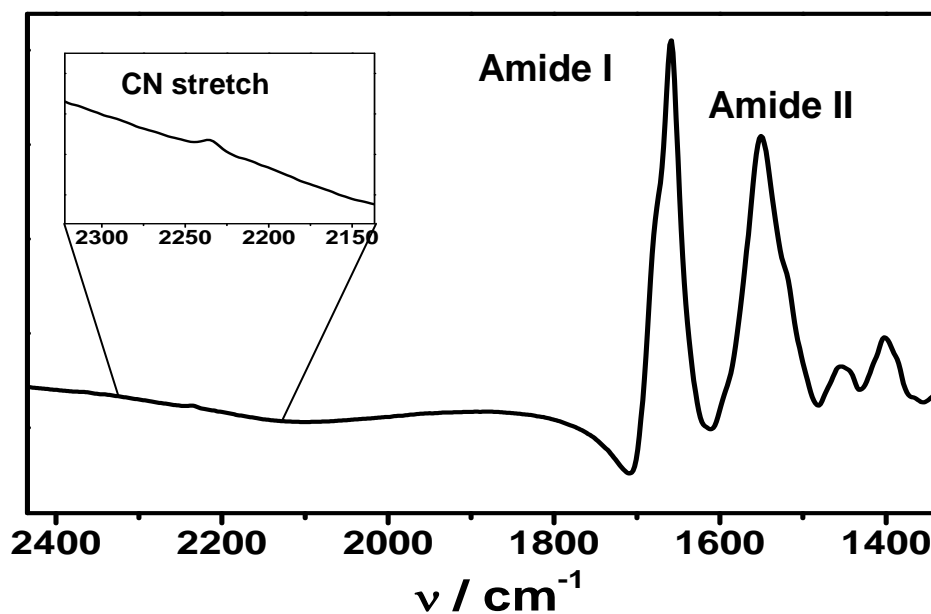


Figure 4.2.1 a) SEIRA spectrum of MBN-labeled K39C Cyt-c, with the Amine I and II bands at 1550 and 1658 cm^{-1} , respectively. Inset: Closer view of the CN stretch region, with the CN stretch of the protein-bound, water exposed MBN nitrile stretch at 2234.5 cm^{-1} . **b)** SEIRA spectrum of MBN-labelled K39C Cyt-c. Top: Absolute absorption spectrum of the CN stretch region. Middle: 2nd derivative spectrum of the same region. Bottom: Baseline subtracted, multi-Gaussian peak fitted absorption spectrum of the same region. In all spectra the CN stretch of the protein-bound, water exposed MBN nitrile stretch is seen at 2234.5 cm^{-1} .

4.2.1 Cyt-c-MBN in solution

For K39C-MBN in solution (Fig. 4.2.2 left, top), the CN stretching mode is observed at 2235.1 cm^{-1} . This frequency is significantly higher than that of solid MBN (2225.7 cm^{-1}) or MBN dissolved in DMSO [2228.3 cm^{-1} , (Schkolnik, Utesch, et al. 2012)], which indicates that the nitrile group is exposed to a protic environment, i.e. to the aqueous phase of the buffer the protein is dissolved in (Fafarman et al. 2010, Ghosh et al. 2009). This observation is in agreement with the results of molecular dynamics (MD) simulations which predicted that the nitrile group is solvent-exposed, see Fig. 4.2.4 (Schkolnik, Utesch, et al. 2012). For K8C-MBN in solution (Fig. 4.2.2 right, top), the CN stretching peak appears at 2234.5 cm^{-1} , in the same region as that measured for K39C, which also indicates that the nitrile group is solvent-exposed. Also in this case, MD simulations predict a solution exposed nitrile group [Fig 4.2.4 (Schkolnik, Utesch, et al. 2012)].

Apart from hydrogen bonding interactions, the stretching frequency of a protein-bound nitrile group is affected by the electric field arising from the charged and polar residues of the protein. In both mutants, K39C and K8C, the nitrile label is solvent exposed. Therefore one may assume that the hydrogen bonding interactions it is subject to are similar. Thus it is likely that the frequency difference $\Delta\nu_{K39C-K8C}$ of the bands at 2235.1 cm^{-1} (K39C) and 2234.5 cm^{-1} (K8C) arises mainly from the difference in the intrinsic electric field of the protein, projected along the MBN nitrile bond, $\Delta\vec{F}_{K39C-K8C}$. The component parallel to the nitrile bond it taken, because this is the direction of $\Delta\vec{\mu}$. Thus, one obtains:

$$(4.2.1) \quad \Delta\nu_{K39C-K8C} = \nu_{K39C} - \nu_{K8C} = -\Delta\vec{\mu} \cdot \Delta\vec{F}_{K39C-K8C}$$

where $\Delta\mu$ is the sensitivity of the nitrile stretching vibrational frequency to the presence of an external electric fields, also known as the Stark tuning rate. If for protein-bound and water-exposed MBN nitrile stretching the tuning rate is $\Delta\mu = -6.0 \cdot 10^{-9} \text{ cm}^{-1} / \text{V} \cdot \text{m}^{-1}$ (see 4.1), then according to Eq. 4.2.1, one obtains $\Delta F_{K39C-K8C} = 6.6 \cdot 10^7 \text{ V} / \text{m}$. This difference in the local electric field may be mainly related to the larger number of positively charged lysine residues in the vicinity of position 8.

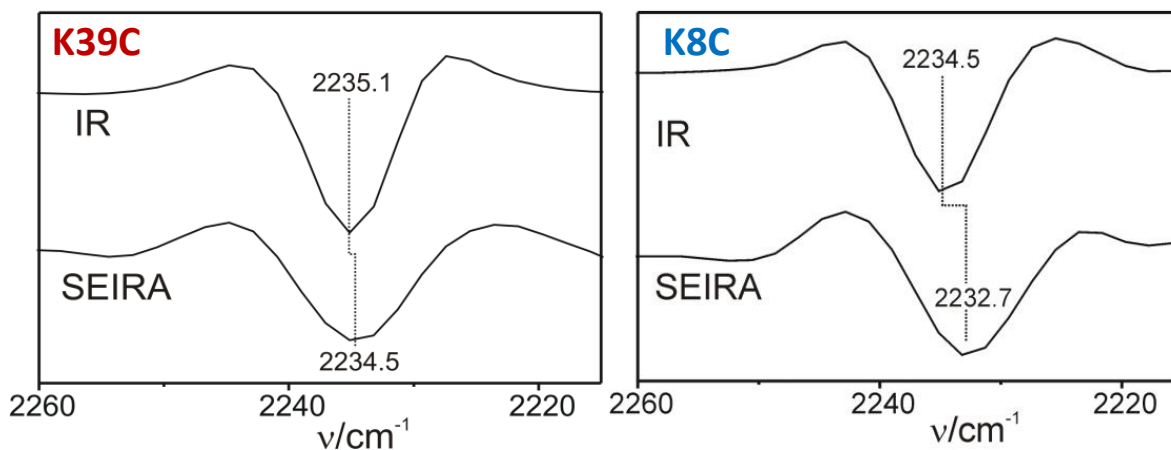


Figure 4.2.2 Second derivatives of the IR (top) and SEIRA (bottom; measured at open circuit) spectra of the MBN-labeled Cyt-c. **Left:** K39C; **Right:** K8C. The root-mean standard deviation was ± 0.15 (IR) and ± 0.9 cm^{-1} (SEIRA).

4.2.1 Cyt-c-MBN at SAM

In the next step, the labeled proteins were introduced into the SEIRA setup and thus immobilized on the 6-mercaptohexanoic acid (MHA) SAM-coated Au film. Cyt-c becomes immobilized to the SAM due to the electrostatic attraction of the negatively charged tail-groups to the positively charged lysine-rich binding domain surrounding the exposed heme crevice (see section 2.2.1) (Ly et al. 2011, Wisitruangsakul et al. 2008, Murgida and Hildebrandt 2005, Xu and Bowden 2006). To ensure that the native protein structure and function are preserved even after protein labeling and immobilization, cyclic voltammetry and SEIRA spectro-electrochemical redox titration (Wisitruangsakul et al. 2008) were performed. The redox potential determined by CV (Fig. 4.2.3 top) was 0.01 V, which, within the error margin, is the same as that measured for the wild-type protein (i.e. 0.04 V, Wisitruangsakul et al. 2008). The SEIRA redox titration difference spectra demonstrate the structural integrity of the immobilized variant proteins, although the redox potential derived from these spectra is 0.07 V, slightly more positive than the literature value (Wisitruangsakul et al. 2008) (Fig. 4.2.3 bottom).

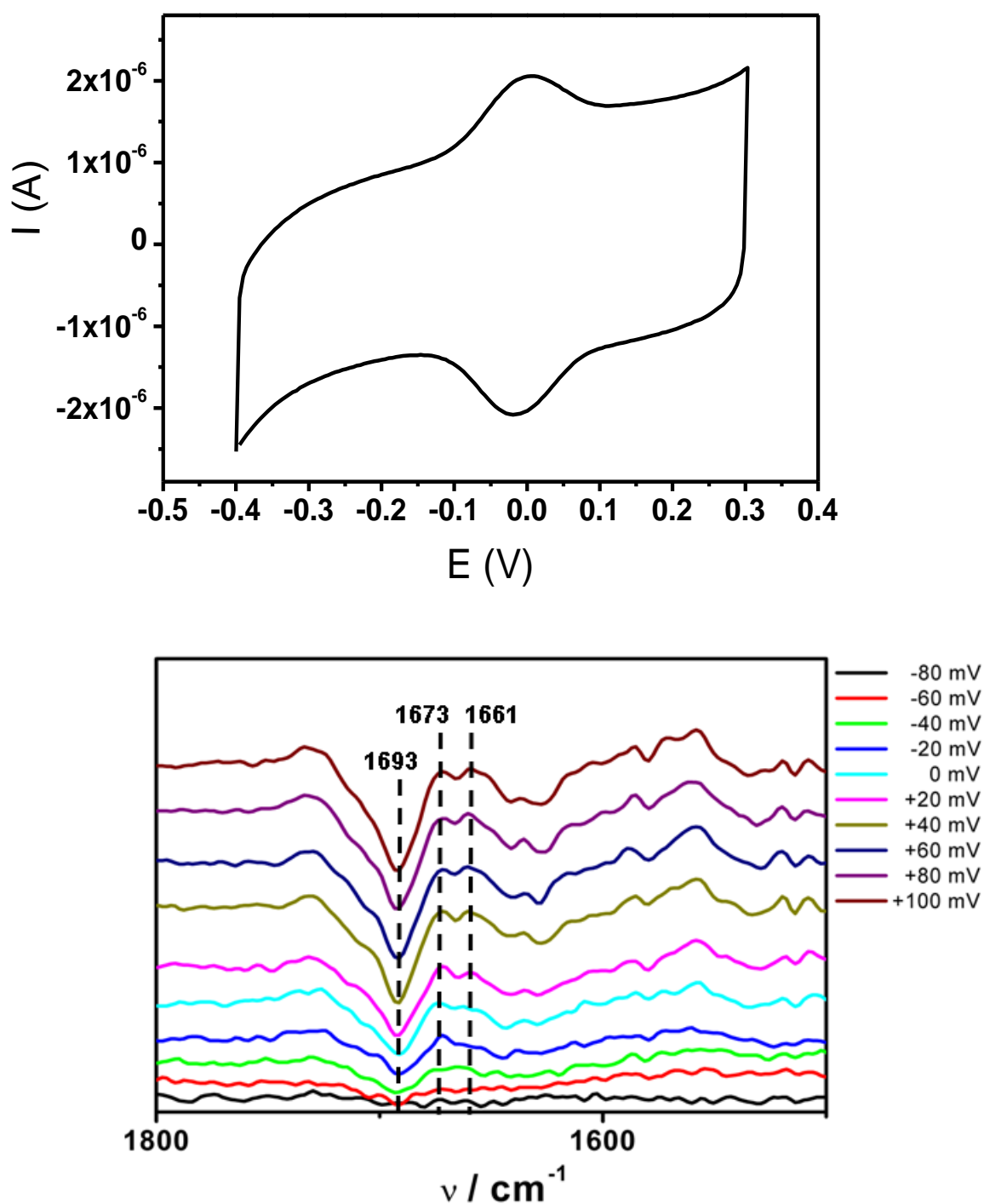


Figure 4.2.3 Cyclic voltammogram (**top**) and Redox titration difference spectra (**bottom**) of SAM-immobilized K39C-MBN in the SEIRA setup. Cyclic voltammogram scan rate 50 mV/sec, $E^0=0.01$ V vs Ag/AgCl. Redox titration: $E^0=0.08$ V vs Ag/AgCl, calculated by changes to the mode appearing at 1693 cm^{-1} .

The nitrile stretching frequency in the SEIRA spectrum of K39C-MBN, measured at open circuit, is 2234.5 cm^{-1} . This is slightly lower than for the labelled protein in solution (Fig. 4.2.2). In contrast, for the labelled K8C, the frequency measured for the probe bound to the SAM-immobilized protein is much lower, at 2232.7 cm^{-1} (Fig. 4.2.2).

MD simulations carried out for the MBN-labelled K39C and K8C immobilized on a SAM-coated Au surface (Schkolnik, Utesch, et al. 2012) show that the nitrile function remains solvent exposed in both Cyt-c variants (Fig 4.2.4). Furthermore, MD simulations show no indication of significant immobilization-induced changes to protein structure. It may also be noted that in the case of K8C the simulations rule out a direct interaction of the nitrile function with the SAM carboxyl groups, in spite of the proximity of the Stark label to the protein binding patch (Fig. 4.2.4). It is thus assumed that frequency changes to the nitrile stretching upon protein immobilization on the SAM result mostly from changes to the local electrostatic field caused by the potential drop across the electrode/SAM/solution interface.

It follows that from $\Delta\nu$, i.e. the *difference* between the nitrile stretching frequencies measured in the IR and SEIRA setups, one may extract the interface-induced electric field $\vec{F}(x)$ at a distance x from the SAM surface:

$$(4.2.2) \quad \Delta\nu = \nu_{SEIRA} - \nu_{IR} = |\Delta\vec{\mu}| \cdot |\vec{F}(x)| \cdot \cos(\alpha)$$

Here α is the angle between $\vec{F}(x)$ and $\Delta\vec{\mu}$, i.e. the angle between the nitrile bond dipole and the surface normal in the SEIRA configuration, to which the x component of the interface-induced electric field $\vec{F}(x)$ is parallel. Thus, the frequency differences $\Delta\nu$ of -0.6 cm^{-1} (K39C) and -1.8 cm^{-1} (K8C) yield $|\vec{F}(x)| \cdot \cos(\alpha) = -6.6 \cdot 10^7 \text{ V/m}$ and $-2.0 \cdot 10^8 \text{ V/m}$ for K39C and K8C, respectively.

To test the way these results relate to estimates of $\vec{F}(x)$ based on electrostatic models, one may assume, as a first approximation, an exponential distance-dependent decay of the electric field at the SAM-solution interface:

$$(4.2.3) \quad |\vec{F}(x)| = -E_{SAM} \cdot \kappa \cdot \exp(-\kappa \cdot x)$$

where E_{SAM} is the potential at the SAM surface, κ is the reciprocal Debye length and $x=0$ is at the SAM surface.

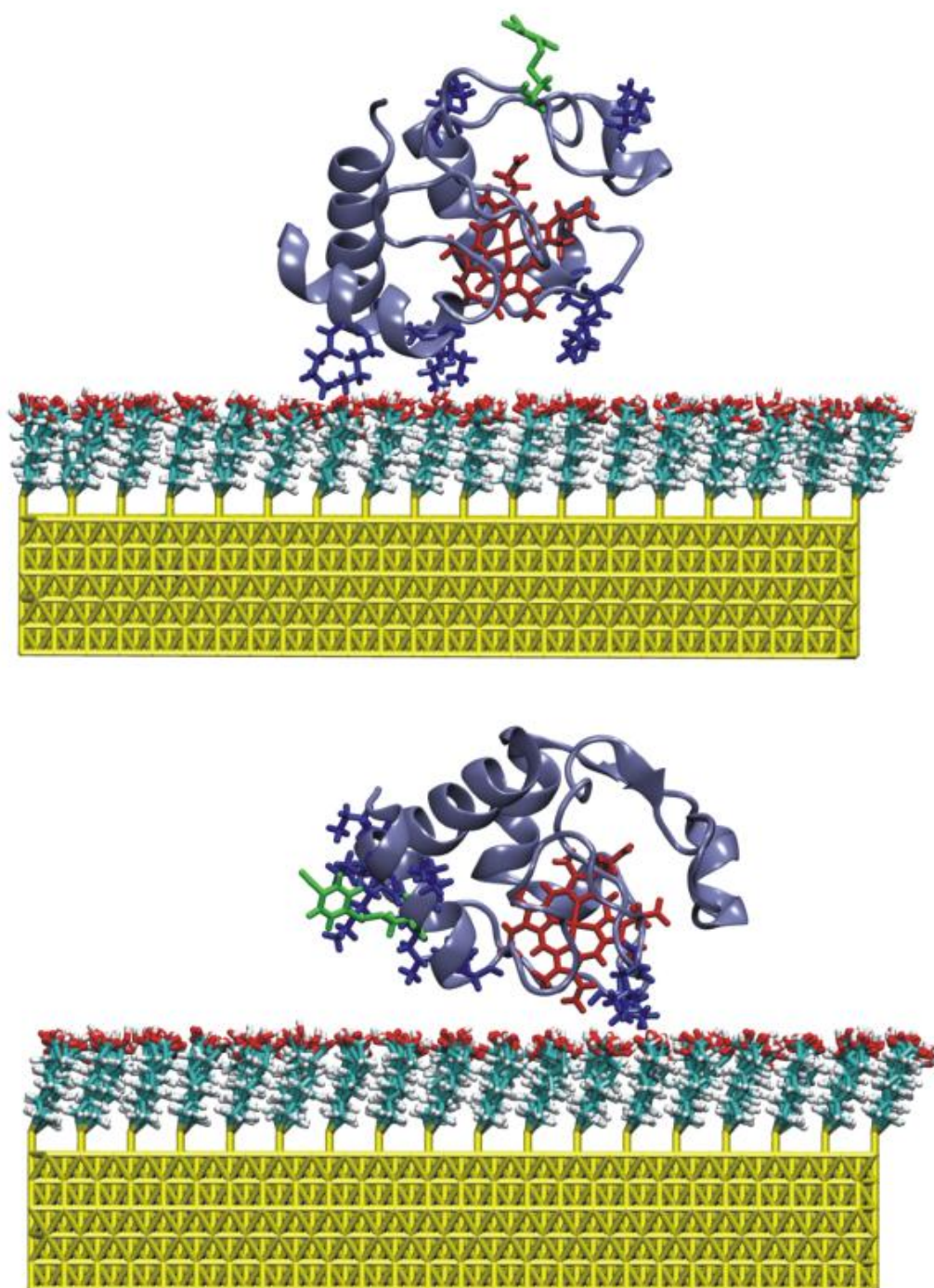


Figure 4.2.4. Snapshot of Cyt-c K39C-MBN (**top**) and K8C-MBN (**bottom**) bound to SAM-coated Au surface. The MBN group and the positively charged lysine surface residues in the vicinity of the label are shown in green and blue, respectively. From Schkolnik, Utesch et al. (2012).

From MD simulations the distance between the centre of the nitrile bond and the SAM surface, as well as the angle of the nitrile bond dipole with respect to the surface normal can be determined. When those parameters were averaged over the last 5 ns of a 10 ns production run, the following values were obtained: 4.4 nm and 127° for K39C, and 2.2 nm and 105° for K8C (Schkolnik, Utesch, et al. 2012). One may then substitute Eq. (4.2.3) into Eq. (4.2.2), and calculate the *ratio* of the frequency differences, i.e. $\Delta\nu_{K39C} / \Delta\nu_{K8C}$. Such a calculation is useful, as in this way the quantity E_{SAM} cancels out. As the measurements were performed at 10° C, in a 10 mM potassium phosphate buffer, pH 7.0 (ionic strength = 22 mM), the reciprocal Debye length κ is $5 \times 10^8 \text{ m}^{-1}$.

$|\vec{F}(x)|$ The value resulting from such a calculation is $\Delta\nu_{K39C} / \Delta\nu_{K8C} = 0.78$, significantly larger than the experimental ratio of 0.33. This means that the theoretical approach underestimates the decay of the local electric field with distance from the SAM surface. Such a discrepancy may arise from the assumptions made for Eq. (4.2.3). Firstly, spatially fixed charges in the diffuse double layer, arising from the immobilization of the protein as a polyelectrolyte at the SAM/solution interface are neglected. This is particularly important in the case of K8C-MBN, since in this variant the label is surrounded by several positively and negatively charged residues. Second, according to MD simulations, positively charged residues near the SAM surface reorient upon docking, due to their electrostatic attraction towards the negatively charged SAM head-groups, which may attenuate the interfacial electric field in the vicinity of the binding patch. This effect is likely to be less severe for the more remote label in K39C, both due to the longer distance from the SAM surface and to the lower number of nearby charged residues. However, for K8C-MBN, neglecting this effect in the calculation, may result in an overestimation of the local electric field at the label position. It therefore arises that a simplistic exponential dependence of $|\vec{F}(x)|$ on distance in the SAM/solution interface is insufficient for describing the local electric field profile in this case, where a label is exposed to both fixed and mobile charges at the diffuse double layer. Combining experimentally obtained values and MD-simulation predicted ones, by substituting $\alpha = 105^\circ$ in Eq. (4.2.2) for the label position of K8C, one obtains a value of $|\vec{F}(x)| = 9.4 \cdot 10^8 \text{ V/m}$ at 2.2 nm from the SAM surface. This result is in the order of magnitude of previous estimates (Murgida & Hildebrandt 2001).

4.3 The vibrational Stark effect of MBN as a tool for understanding the electrostatics of metal/SAM/solution interfaces

4.3.1 Formation of MBN-SAM on Au electrodes

Following the SAM formation procedure specified in section 3.2.4, Fig. 4.3.1 (top) shows the increase in nitrile stretching intensity that occurs when a typical MBN SAM is formed on Au. Upon addition of MBN dissolved in DMSO to the SEIRA cell, the nitrile stretching peak appeared at 2222.8 cm^{-1} . The increase in peak intensity was followed by SEIRA. In Fig. 4.3.1 (bottom) the time course of the peak intensity is shown. The peak intensity first grows rapidly and then reaches a plateau as the SAM becomes too tightly packed to admit any further MBN molecules at the surface. When the cell was washed with DMSO to remove excess MBN, the CN stretch reached a frequency of 2223.2 cm^{-1} .

To make sure that MBN has indeed formed a SAM on the gold surface, a cyclic voltammogram (CV) of the monolayer was recorded. Subsequently, after the completion of the potential series (see section 4.3.5), cyclic voltammetry (CV) was performed, with vertex potentials at -400 and 300 mV , and a scan rate of 50 mV/sec , followed by the acquisition of a SEIRA spectrum. Later a reductive potential of -1500 mV was applied for 5 min to reduce the Au-S bonds and so desorb the SAM. A SEIRA spectrum was again acquired and a second, identical CV performed. Then a final SEIRA spectrum was acquired. In Fig. 4.3.2 (top), the CV measured before applying the reductive potential shows the small capacitive current indicative of the presence of a SAM (Smith & White 1992), whereas after applying -1.5 V , the Au-S bond is reduced and the SAM is removed from the gold surface, leading to a sharp increase in the capacitive current, and yielding a CV similar to that obtained for the bare gold surface. In Fig. 4.3.2 (bottom) SEIRA spectra were recorded to follow the MBN nitrile stretch peak before, during and after applying the reductive potential. The nitrile stretching mode disappears from the spectra as the Au-S bond is reduced and the MBN SAM is desorbed from the surface.

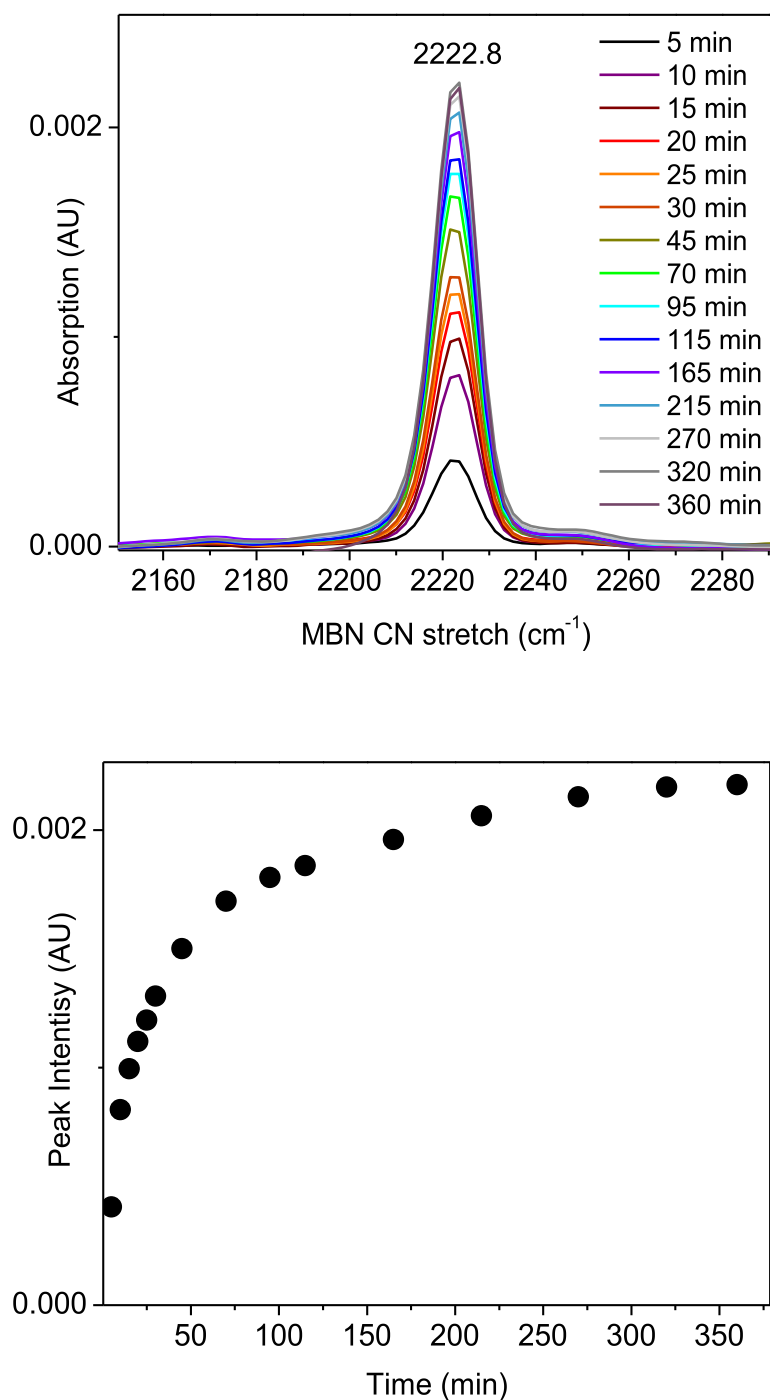


Figure 4.3.1. Time series of the nitrile stretching vibration originating from MBN monolayer formation on Au film in SEIRA setup. **Top:** SEIRA spectrum segment; **Bottom:** Peak intensity at 2222.8 cm⁻¹ as a function of time after addition of MBN to SEIRA cell.

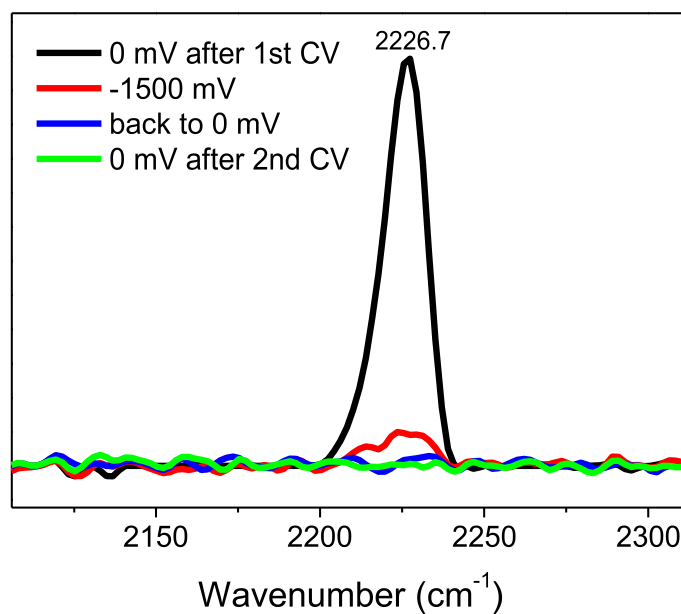
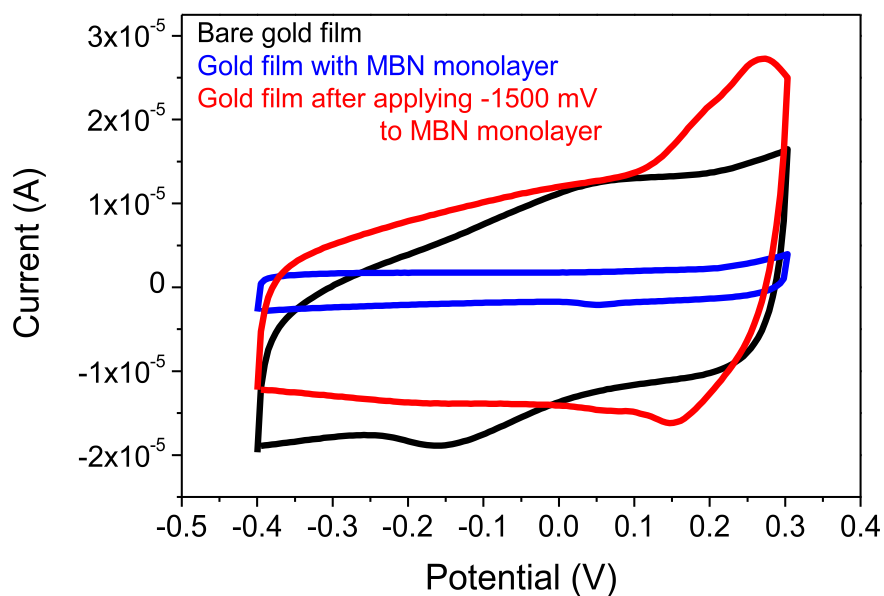


Figure 4.3.2. Top: Cyclic voltammograms measured in the SEIRA cell, of the bare gold film (black), of the MBN SAM coated gold film (blue), and of the gold film after applying a voltage of -1.5 V to the MBN SAM (red). **Bottom:** SEIRA spectra, showing the MBN peak before (black), during (red) and after (blue and green) applying -1.5 V to the gold film.

4.3.2 Thiophenol:MBN mixed SAM preparation

The SEIRA cell was filled with a 2mM solution of Thiophenol in DMSO:H₂O 3:1 (v/v) and allowed to incubate overnight. The next day, the cell was successively washed with DMSO:H₂O, H₂O and buffer (potassium phosphate, 10 mM, pH=7.0). A CV was recorded with vertex potentials at -400 and 300 mV, and at a scanning rate of 50 mV/sec, with the buffer serving as electrolyte, to ensure the formation of a SAM on the Au working electrode. Once that was established (data not shown), MBN was added to the cell, to a final concentration of 100 nM, while the potential on the Au working electrode was kept at 0 mV. The MBN nitrile stretching peak could be detected, and its growth was followed with time (see Fig. 4.3.3, top). The peak remained after removing excess unbound MBN from the cell and washing it, indicating that it represents MBN covalently bound to the gold surface. After the series of applied potentials (see section 4.3.6), a CV was recorded, to ensure that the monolayer was still attached to the gold electrode, followed by a reductive potential of -1.5 V to desorb the monolayer. Then another CV was performed, and SEIRA spectra were recorded at each step, to ascertain desorption of the monolayer from the surface (see Fig. 4.3.3, bottom). The results from both SEIRA and the cyclic voltammograms indicate that a mixed thiophenol:MBN SAM was indeed formed by integration of MBN molecules into the pre-existing thiophenol SAM, and that the MBN molecules were covalently bound to the Au surface.

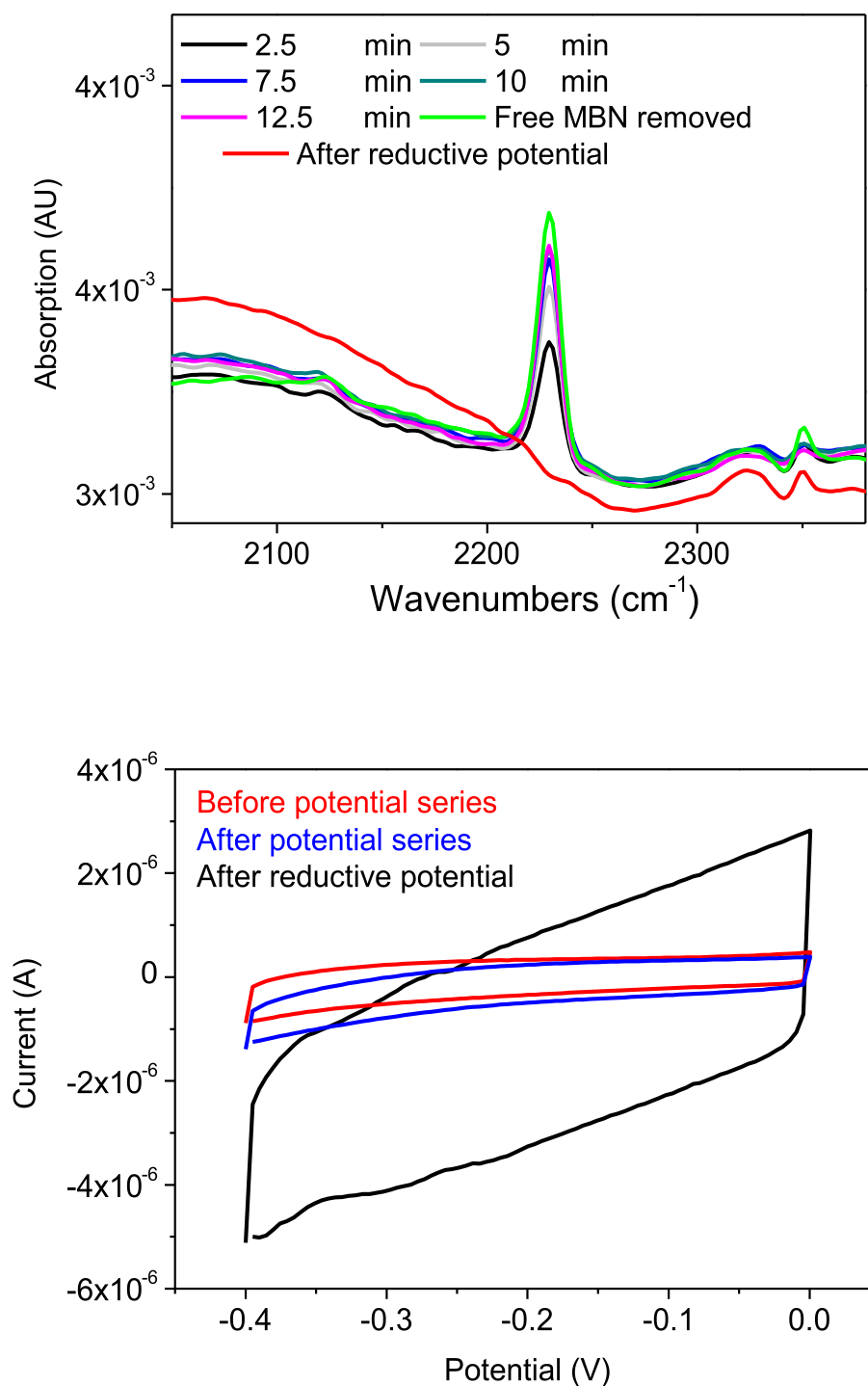


Figure 4.3.3. Top: SEIRA spectra, showing the nitrile stretching peak after MBN was added to a SEIRA cell containing a thiophenol monolayer (black, grey, blue, teal and pink spectra taken at 2.5 min intervals after MBN addition to cell), after removing the MBN solution from the cell (green) and after applying -1.5 V to the Au WE (red). **Bottom:** Cyclic voltammograms performed on the thiophenol:MBN mixed monolayer before (red) and after (blue) applying a potential series (see section 4.3.6), and after applying a reductive voltage of -1.5 V (black).

4.3.3 MHA:MBN mixed SAM preparation

To probe the behavior of the MBN nitrile stretching mode within an environment of charged residues, a SAM of 6-mercaptohexanoic acid (MHA) was formed on the Au working electrode, by incubating the cell overnight with a solution of 1mM MHA in ethanol overnight. After residual MHA and ethanol were removed from the cell, it was filled with buffer and MBN was added to the solution to a final concentration of 1 nM. To integrate MBN into a MHA monolayer, a mildly reductive potential of -0.4 V was applied, to remove a fraction of MHA molecules from the surface, allowing the binding of MBN molecules from the bulk solution to the vacant adsorption sites. The process was monitored by SEIRA spectroscopy. In Fig. 4.3.4, the decreasing carboxylate stretching modes band intensities of MHA and the increasing intensity of the MBN nitrile stretching and ring stretching modes indicate the desorption of MHA molecules and the adsorption of MBN molecules. After ca. 12 hours under -400 mV, the SEIRA intensity of the nitrile stretching reached a value of ca. 4% of that for the pure MBN monolayer at the same potential, reflecting the relative contribution of MBN to the composition of the mixed monolayer. This number may not be taken as an absolute MBN coverage rate, due to possible differences in SAM density between MBN and MHA pure SAMs.

4.3.4 Solvent effects on the nitrile stretching modes in an MBN-SAM on Ag and Au

The nitrile stretching frequency of pure MBN SAMs on Ag and Au electrodes was measured by SER and SEIRA spectroscopy, respectively (Schkolnik, Salewski, et al. 2012). In the absence of any solvent, i.e. when probing the SAM/air interface, the CN stretching frequency was determined to be 2230.0 ± 1.0 cm^{-1} for Ag/MBN and 2225.8 ± 0.2 cm^{-1} for Au/MBN (Figure 4.3.5). In the case of Ag/SAM, the frequency increased upon addition of DMSO and of different fractions of buffer in DMSO (from 0 to 100%), up to a value of 2235.1 ± 1.0 cm^{-1} at 100% aqueous buffer. For Au/SAM in contact with DMSO/buffer solutions, the CN stretching frequency first dropped considerably upon the addition of DMSO, and then decreased further upon the addition of the first two

10% buffer fractions. From 30% buffer on, it increased monotonically up to a value $2228.6 \pm 1.0 \text{ cm}^{-1}$ in 100% buffer solution. Interestingly, this value is essentially the same as that determined also for Au/MBN SAM in 100% water ($2228.4 \pm 1 \text{ cm}^{-1}$), indicating that at 10 mM a buffer is equivalent to pure water, in its effect on the nitrile stretching frequency of the MBN SAM (for a detailed discussion of these effects see section 4.3.7).

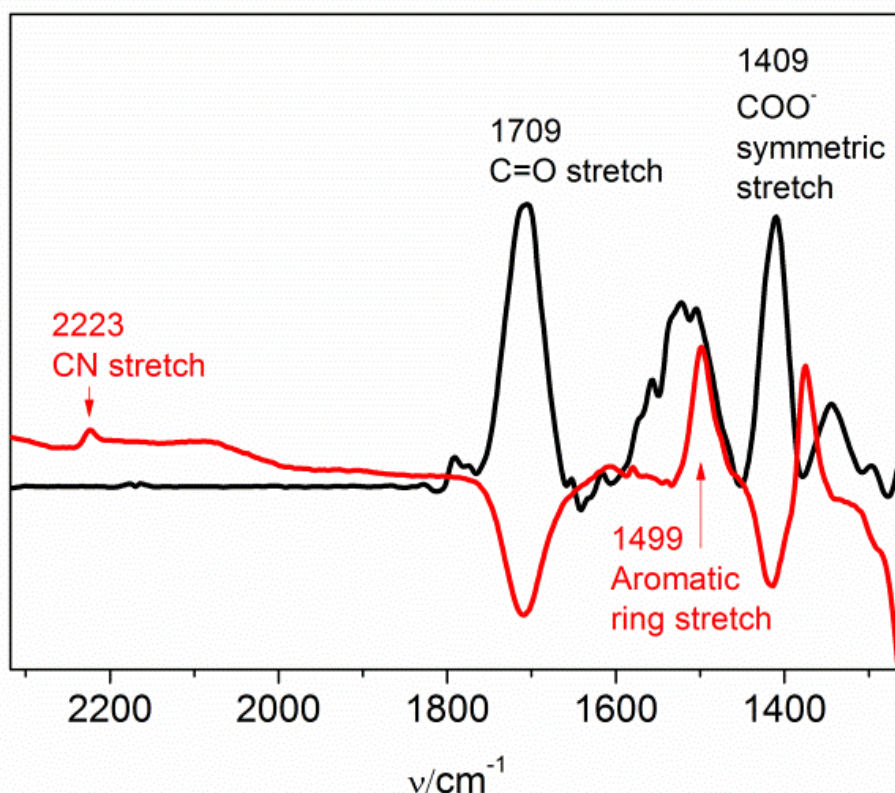


Figure 4.3.4. Black: SEIRA spectrum of MHA SAM on Au. Reference spectrum: bare Au film. **Red:** spectrum of the same SAM after addition of MBN to the spectro-electrochemical cell under -400 mV (vs. Ag/AgCl). Reference spectrum: Au film with MHA SAM. From the appearance of the nitrile stretching mode at 2223 cm^{-1} , along with the negative peaks at 1709 and 1409 cm^{-1} , it is evident that some of the MHA molecules are being replaced by MBN.

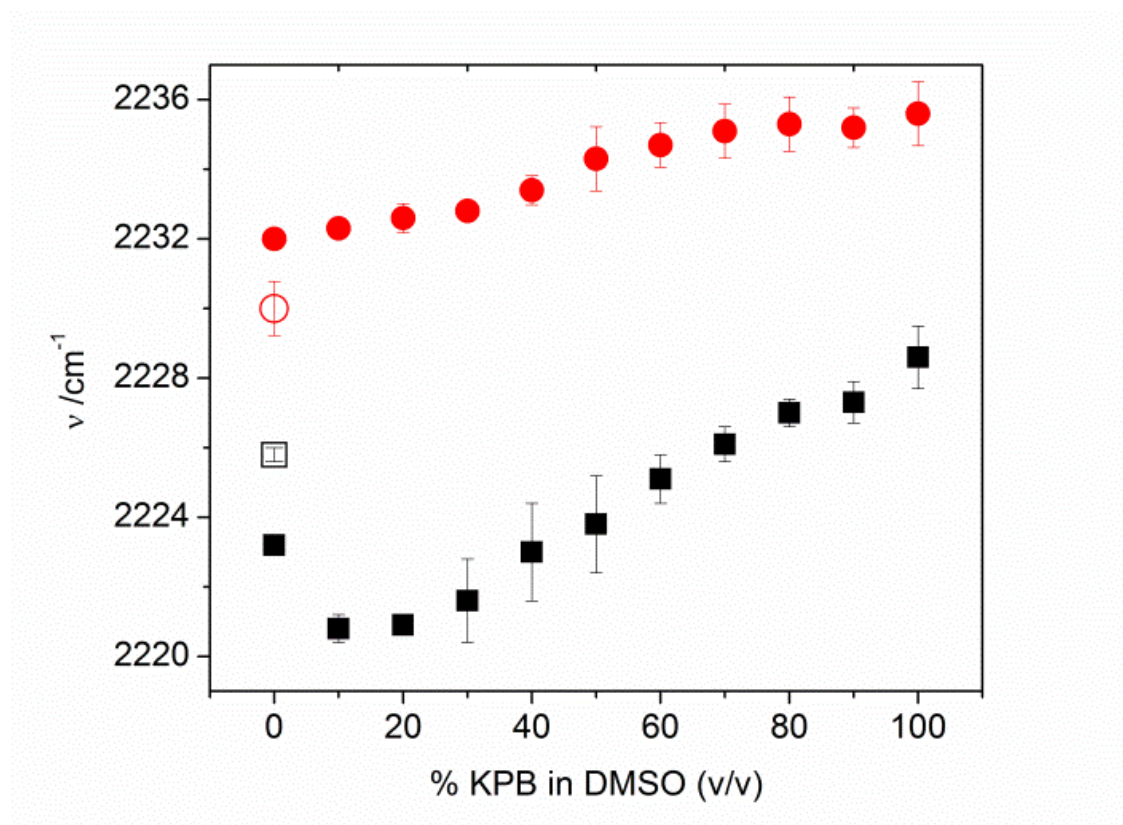


Figure 4.3.5. Nitrile stretching frequencies for MBN SAMs on Au (black) and Ag (red), measured by SEIRA and SERS, respectively, in different fractions of potassium phosphate buffer (KPB) 10mM pH=7.0 in DMSO (solid symbols). Hollow symbols: no solvent (Metal/MBN/air interface). The error bars indicate the root-mean square deviations over two measurements.

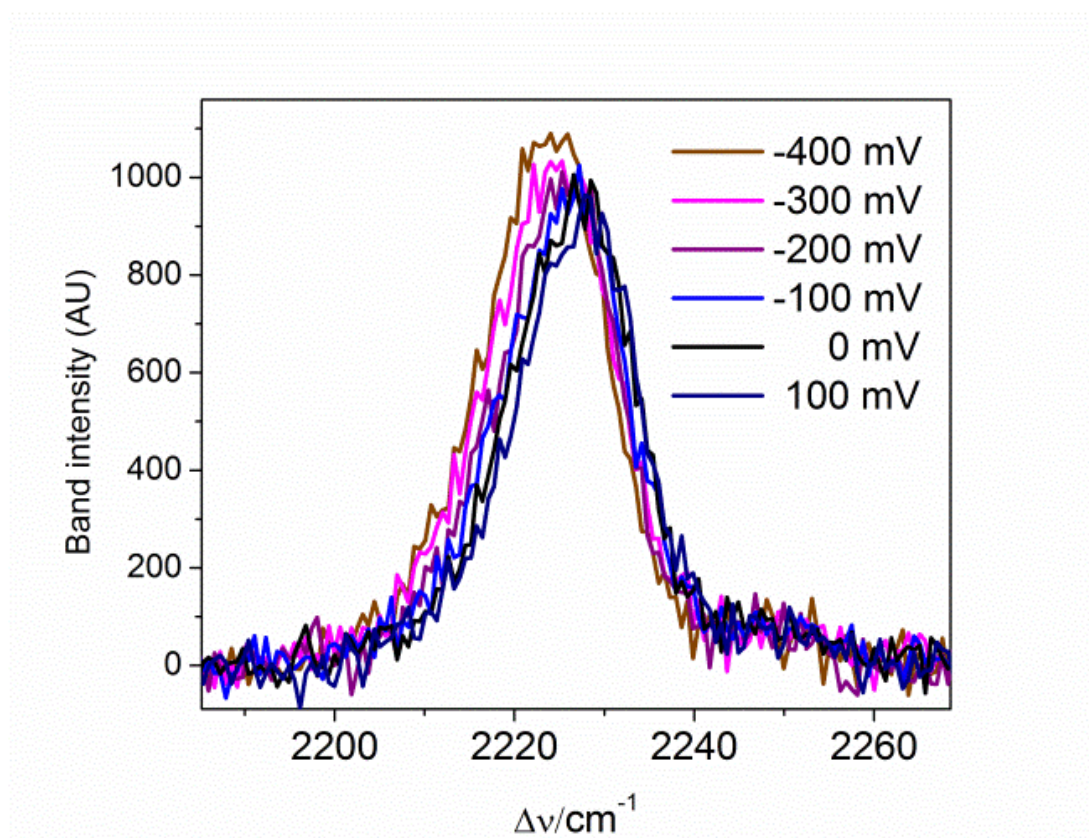
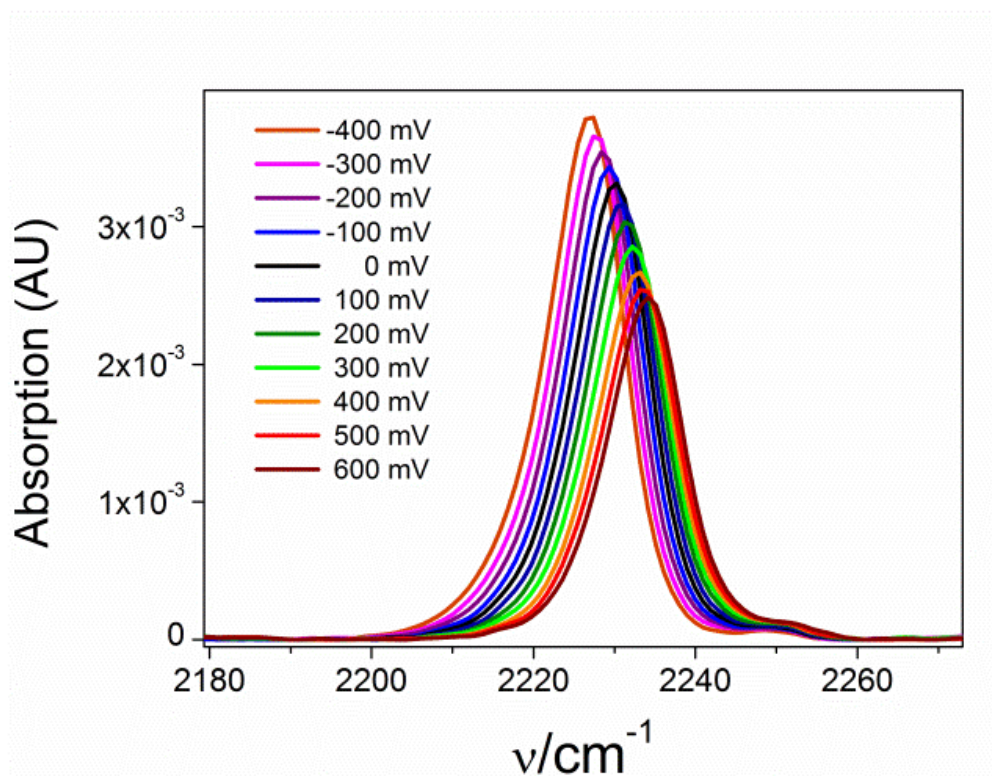
4.3.5 The nitrile stretching frequency in MBN-SAMs on Ag and Au under a series of applied potentials

The working electrode potential was varied from -0.4 to +0.6 V and from -0.5 to +0.1 V for Au/MBN-SAM and Ag/MBN-SAM, respectively, and changes to the MBN nitrile stretching mode were recorded. The potential limits were defined by the onset of metal oxidation and of the metal-sulfur bond reduction. Selected SEIRA and SER spectra are shown in Figure 4.3.6. The frequency linearly increases with increasing potential, both for the Au and the Ag electrode. The slope and intercept of the linear fits are similar for

the MBN SAMs on Au and Ag (Fig. 4.3.6 right). There is no indication of potential-dependent variations in the band profiles. However, in both cases, peak intensity decreases significantly as the potential becomes more positive (Fig. 4.3.7). This intensity dependence on the potential is reversible. It might be explained by electric-field induced reorientation of the dipolar MBN molecules while attached to the gold film. Since according to the surface selection rules, intensity is observed only for vibrational modes perpendicular to the surface, and since in ATR spectroscopy the signal strength is dependent on the vibrational mode's distance from the surface, the changes in the CN stretch intensity may arise from a change in the tilt angle θ between the CN bond and the surface normal, in combination with changes to the distance of the nitrile bond from the surface as the tilt angle varies.

4.3.6 The MBN nitrile stretching frequency in mixed SAMs on Au electrodes, under a series of applied potentials

Potential-dependent SEIRA measurements were carried out for the mixed thiophenol:MBN and MHA:MBN monolayers as well, to probe the nitrile stretching frequency of MBN as it protrudes into the solution, and within an environment dominated by protonated and deprotonated carboxylic head-groups, respectively. A behavior similar to that of a pure MBN SAM is seen (Fig. 4.3.6). In this case, however, the slope is lower than for the pure SAM, possibly indicating that in this system the nitrile groups are more exposed to the solvent, as they stick out into the solution above the aromatic ring plane, causing an increase in the Stark tuning rate due to stronger hydrogen bonding interactions (see section 2.6) (Oklejas & Harris 2003; Fafarman et al. 2012). For MHA/MBN, the frequency follows a linear relationship with the electrode potential similar to that of the pure MBN monolayer, albeit with a slightly different slope and intercept (Fig. 4.3.6). The larger slope, compared to Au/MBN, may imply that the nitrile groups are less exposed to the aqueous phase (Fafarman et al. 2012) and are instead partly buried within the SAM.



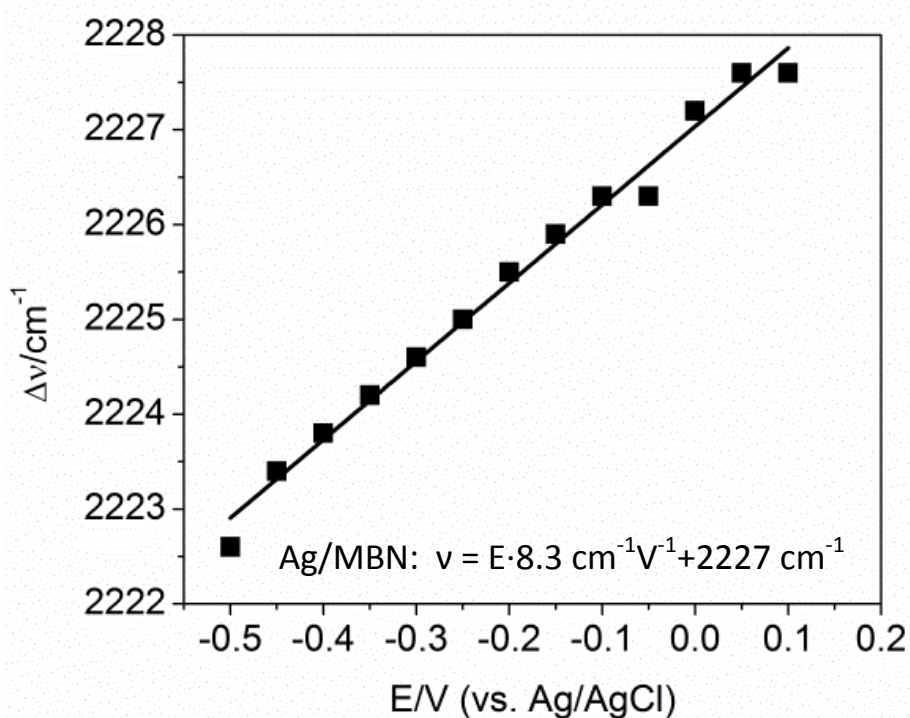
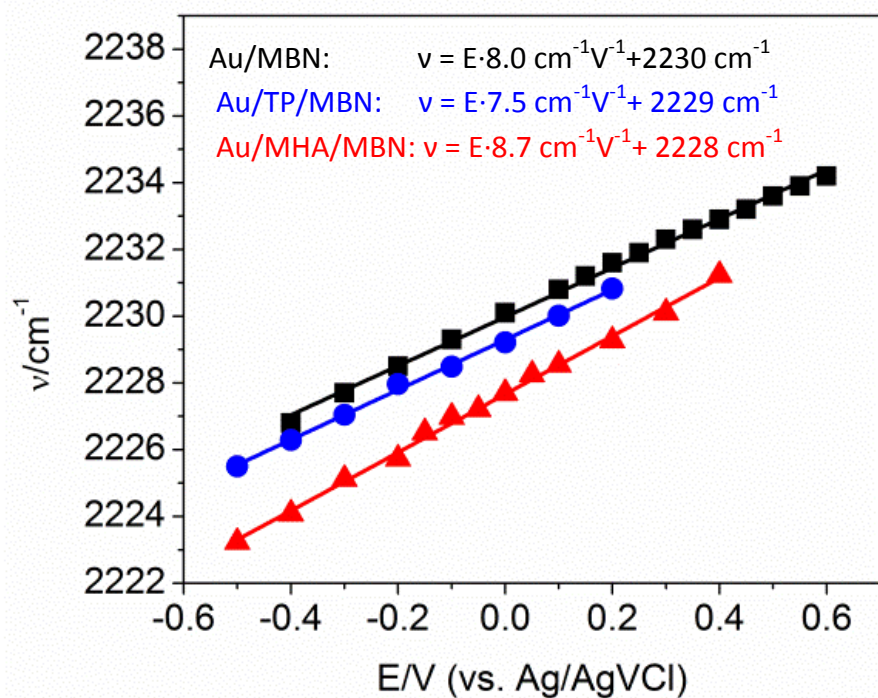


Figure 4.3.6 (double fold). **Top:** Au/SAM **Bottom:** Ag/SAM. **Left:** Nitrile stretch peak at different applied potentials (vs. Ag/AgCl) for the pure MBN SAM. **Right:** Nitrile stretching frequency vs. applied potential. The solid lines are linear fits to the data.

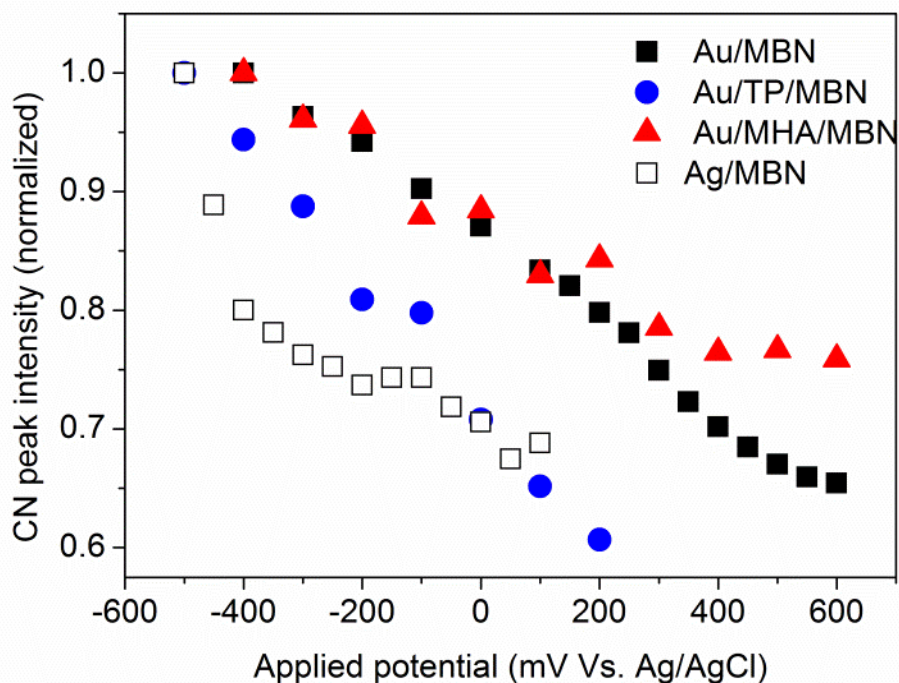


Figure 4.3.7. Changes in CN stretching band intensities with electrode potential for different compositions

4.3.7 Factors controlling the zero-field nitrile stretching frequency

The vibrational Stark effect (VSE) of MBN is defined as follows:

$$(4.3.1) \quad \nu = \nu_0 - \Delta\vec{\mu} \cdot \vec{E}_F$$

where $\Delta\mu$ is the difference dipole moment (between the ground and excited vibrational states), ν_0 is the vibrational frequency in the absence of an external electric field, and ν , the nitrile stretching frequency depends, linearly in our case, on the electric field E_F . The justification for our choice to neglect the quadratic term in the electric field dependence will be presented below. We use $\Delta\mu = 6.0 \cdot 10^{-9} \text{ cm}^{-1}/\text{V/m}$ for the present VSE analysis of the aqueous-phase exposed MBN SAM nitrile (see section 4.1). As opposed to the tuning rate, whose sensitivity to such different conditions seems to be relatively low, the value for the zero-field frequency ν_0 determined for free MBN in an

aqueous environment, as well as that determined for MBN in a frozen Me-THF glass cannot be used as an approximated value for that of MBN in a SAM, since packing, hydrogen bonding interactions, binding to different metals and the surface potential of the SAM all affect the nitrile stretching frequency quite significantly.

For the Au/MBN/air and Ag/MBN/air systems the nitrile stretching frequency is observed at 2225.8 and 2230.0 cm^{-1} , respectively. For comparison, the experimentally determined nitrile stretching frequency of benzonitrile in the gas phase is observed at 2238 cm^{-1} (Stein 2003). Thus, experimental data indicate a decrease in the nitrile stretching frequency upon metal binding and SAM formation. This red shift may arise from the depolarizing effect of the SAM (Natan et al. 2006), which may be similar to what occurs in solid MBN [2226 cm^{-1} (Schkolnik, Utesch, et al. 2012)]. It has been shown by Hamoudi et al. (2011) that charge is transferred in MBN attached to Au predominantly to the anti-bonding π_1^* orbital, which is perpendicular to the benzene ring. If this is indeed the case, then the fact that the red shift is smaller for Ag/MBN may be attributed to the larger charge density that is expected to flow from the metal to the MBN upon binding, as the work function of Ag is smaller (see section 4.3.8). This charge density transfer may serve to counteract depolarization due to packing, in the case of Ag but not in the case of Au, whose work function is higher.

Upon inserting the MBN-coated metal electrodes into a DMSO solution, the polar solvent molecules tend to orient in the SAM/solvent interface. The resulting surface potential causes a red-shift of 2.6 cm^{-1} in the nitrile stretching frequency in the case of Au (Fig. 4.3.5). Taking into account the potential-dependence of the nitrile stretching frequency (Fig. 4.3.6), a red-shift is equivalent to a negative shift in the electrode potential. Accordingly, we conclude that the DMSO molecules are preferentially aligned with their partial negative charges (i.e. their oxygen atoms) facing the SAM surface. Conversely, a 2- cm^{-1} blue-shift is observed in the case of Ag/MBN in contact with 100% DMSO, pointing to an opposite orientation of the DMSO molecules with respect to the SAM-coated Ag surface.

Similarly, the response of the nitrile stretching frequency to the increments in the fraction of aqueous buffer in the solvent mixture is different for Au/MBN and Ag/MBN. For Au/MBN, at small amounts of buffer the frequency decreases further. This may be

attributed to an orientation of the more polar water molecules in parallel to the DMSO molecules, both with their oxygen atoms pointing to the SAM, such that the surface potential becomes even more negative. However, with increasing buffer content, hydrogen bonding interactions of water molecules with the nitrile group become more dominant. Hydrogen bonding interactions have been shown to cause considerable blue-shifts in the nitrile stretching frequency of different nitriles (see section 2.6) (Aschaffenburg & Moog 2009; Ghosh et al. 2009; Fafarman et al. 2010; Levinson et al. 2012). After a short “tug of war” between the red-shift caused by the negative surface potential and the blue-shift due to hydrogen bonding interactions (20-30%, Fig. 4.3.5), the latter eventually dominates and thus leads to an increase in the frequency with increasing buffer content. In contrast, in the Ag-bound MBN SAM the nitrile stretching frequency increases monotonically, since in this case solvent molecule orientation (for both DMSO and H₂O) and hydrogen bonding both affect the nitrile stretching in the same direction. It is interesting to note that the nitrile stretching frequency of MBN in DMSO solution was recorded at 2227.7 cm⁻¹ and the corresponding value for an aqueous solution was estimated to be 2233.6 cm⁻¹ (section 4.1, Fig. 4.1.1). These values lie between the respective frequencies for the Au- and Ag-bound MBN SAM, which is in line with the observation that the SAM-coated metal surfaces are oppositely charged at open circuit.

On the basis of these results we may now estimate the MBN nitrile stretching frequency in the absence of electric field, ν_0 , for the Ag/SAM/buffer and Au/SAM/buffer systems. This frequency includes the effect of metal-sulfur bond formation and of the hydrogen bonding interactions between the nitrile and the aqueous phase, while excluding the effect of the surface potential at the SAM/solution interface arising from the charge on the metal electrode at open circuit. This value cannot be measured experimentally. However, we may assume that the effect of hydrogen bonding on the CN stretching frequency in an aqueous environment is independent of the existence of the metal-sulfur bond. Correspondingly, the blue-shift of 7.6 cm⁻¹ from solid MBN (2226 cm⁻¹) to MBN in aqueous solution (2233.6 cm⁻¹, section 4.1) should be approximately the same as for the hypothetical shift arising from transferring the Ag/MBN/air (2230.0 cm⁻¹) and Au/MBN/air (2225.8 cm⁻¹) systems into an aqueous solution while excluding the effect of electrode charge. Correspondingly, the addition of this increment to the frequencies

of the metal/MBN/air interfaces is estimated to provide a reasonable approximation for the frequencies in the absence of an electric field, and we thus obtain $\nu_0 = 2237.6 \text{ cm}^{-1}$ and $\nu_0 = 2233.4 \text{ cm}^{-1}$ for the MBN SAMs on Ag and Au, respectively.

4.3.8 Electrostatic model

Based on the Smith and White (1992) electrostatic model describing the interfacial potential distribution for SAM-coated metals and on further developments of the model (see section 2.1.3) (Lecomte et al. 2005; Murgida & Hildebrandt 2001), the electric field at the SAM/solution interface is given by

$$(4.3.2) \quad |E_F| = \frac{\varepsilon_S \kappa \varepsilon_0}{\varepsilon_0(\varepsilon_C + \varepsilon_S \kappa d_C)} (E - E_{pzc}) - \frac{\sigma_C}{\varepsilon_0(\varepsilon_C + \varepsilon_S \kappa d_C)}$$

where ε_C and ε_S are the dielectric constants of the SAM and the aqueous solution, respectively; d_C is the thickness of the MBN monolayer, ε_0 denotes the permittivity of vacuum, and κ is the reciprocal Debye length. In our system: $\varepsilon_S = 78$, $\kappa = 5 \cdot 10^8 \text{ m}^{-1}$ (for potassium phosphate buffer 10 mM, pH=7.0), $\varepsilon_0 = 8.854 \cdot 10^{-12} \text{ C} \cdot \text{V}^{-1} \cdot \text{m}^{-1}$, $\varepsilon_C = 3$ (Natan et al. 2010), $\Delta\mu = 6.0 \cdot 10^{-9} \text{ cm}^{-1} \cdot \text{V}^{-1} \cdot \text{m}$ (see section 4.3.7), and $d_C = 6.8 \cdot 10^{-10} \text{ m}$ for Au/MBN and $8.9 \cdot 10^{-10} \text{ m}$ for Ag/MBN (see discussion concerning tilt angles below). σ_C is the charge density on the SAM surface, which in the case of carboxyl-terminated SAMs has been related to the apparent pK_a of the head groups. In a more general sense, σ_C may be seen as the charge density in the inner Helmholtz layer reflecting the contributions of charged SAM head groups as well as those of the ions and water dipoles aligned in the immediate vicinity of the SAM surface. This surface charge density, originally assumed to be constant, varies with the electrode potential E , or more precisely, with the difference between the electrode potential E and the potential of zero charge of the metal E_{pzc} . Here, we assume a linear relationship as a first approximation:

$$(4.3.3) \quad \sigma_C = \sigma_0 + k(E - E_{pzc})$$

where k is a constant and σ_0 is the charge density at E_{pzc} . Eq. 4.3.2 may be combined with Eq. 4.3.3 to yield:

$$(4.3.4) \quad |E_F| = \frac{\varepsilon_S \kappa \varepsilon_0}{\varepsilon_0(\varepsilon_C + \varepsilon_S \kappa d_C)} (E - E_{pzc}) - \frac{\sigma_0}{\varepsilon_0(\varepsilon_C + \varepsilon_S \kappa d_C)} - \frac{k(E - E_{pzc})}{\varepsilon_0(\varepsilon_C + \varepsilon_S \kappa d_C)}$$

or after rearrangement:

$$(4.3.5) \quad |E_F| = \frac{\varepsilon_S \kappa \varepsilon_0 - k}{\varepsilon_0(\varepsilon_C + \varepsilon_S \kappa d_C)} (E - E_{pzc}) - \frac{\sigma_0}{\varepsilon_0(\varepsilon_C + \varepsilon_S \kappa d_C)}$$

For the electric-field dependence of the nitrile stretching frequency, we have to take into account the definition of the nitrile dipole axis pointing from the carbon to the nitrogen such that $\Delta\mu$ has a negative sign (Boxer 2009). Thus combining Eq. 4.3.5 and Eq. 4.3.1 yields:

$$(4.3.6) \quad \nu = \nu_0 + |\Delta\vec{\mu}| |\vec{E}_F| \cos\theta = \nu_0 + |\Delta\vec{\mu}| \cos\theta \left(\frac{\varepsilon_S \kappa \varepsilon_0 - k}{\varepsilon_0(\varepsilon_C + \varepsilon_S \kappa d_C)} (E - E_{pzc}) - \frac{\sigma_0}{\varepsilon_0(\varepsilon_C + \varepsilon_S \kappa d_C)} \right)$$

where θ refers to angle formed by the vector of the nitrile dipole moment and that of the electric field. Rearranging Eq. 4.3.6 leads to:

$$(4.3.7) \quad \nu = \nu_0 - |\Delta\vec{\mu}| \cos\theta \left(\frac{(\varepsilon_S \kappa \varepsilon_0 - k) E_{pzc} + \sigma_0}{\varepsilon_0(\varepsilon_C + \varepsilon_S \kappa d_C)} \right) + |\Delta\vec{\mu}| \cos\theta \left(\frac{\varepsilon_S \kappa \varepsilon_0 - k}{\varepsilon_0(\varepsilon_C + \varepsilon_S \kappa d_C)} \right) E$$

where the first two terms on the right hand side of Eq. 4.3.7 describe the intercept of the linear fits in Figure 4.3.6, whereas the last term corresponds to the slope. Note that Eq. 4.3.7 describes a linear relationship between the nitrile stretching frequency and the applied electric potential, via the linear relationship between the latter and the electric field. This, in combination with the excellent linear correlation empirically observed between the nitrile stretching frequency and the applied potential, E , (Fig. 4.3.6), justifies neglecting higher order terms in the analysis of the VSE (cf. Eq. 4.3.1).

From the slope term in Eq. 4.3.7 one may determine the quantity k for the various metal/SAM set-ups (Table 4.3.1). However, in order to do so, estimates for the tilt angle of the nitrile group relative to the metal surface normal are required. For *p*-cyanobiphenylthiol on Au, θ was determined to be $\sim 40^\circ$ (Ballav et al. 2007), which is similar to that determined for thiophenol SAM on Au ($49^\circ - 54^\circ$) (Frey et al. 2001; Kaefer et al. 2007). However, the angles for MBN compared to thiophenol on Ag differ significantly, with $24^\circ - 28^\circ$ reported for thiophenol on Ag (Han et al. 2001; Schalnath & Pemberton 2010), and, rather surprisingly, ca. 0° for MBN on Ag (Shaw et al. 2009). In view of this striking discrepancy between thiophenol and MBN on Ag, which is contrary

to the findings for Au, one has to consider the reported value for Ag/MBN with caution. Nevertheless, for the present calculations we first adopt 49° and 0° for Au/MBN and Ag/MBN, respectively. These values constitute a factor in determining the SAM thickness, d_c , for which an Ag-S bond length of 2.4 Å and Au-S bond length of 1.9 Å (Akinaga et al. 2001; Ehler et al. 1997), a sulfur-nitrogen distance of 6.5 Å as well as the respective values of θ discussed above were employed. As a result, d_c is evaluated to be 6.8×10^{-10} m and 8.9×10^{-10} m for Au/MBN and Ag/MBN, respectively.

Now we consider the intercept and determine the potential at which the electric field at the position of the nitrile group is zero. This potential may be considered as the effective potential of zero-charge E_0 for the SAM-modified metal, corresponding to the potential at which the experimentally determined frequency ν is equal to ν_0 (i.e. $\nu = \nu_0$ when $E = E_0$). Note that E_0 may differ substantially from E_{pzc} , which refers to the potential of zero-charge of the bare metal. We further use the E_0 values obtained in this way (Table 4.3.1) to calculate the charge densities in the inner Helmholtz layer at zero-field (σ_0) according to:

$$(4.3.8) \quad (E_0 - E_{pzc})(\epsilon_S \kappa \epsilon_0 - k) = \sigma_0$$

which is derived from Eq. 4.3.7 by substituting $E = E_0$ and $\nu = \nu_0$.

Eq. 4.3.5 may now be used to calculate the variation of the electric field strength at the SAM surface, i.e. at the position of the nitrile group, as a function of the electrode potential (Figure 4.3.8). For all metal/SAM set-ups, the electric field increases as the potential becomes more negative, covering a range from $0.9 \cdot 10^8$ V/m to $-2.5 \cdot 10^9$ V/m. Whereas similar values are obtained for Au/MBN and Au/thiophenol/MBN, the absolute value of the field strength is larger in the mixed MHA/MBN SAM on Au. As estimated from the nitrile SEIRA signal intensity, this mixed SAM includes roughly only 4% MBN. However, the question remains whether the incorporation of MBN into the preformed MHA SAM leads to a largely homogeneous MBN distribution or to MBN islands within the MHA SAM. In the latter case, one would expect an inhomogeneity of the SEIRA bands, given that there would be a different electric field strength at the rim of each island, dominated by the surrounding MHA SAM, than the one at the center of the MBN islands, leading to different nitrile stretching frequencies in the interior of the MBN islands compared to the MBN/MHA boundary. Such inhomogeneities are not

observed in the SEIRA spectra of Au/MHA/MBN, implying that the electric field at the SAM surface either does not display significant gradients parallel to the metal surface, or that the distribution of MBN within the MHA SAM is largely homogeneous. If the latter is true, then it may be concluded that (i) MBN probes the electric field on the MHA SAM surface, and (ii) the magnitude of the electric field on a MHA SAM on Au at pH 7.0 is only larger by ca. 15% compared to Au/MBN, despite the expected partial dissociation of the carboxylate head-groups at pH 7.0, especially at the higher applied potentials (White et al. 1998; Murgida & Hildebrandt 2001; Gershevitz & Sukenik 2004). For comparison, the field estimated for MHA SAM with immobilized Cyt-c, at 2.2 nm from the SAM surface is $-9.4 \cdot 10^8$ V/m at open circuit (see section 4.2). Since in the preparation of the Au/MHA/MBN SAM a potential of 400 mV was applied, it is impossible at the moment to supply open circuit values for the system presented in this section. However, as seen in Fig. 4.3.8, the value obtained in section 4.2 is within the range of electric fields experienced by the MBN nitrile in the Au/MHA/MBN system.

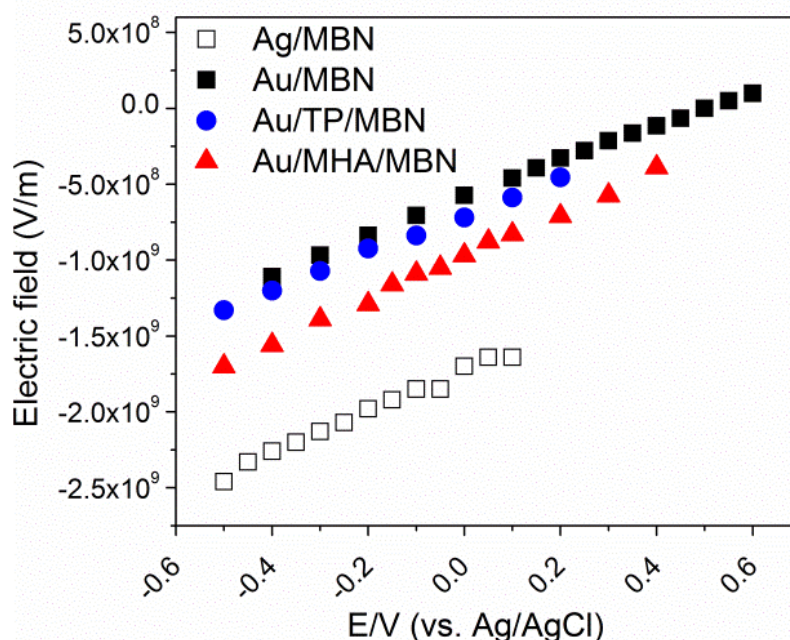


Figure 4.3.8. Plots of the electric field strength as a function of the electrode potential, calculated according to Eqs. 4.3.1 and 4.3.5, using the experimentally determined nitrile stretching frequencies for the four systems.

4.3.9 The effective potential of zero charge.

The quantity E_0 derived from the experiments reflects the change in the potential of zero charge of the pure metal (E_{pzc}) due to the modification of its surface by a dipolar SAM. The effective potential of zero charge E_0 can also be estimated by calculating the change in the work function of the metal ($\Delta\Phi$) arising from its modification by the SAM. Wang et al. (Wang et al. 2009) have made the observation that the only parameters affecting $\Delta\Phi$ in the case of metal modification by a dipolar SAM of certain head- and tail-groups, are the direction of the dipole moment of the SAM and its angle with respect to the surface normal (β), which can be derived from the molecular tilt angle θ for the SAM and from the angle of the dipole within the molecule. As mentioned previously, we have adopted 49° and 0° for Au/MBN and Ag/MBN, respectively, for the time being (see section 4.3.8). On the basis of the relationship between $\Delta\Phi$ and $\cos(\beta)$ determined by Wang et al. (2009), one then obtains $\Delta\Phi = 0.15$ and 2.6 eV for Au/MBN and Ag/MBN respectively.

For bare metals, the work function Φ_M is related to the potential of zero charge according to

$$(4.3.9) \quad E_{pzc} = \Phi_M - K$$

where here E_{pzc} is expressed in V vs. NHE and K is a constant that was determined to be 5.01 and 4.61 eV for Ag and Au, respectively (Trasatti 1971; Emets & Damaskin 2009 and references therein). Recommended values for the work function of bare polycrystalline Ag and Au are 4.3 and 4.88 eV, respectively (Valette 1982; Trasatti 1984), yielding -0.71 V and $+0.27$ V vs. NHE for E_{pzc} of polycrystalline Ag and Au, respectively. Correspondingly, Eq. 4.3.9 allows evaluating the effective potential of zero charge by substituting the modified work function of the SAM-coated metals $\Phi_{M/SAM}$ according to

$$(4.3.10) \quad E_0 = \Phi_{M/SAM} - K = \Phi_M + \Delta\Phi - K$$

providing, after conversion of the reference potential scale from NHE to Ag/AgCl, $E_0 = 0.215$ and 1.658 V for Au/MBN and Ag/MBN, respectively. These values are in reasonable agreement with the experimental data derived from the VSE analysis (0.450

and 1.277 V vs. Ag/AgCl, respectively, see Table 4.3.1), especially in view of the underlying approximations of both the electrostatic model and the E_0 calculations, and the simplistic approach used for the latter.

Another, more elaborate method for calculating $\Delta\Phi$ was suggested by Heimel et al. (2007, 2008). This includes the metal-sulfur bond dipole, BD , and the potential difference across the dipolar SAM, ΔV_{vac} , according to:

$$(4.3.11) \quad \Delta\Phi = \Delta V_{vac} + BD$$

where ΔV_{vac} is given by:

$$(4.3.12) \quad \Delta V_{vac} = -\frac{\mu_{\perp}}{\epsilon_0 A}$$

and μ_{\perp} is the dipole moment component of the SAM in the direction of the surface normal and A is the area of the unit cell (Heimel et al. 2007). Estimating μ_{\perp} for the SAM, even if β is known, cannot be accomplished by merely projecting the dipole of a single molecule of MBN onto the surface normal, as depolarization effects of the MBN dipole by neighboring molecules in the SAM exist (Natan et al. 2006). According to the findings of Natan et al. (2006), we adopt a value of 3.6 Debye for the dipole moment of the MBN SAM, which is then multiplied by $\cos(\beta)$ to yield μ_{\perp} . Based on the values calculated for a series of related systems (Heimel et al. 2007), BD is taken to be -1.05 eV and -0.27 eV for Au-MBN and Ag-MBN, respectively. The difference between these two values is in good agreement with experimental data reported by Alloway et al. (2009). Thus, one obtains $\Delta\Phi = 0.3$ eV (Au/MBN) and 2.9 eV (Ag/MBN), leading eventually to $E_0 = 0.402$ and 1.936 V vs. Ag/AgCl for Au/MBN and Ag/MBN, respectively. Here, E_0 for Au/MBN is much closer to the experimentally derived value (0.450 mV vs. Ag/AgCl, see table 4.3.1) than the result obtained using the other, more simplistic approach. However, for Ag/MBN this more elaborate calculation results in a stronger deviation from the observed E_0 . The failure to reproduce the experimental value for Ag/MBN in a satisfactory manner does not necessary argue against the approach proposed by Heimel et al. (2007). In view of the very good agreement for Au/MBN, one may also question the parameter that introduces the greatest uncertainty into the calculation in the case of the Ag/MBN system, i.e. the tilt angle of the nitrile function (θ) and as a result the angle of the dipole moment of the entire molecule with respect to the surface normal (β). One may,

therefore, use an approach suggested by Ballav et al. (2007) to estimate the angles β and θ from the measured change to the work function. We therefore take the experimental $E_0 = 1.277$ V, corresponding to $\Delta\Phi = 2.2$ eV, to derive $\beta = 38^\circ$, which yields a tilt angle (θ) of 26° . This value is in good agreement with those reported for thiophenol on Ag (Han et al. 2001; Schalnath & Pemberton 2010), which seems to be more reasonable, as it echoes the resemblance in (θ) for different S-phenyl containing SAMs on Au (Frey et al. 2001; Kaefer et al. 2007; Ballav et al. 2007).

In both cases, it should be noted that previous experimental and theoretical studies on SAM structures, and specifically on the tilt angle of the SAM molecules, refer to the metal/SAM set-up in air or *in vacuo*. Contact with an aqueous solution or an electrochemical environment may cause structural differences which are not considered. Moreover, the present analysis tacitly assumes that the tilt angle of the nitrile function is potential-independent. However, the variation in the SEIRA peak intensities in Figure 4.3.7 allows estimating the error inherent to this assumption. In the ATR SEIRA set-up, the IR signals are enhanced via the electric field component of the electromagnetic radiation perpendicular to the surface, $|E|_{\perp}$, such that a maximal enhancement is obtained for molecular oscillators oriented in parallel to the surface normal. Since the SEIRA intensity I_{SEIRA} scales with the square of $|E|_{\perp}$, it follows that $I_{SEIRA} \propto (\cos\theta)^2$. Assuming that the SEIRA intensity for a pure MBN SAM on an Au electrode, measured at an electrode potential of +0.4 V (close to E_0) would refer to a tilt angle of the nitrile function with respect to the surface normal of 49° , then the increased intensity at -0.4 V would correspond to a tilt angle of 38° .

Table 4.3.1. Electrostatic parameters for various metal/MBN interfaces ^a.

	Slope ^b (cm ⁻¹ /V)	Intercept ^b (cm ⁻¹)	k ^c (CV ⁻¹ m ⁻²)	E_0 , exp. ^c (V)	σ_0 ^c (Cm ⁻²)	E_0 , calc. ^d (V)	E_0 , calc. ^e (V)
Ag/MBN	8.3	2227	-0.117	1.277	1.005	1.685	1.936
Au/MBN	8.0	2230	-0.186	0.425	0.199	0.215	0.402
Au/TP/MBN	7.5	2229	-0.153	0.587	0.267	-	-
Au/MHA/MBN	8.7	2228	-0.232	0.621	0.330	-	-

^a Calculated according to Equation (4.3.7), using $\epsilon_S = 78$, $\kappa = 5 \cdot 10^8$ m⁻¹, $\epsilon_0 = 8.854 \times 10^{-12}$ C·V⁻¹·m⁻¹, $\epsilon_c = 3$ (Natan et al. 2010), $\Delta\mu = 6.0 \times 10^{-9}$ cm⁻¹·V⁻¹·m, and $d_c = 6.8 \times 10^{-10}$ m for Au/MBN and 8.9×10^{-10} m for Ag/MBN as described in the text. For E_{pzc} , we have used -0.92 V and +0.06 V for polycrystalline Ag and Au, respectively (Trasatti 1984; Valette 1982); ^b Taken from the linear fits in Figure 4.3.6; ^c As defined by Equation (4.3.3), derived from the experimental data according to Equations (4.3.7) and (4.3.8); ^d Calculated using Equation (4.3.10), according to Wang *et al.* (2009); ^e Calculated using Equations (4.3.10-4.3.12), according to Heimel *et al.* (2007);

4.4 Catalytic efficiency of Dehaloperoxidase A is controlled by electrostatics – the vibrational Stark effect as a tool for understanding enzyme kinetics

In this study dehaloperoxidase A (DHP A) variants were labeled with the VSE probe molecule MBN and the vibrational frequency of the MBN nitrile stretch was measured for each variant. The studied variants include the wild type (WT) protein and mutants consisting of substitutions that alter the total charge of the protein by up to one unit of charge. For the procedure of mutant production, see Zhao et al. (2012). The mutant variants are: R33Q, K36A (positive to neutral), N91K (neutral to positive), N61D and N96D (neutral to negative). All the mutation positions were located in the vicinity of the heme pocket (see Fig. 4.4.5). Since it has been determined that the protein is slightly negatively charged at pH=7.0 (Zhao et al. 2012), it arises that all the above mutations correspond to an increase in the overall negative charge of the protein, except for N61K in which the total negative charge is decreased. As shown by Zhao et al (2012), these mutations result in a decrease in the catalytic efficiency of the enzyme, expressed as k_{cat}/K_m , except for N61K, which results in an increase in k_{cat}/K_m . This was rationalized by the observation that both enzyme and substrate are negatively charged, leading to diffusion-controlled kinetics (H. Ma et al. 2010), in which k_{cat}/K_m describes the efficiency of substrate approach to the enzyme (Zhao et al. 2012). As the catalytic efficiency increases significantly in higher ionic concentrations, when the negative charges of the enzyme and the substrate are masked, it was concluded that the process is electrostatically controlled (Zhao et al. 2012). Here, we test this conclusion with the aid of the VSE label.

4.4.1 FTIR spectra of MBN-labeled mutant and wild type DHP A

The FTIR absorption spectrum of labeled wild-type (WT) DHP A after baseline subtraction is shown in Figure 4.4.1. As KCN was added to the protein after protein purification and oxidation and before labeling with MBN, in order to ensure that the

heme remained in its ferric (oxidized) state (see section 3.3), a heme-bound cyanide stretching mode is detected at 2128.3 cm^{-1} . The nitrile stretch arising from the MBN label covalently bound to the only surface cysteine found in DHP A, i.e. Cys73, is seen at 2234.9 cm^{-1} . This frequency is characteristic of aromatic nitriles in a protic environment (Fafarman & Boxer 2010; Ghosh et al. 2009; Aschaffenburg & Moog 2009; Schkolnik, Salewski, et al. 2012), indicating that the MBN is exposed to the aqueous phase while attached to the protein surface. This is confirmed by MD simulations performed in our group, by Tillmann Utesch (unpublished data), for the labeled protein variants, see, e.g., Fig. 4.4.2. No signal that could be assigned to non-specifically bound MBN was detectable in any of the spectra. Each protein variant was measured five times, with a root mean standard deviation of $\pm 0.1\text{ cm}^{-1}$ for the reported peak frequencies.

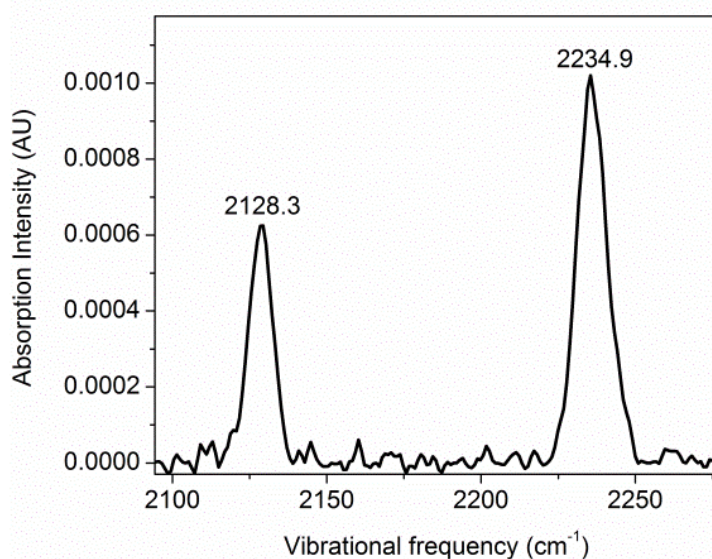


Figure 4.4.1. Baseline subtracted FTIR absorption spectrum of MBN-labeled wild type DHP A, displaying the heme-bound cyanide stretch at 2128.3 cm^{-1} , and the nitrile stretch of MBN covalently bound to C73, at 2234.9 cm^{-1} .

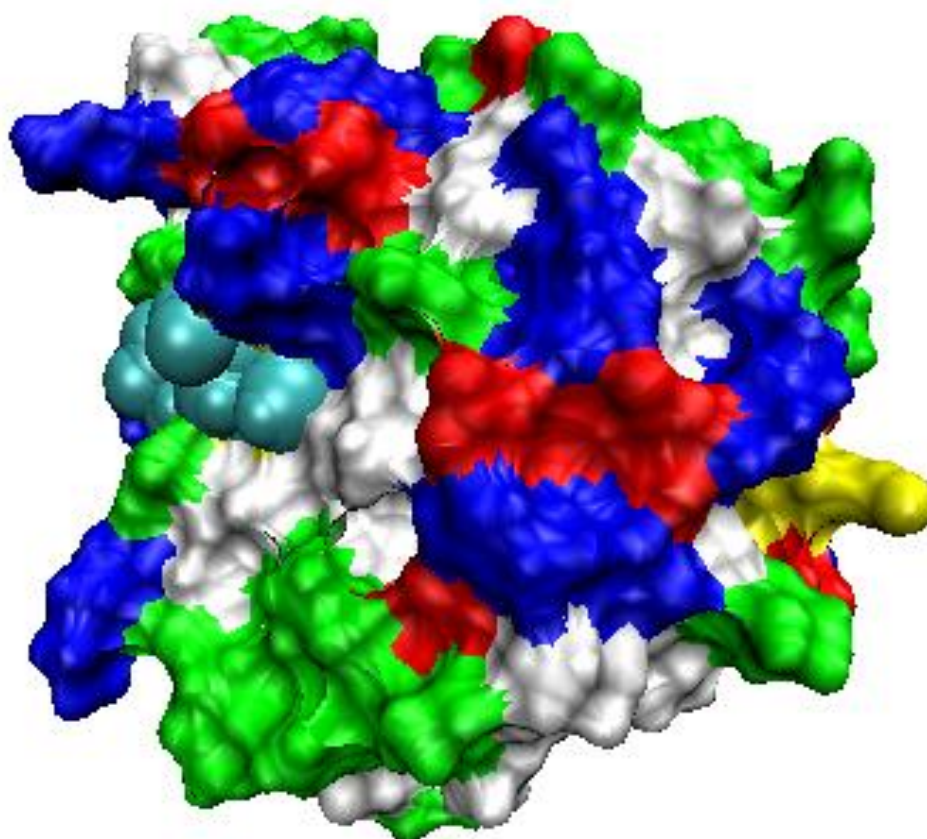


Figure 4.4.2. WT DHP A with MBN covalently bound to Cys 73 (yellow), and heme-bound cyanide (not seen. Heme appears in cyan). Color code: Blue/red – positively/negatively charged residues; Green/white – polar/non-polar residues. Snapshot from a 10 ns run performed by Tillmann Utesch. As seen, the MBN nitrile is exposed to the aqueous phase.

For all mutants, the single charge mutations were reflected by small but clearly detectable and statistically significant changes to the nitrile stretching frequency of the protein-bound MBN, in the mutants compared to WT DHP A. These frequency changes are inversely correlated to the square of the distance between the MBN nitrile bond and the mutation site (r^2), and linearly correlated to the protein dipole moment, both calculated by MD simulations. These correlations are presented in Figure 4.4.4 a and b, respectively. MD simulations were performed once for WT DHP A and for each of its mutants, with the exception of N61D, for which the simulation was run twice, for comparison. The figures contain both N61D runs, for reference. All MD simulations were performed for DHP A variants with a heme-bound cyanide and an MBN covalently

bound to Cys73. To stabilize the structure, His55 was protonated in the ϵ position, as arises from crystal structures (Thompson 2011). The correlations hold for all variants, except for the one with a charge mutation in position 36, a position that shows a much greater conformational flexibility than the other mutation positions, as reflected in the MD root mean square fluctuation (rmsf) graph shown in Fig. 4.4.3 (top). Since the electric field caused by a single charge varies proportionally to $1/r^2$, where r is the distance from the charge, the correlation between the changes in the MBN nitrile stretch frequency and this parameter indicates that the VSE probe can indeed sense the change to the protein electric field caused by a single charge mutation over considerable distances (21-38 Å). Such sensitivity on the nm range has also been shown in section 4.2. The observation that the MBN nitrile stretching frequency is linearly correlated to the protein dipole indicates that it reflects changes to overall protein electrostatics. These two last observations are strengthened by the negligible difference in the MBN nitrile stretching frequency observed for N61D and N61K in 150 mM potassium phosphate buffer (pH=7.0), as opposed to a 0.4 cm^{-1} frequency difference in 10 mM buffer. Since in a higher ionic strength there are more ions to mask the change in charge due to mutation at a distance of ca. 20 Å from the MBN nitrile, it is to be expected that at higher ionic strength the mutation would not be reflected in the MBN nitrile stretching frequency.

Eq. 4.3.1, i.e. $\nu = \nu_0 - \Delta\vec{\mu} \cdot \vec{F}$, can be used to determine the electric field experienced by the MBN nitrile, in the nitrile bond direction, for each DHP A variant. For ν_0 , 2233.3 cm^{-1} is used, following the results reported in section 4.1. The Stark tuning rate ($\Delta\mu$) used here for the protein-bound, buffer exposed MBN is $6.0 \cdot 10^{-9} \text{ cm}^{-1}/\text{V/m}$ as discussed in section 4.1. The electric fields calculated using these parameters range from $3.6 \cdot 10^8$ to $5.1 \cdot 10^8 \text{ V/m}$. All the above mentioned measured and calculated values appear in Table 4.4.1.

Table 4.4.1. MBN nitrile stretching frequencies, label distance from mutation site, protein dipole and electric fields obtained for the different DHP A variants.

DHP A variant ^a	ν_{MBN} (cm^{-1}) ^b	Protein dipole (D) ^c	d_{label} (\AA) ^d	Mut-C _(MBN) -N _(MBN) angle (deg) ^e	$E_{F,\text{MBN}}$ (V/m) ^f
WT	2234.9	260 ± 40			3.2·10 ⁸
R33Q	2236.1	270 ± 30	38 ± 1	142 ± 15	5.1·10 ⁸
K36A	2235.2	340 ± 20	36 ± 2	135 ± 18	3.6·10 ⁸
N61D	2235.5	360 ± 30	22 ± 2	118 ± 18	4.1·10 ⁸
N61K	2235.1	290 ± 30	25 ± 2	120 ± 20	3.4·10 ⁸
N96D	2235.9	370 ± 40	30 ± 1	152 ± 13	4.8·10 ⁸
N61D (KPB 150 mM)	2235.4				4.0·10 ⁸
N61K (KPB 150 mM)	2235.5				4.1·10 ⁸

^a Unless stated otherwise, measurements were performed at a potassium phosphate buffer concentration of 10 mM, pH=7.0. ^b MBN nitrile stretching frequency. Average over 5 measurements, root mean standard deviation = ±0.1 cm^{-1} . ^c Protein dipole, according to MD simulations. ^d Mutation site distance from MBN nitrile bond center, according to MD simulations. ^e Angle between the mutation site, the MBN carbon and the MBN nitrogen, from MD simulations. ^f Electric field at the MBN nitrile, in mean nitrile bond direction, calculated according to the linear terms of Eq. 2.6.1.

Table 4.4.2. Heme-CN stretching frequencies, distances and angles from mutation site.

DHP A variant ^a	$\nu_{\text{heme-CN}}$ (cm^{-1}) ^b	d_{label} (\AA) ^c	Mut-C-N angle (deg) ^d
WT	2128.4		
R33Q	2128.7	16 ± 1	70 ± 9
K36A	2128.1	9 ± 2	63 ± 11
N61D	2128.8	14 ± 1	74 ± 7
N61K	2128.2	15 ± 1	77 ± 10
N96D	2128.7	13 ± 1	118 ± 7
N61D (KPB 150 mM)	2127.8		
N61K (KPB 150 mM)	2128.0		

^a Unless stated otherwise, measurements were performed at a potassium phosphate buffer (KPB) concentration of 10 mM. ^b CN stretching frequency of the heme-bound cyanide (heme-CN). Average over 5 measurements, root mean standard deviation = ±0.1 cm^{-1} . ^c Mutation site distance from heme-bound CN bond center, according to MD simulations. ^d Angle between the mutation site, the heme-CN C atom and the heme-CN N atom, according to MD simulations (see fig. 4.4.3 bottom).

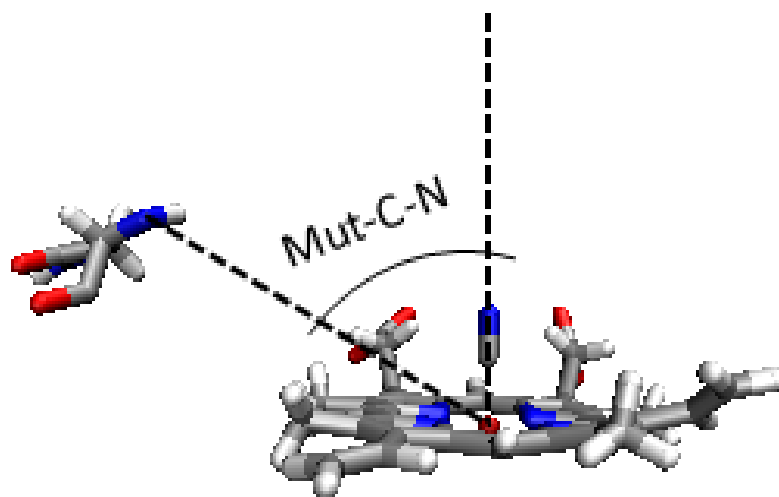
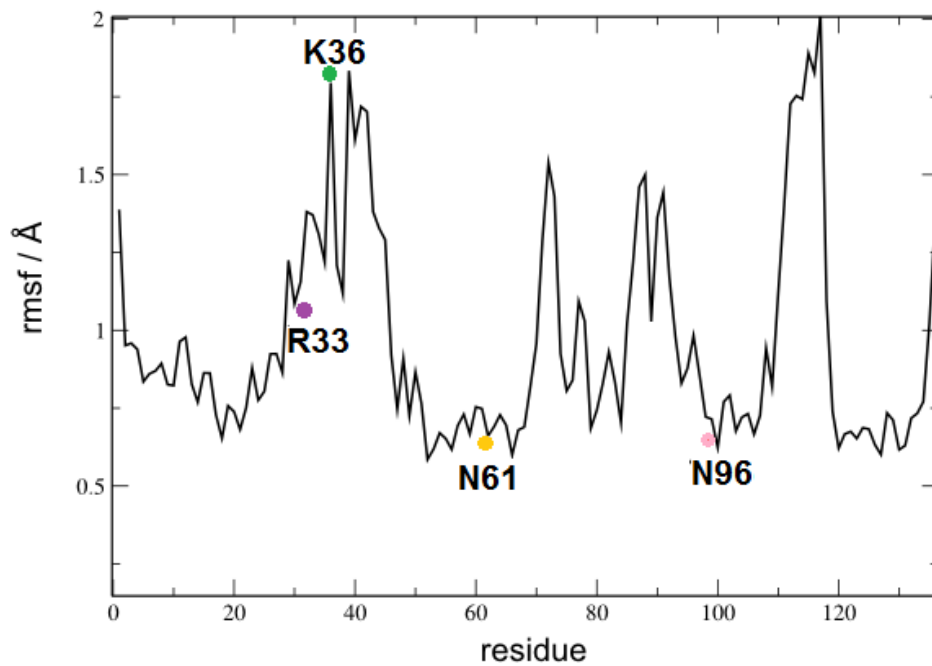


Figure 4.4.3. Top: rmsf for the different positions, from MD simulations performed for WT DHP A. **Bottom:** Snapshot of DHP A with CN at the heme and position 61 highlighted, in order to show the way the angle Mut-C-N (Table 4.4.2) was calculated.

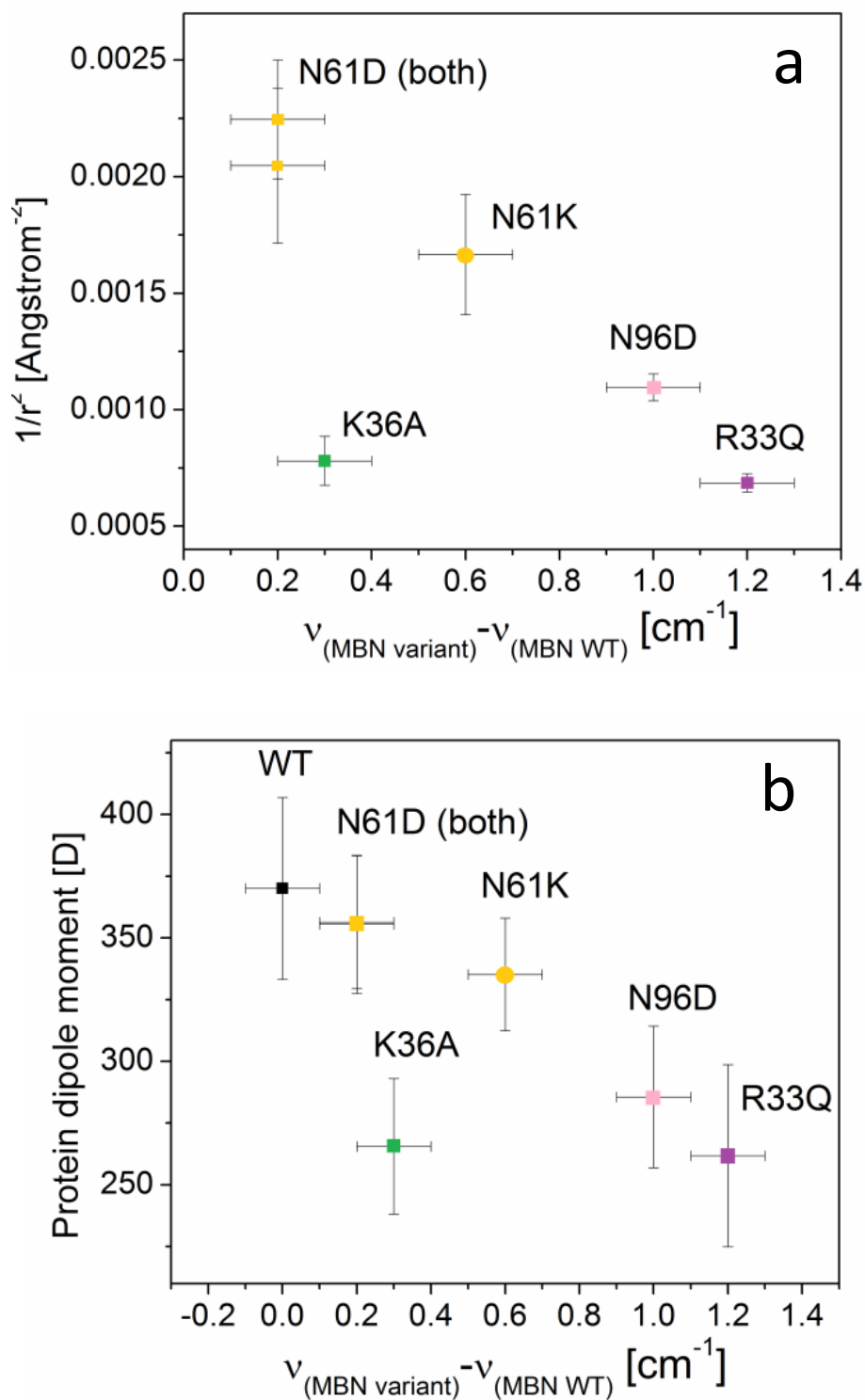


Figure 4.4.4. a) Variation of the difference of the nitrile stretch frequency between the mutants and the wild type protein with $1/r^2$, where r is the distance from the charge mutation site to the MBN nitrile bond, **b)** Protein dipole moment vs. the change in nitrile stretch frequency between the WT and variant proteins. All data refers to DHP A with heme-CN and MBN attached to Cys73. Frequencies were determined by FTIR, and the rest of the data was obtained by MD simulations.

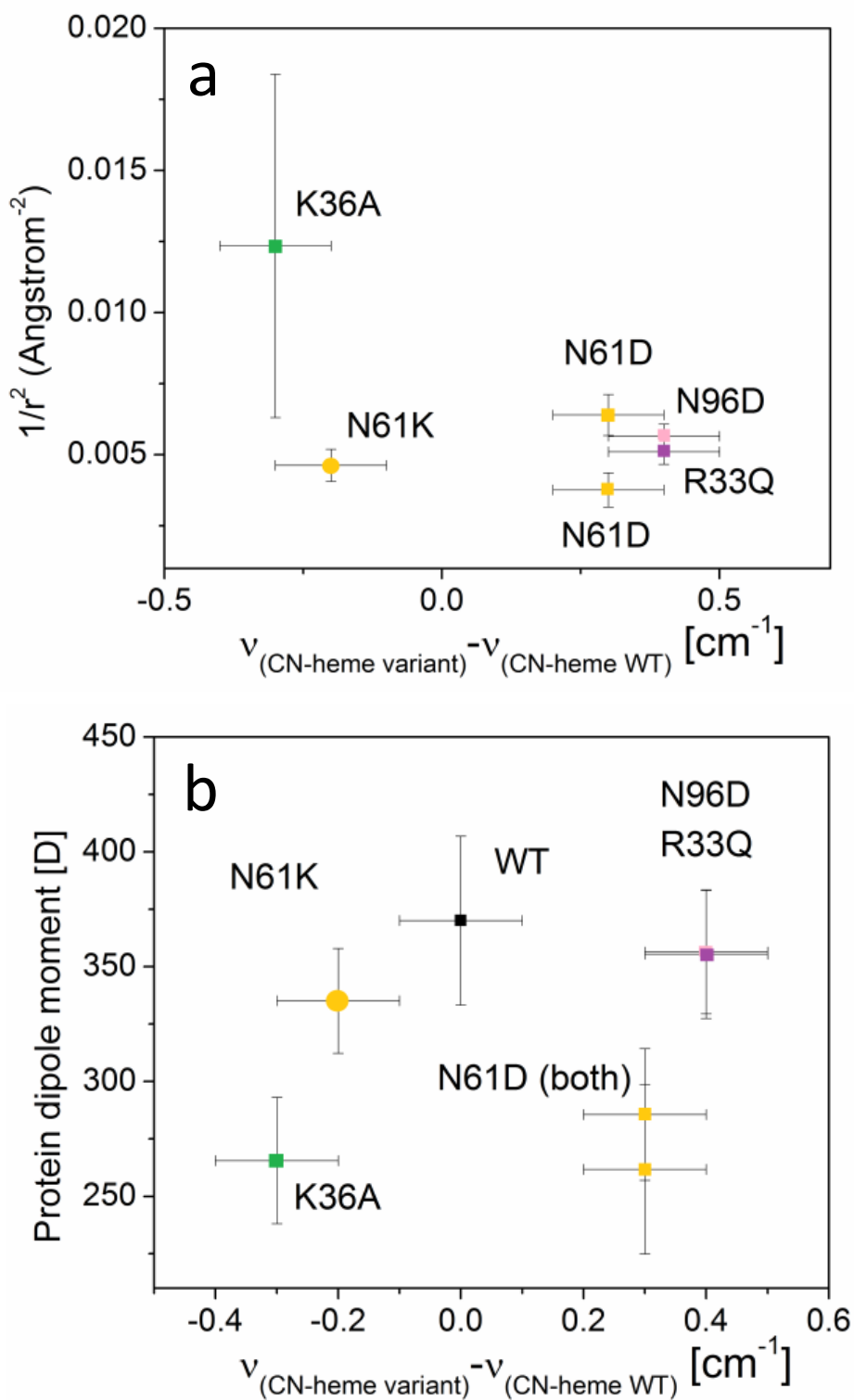


Figure 4.4.5. a) $1/r^2$, where r is the distance from the charge mutation site to the heme-bound cyanide (heme-CN) CN bond, vs. the change in CN stretch frequency between the WT and variant proteins. **b)** Protein dipole vs. the change in heme-CN stretch frequency between the WT and variant proteins. Frequencies were determined by FTIR, and the rest of the data was obtained by MD simulations.

It is interesting to note, that while the Stark tuning rate for heme-bound cyanide (hereafter heme-CN) is not expected to be significantly lower than that of MBN (Dalosto et al. 2004), the changes to its stretching frequency in the mutants compared to the WT protein are small relative to the changes observed for the MBN nitrile (See Table 4.4.2). Additionally, they do not correlate with either $1/r^2$, where r is the distance of the CN bond of the heme-CN from the charge mutation, nor with the protein dipole moment (See Figure 4.4.5). These observations are explained by the angle between the heme-CN nitrogen, its carbon and the mutation site (Mut-C-N angle, explained in fig. 4.4.3 bottom) predicted by MD simulations, and shown in Table 4.4.2. As these angles are close to 90° , the product of the scalar multiplication in Eq. 2.6.1 becomes small. Thereby, changes to the electric field due to charge mutations become smaller, and their dependence on r^2 or the protein dipole moment becomes statistically insignificant.

4.4.2 Connecting VSE and kinetic findings in DHP A

After it has been determined, with the aid of MD simulations, that the changes to the MBN-nitrile frequency in the charge mutants compared to the WT DHP A indeed reflect changes to overall protein electrostatics, one may compare the present findings to the kinetic data published by Zhao et al. (2012) for the same single-charge mutants. When plotting the frequency changes against the catalytic efficiency of the enzyme, determined by Zhao et al (2012) (Figure 4.4.6), a linear correlation is observed. The correlation between the catalytic efficiency (k_{cat}/K_m) and the MBN-nitrile vibrational frequency, which as explained above reflects the overall change in protein electrostatics, clearly indicates that the mutations investigated here preferentially affect the catalytic efficiency of DHP A by changing its overall electrostatics rather than by structural or functional alterations to the active site.

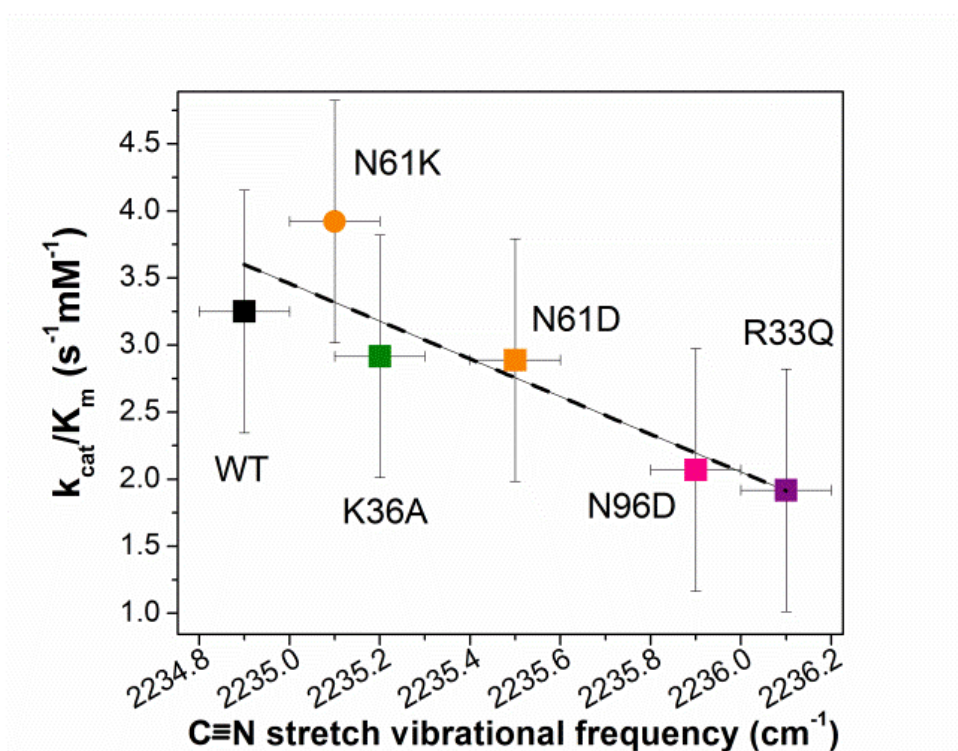
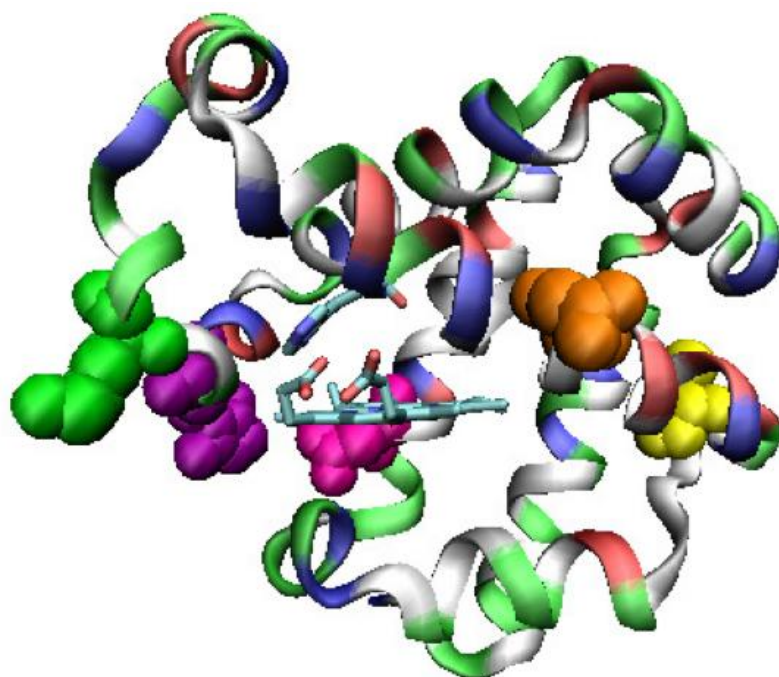


Figure 4.4.6. Top: DHP A with several positions highlighted [Crystal structure 3LB1 (Thompson, Davis, et al. 2010)]. Yellow: Cys 73, the MBN covalent-binding position. Mutation positions: 33 purple, 36 green, 61 orange, 96 pink. **Bottom:** $k_{\text{cat}}/K_{\text{m}}$ (catalytic efficiency) vs. the nitrile stretching frequency. The color code corresponds to the top figure. Orange circle: N61K, orange square: N61D and black square: WT DHP A. Dashed line: linear fit, $k_{\text{cat}}/K_{\text{m}}=3144.7-1.4\nu_0$, $R^2=0.73$.

Because in DHP A the rate of enzymatic turnover is controlled by diffusion, particularly at low substrate concentrations (Ma et al. 2010), the electrostatic effect observed here may be attributed to the potential experienced by the substrate as it approaches its as yet unknown surface binding site (Thompson, Franzen, et al. 2010). This observation is confirmed by the decrease in the catalytic efficiency of WT DHP A when the reaction is performed at a lower ionic strength, as reported by Zhao et al. (2012). Since DHP A is negatively charged at pH 7 (Zhao et al. 2012) a higher ionic strength decreases the mutual repulsion between enzyme and substrate. Further, the effect of charge mutations on the MBN nitrile stretching frequency sharply decreases upon increasing the buffer concentration from 10 mM to 150 mM (Table 4.4.1). It thus appears that ionic masking plays an important role in both DHP A kinetics and in the charge-mutation-induced change to the vibrational frequency of the VSE probe, confirming that enzyme kinetics are controlled by the electrostatic interaction between the charged substrate and the overall electric field of the enzyme.

This work demonstrates that VSE can be used to probe the effect of the overall protein electric field on an enzymatic process. Our results confirm the previously observed relation between DHP A kinetics and electrostatic changes due to charge mutations in the vicinity of its heme-pocket, while experimentally disentangling the role of protein electrostatics from possible mutation-induced structural and functional changes.

In a wider context, the present results suggest that electrostatic control may be an important factor in steering substrates towards enzyme active sites in biochemical pathways. The method presented here therefore can be useful in the future for the measurement of the effect of protein surface electrostatics on enzyme function, particularly in processes where the binding of a charged substrate may be a rate limiting step in the catalysis. Considering that many enzymes have charged substrates, such a method has potentially wide application in biophysics.

Conclusion

The vibrational Stark effect in nitriles has been, over the last decade, increasingly used to investigate electric fields in the active sites of proteins and enzymes. However, the use of this promising and versatile tool need not be confined to this purpose. The VSE, employing small probe molecules on the scale of only several Å in length, allows probing local electric fields at specific locations in various complex molecules and macromolecular systems. By covalently binding a Stark label to cysteine residues on protein surfaces, we have, in this work, been able to probe the electric fields on the surfaces of two proteins – cytochrome *c* and dehaloperoxidase A, and in the latter case, to draw conclusions as to the mechanism underlying the kinetics of the enzyme. Moreover, by attaching Stark-labeled cytochrome *c* mutants to a self assembled monolayer (SAM), we have been able to investigate SAM electrostatics and to identify limitations in an existing model that describes electrostatics at protein-coated SAMs. This finding may in the future help to develop better models and improve our understanding of interfacial electric fields. Such studies need not necessarily be restricted to proteins immobilized at SAM-coated electrodes, serving as rather crude biomimetic membrane models, but may further be extended to proteins embedded in phospholipid vesicles in solutions or in bilayer membranes on metal supports.

Further, the potential of VSE for the investigation of electrostatics does not start and end with protein-containing systems. We have shown that VSE probes can be both used to form SAMs and incorporated in existing SAMs, thus serving as a tool for studying electrostatics at the metal/SAM/solvent interface, an interface that thus far has posed great challenges for direct measurement, due to the many factors involved in its electrostatics, including the metal-SAM interaction, the SAM dipole and the SAM/solvent interfacial potential. By creating different Stark-probe containing SAMs and measuring the vibrational frequencies of the probe for different metals, solvents and applied potentials, and with the aid of an improved electrostatic model, we have been able to observe solvent orientation and to quantify electric fields and charge densities at the SAM-solution interface. Not less importantly, we have been able to determine the effective potential of zero charge of the SAM-modified metal, separating it from the contribution arising from the SAM-solution interfacial potential. Moreover, in the latter

work, as well as in the investigation which has utilized SAM-bound Stark-labeled cytochrome *c* to probe SAM electrostatics, we have demonstrated the great potential that surface enhanced vibrational spectroscopy in a spectro-electrochemical cell may hold for further VSE investigations.

To achieve all these results from the linear VSE, it has also been necessary to select appropriate values for $\Delta\mu$, the Stark tuning rate, and for ν_0 , the nitrile vibrational frequency in the absence of an electric field. Such parameters, specific for each system used in this work, have been obtained either by the analysis of previously published results (for $\Delta\mu$) or by the measurement of the variation in ν_0 under different conditions. The values derived for these parameters, although merely serving as tools for the achievement of more significant outcomes, as described above, are in themselves of great value for further research in the field of the nitrile-bond VSE, and will serve researchers in future VSE-based investigations of the electrostatics of different macromolecules and systems, and for the elucidation of electrostatically controlled reaction mechanisms.

Acknowledgements

For my achievements and the knowledge I have acquired during my doctoral studies I would like to thank Prof. Peter Hildebrandt and Prof. Stefan Franzen, my co-advisors, who have, in their very distinct ways, supported without pushing, imparted knowledge, helped form ideas and dealt with my temper.

I would also like to particularly thank Dr. Ingo Zebger who taught me how to perform IR spectroscopy and who was always there to help and guide – day or night, weekday or weekend; Dr. Diego Millo and Prof. Edmond Bowden who very patiently taught me everything I know about electrochemistry; and Dr. Matt Thompson, who together with Shu Jiang and Junjie Zhao from NCSU has taught me all about Dehaloperoxidase-hemoglobin A, and about protein production and purification.

For SERS measurements, for collaborating with me on my publications, for inspiring discussions and for his friendship I would like to thank Johannes Salewski. To Tillmann Utesch my ever-lasting gratitude for having saved me from having to perform MD simulations by myself and for his kind and friendly disposition. I likewise thank Francisco Velazquez Escobar for Raman measurements.

No less importantly, I would like to thank my colleagues and friends at the MVL: Wiebke Meister, Yvonne Rippers, Elisabeth Siebert, Sara Bruun, Jacek Kozuch and Murat Sezer; and from the IGRTG: Salome Patarai, Marco Mazza and Vashti. You all made work and life much more fun and inspiring.

I would like to thank Claudia Schulz, Marina Boettcher, Juergen Krauss, Lars Paasche, Khoa Ly and Simon Lappi for technical and administrative support, and for their friendly attitudes, kind help and endless patience.

Financial support by the German Research Foundation (DFG) in the framework of the IRTG 1524 is gratefully acknowledged, and no less important, the initiative, support and kindness of Prof. Martin Schoen, Dr. Daniela Fliegner and Petra Erdmann, who have made IGRTG 1524 happen and work, and who sent me to NCSU for an unforgettable period of full-throttle science and American culture.

Thank you all for everything! None of this would have been possible without you.

Bibliography

- Akinaga, Y., Nakajima, T. & Hirao, K., 2001. A density functional study on the adsorption of methanethiolate on the (111) surfaces of noble metals. *The Journal of Chemical Physics*, 114(19), p.8555.
- Albert L. Lehninger, 1970. *Biochemistry*, 2nd ed., New York: Worth Publishers.
- Alloway, D.M. et al., 2009. Tuning the Effective Work Function of Gold and Silver Using ω -Functionalized Alkanethiols: Varying Surface Composition through Dilution and Choice of Terminal Groups. *The Journal of Physical Chemistry C*, 113(47), pp.20328–20334.
- Andrews, S.S. & Boxer, S.G., 2000. Vibrational Stark Effects of Nitriles I. Methods and Experimental Results. *The Journal of Physical Chemistry A*, 104(51), pp.11853–11863.
- Aroca, R. & Price, B., 1997. A New Surface for Surface-Enhanced Infrared Spectroscopy : Tin Island Films. *The Journal of Physical Chemistry B*, 101(33), pp.6537–6540.
- Aschaffenburg, D.J. & Moog, R.S., 2009. Probing hydrogen bonding environments: solvatochromic effects on the CN vibration of benzonitrile. *The journal of physical chemistry. B*, 113(38), pp.12736–43.
- Ataka, K. & Heberle, J., 2007. Biochemical applications of surface-enhanced infrared absorption spectroscopy. *Analytical and bioanalytical chemistry*, 388(1), pp.47–54.
- Ballav, N. et al., 2007. Direct probing molecular twist and tilt in aromatic self-assembled monolayers. *Journal of the American Chemical Society*, 129(50), pp.15416–7.
- Bjerke, A.E. et al., 1999. Surface-Enhanced Infrared Absorption of CO on Platinized Platinum. *Analytical Chemistry*, 71(10), pp.1967–1974.
- de Boer, B. et al., 2005. Tuning of Metal Work Functions with Self-Assembled Monolayers. *Advanced Materials*, 17(5), pp.621–625.
- Boxer, S.G., 2009. Stark Realities. *The Journal of Physical Chemistry B*, 113(10), pp.2972–2983.
- Brewer, S.H. & Franzen, S., 2003. A quantitative theory and computational approach for the vibrational Stark effect. *The Journal of Chemical Physics*, 119(2), pp.851–856.
- Bublitz, G.U. & Boxer, S.G., 1997. Stark spectroscopy: applications in chemistry, biology, and materials science. *Annual review of physical chemistry*, 48, pp.213–42.
- Bushnell, G.W., Louie, G.V. & Brayer, G.D., 1990. High-resolution three-dimensional structure of horse heart cytochrome c. *Journal of Molecular Biology*, 214(2), pp.585–595.
- Chapman, R.G. et al., 2000. Preparation of Mixed Self-Assembled Monolayers (SAMs) That Resist Adsorption of Proteins Using the Reaction of Amines with a SAM That Presents Interchain Carboxylic Anhydride Groups. *Langmuir*, (16), pp.6927–6936.
- Cho, H.G., Cheong, B.S. and Kim, K.W., 1998. Vibrational Spectroscopy of C-N Stretch in Mixtures of Deuterated Acetonitrile and Methanol. *Bull. Korean Chem. Soc.*, 19(9), pp.909–910.

- Dalosto, S.D., Vanderkooi, J.M. & Sharp, K.A, 2004. Vibrational Stark Effects on Carbonyl, Nitrile, and Nitrosyl Compounds Including Heme Ligands, CO, CN, and NO, Studied with Density Functional Theory. *The journal of physical chemistry B*, 108(20), pp.6450–7.
- Demoz, A. & Harrison, D.J., 1993. Characterization of Extremely Low Defect Density Hexadecanethiol Monolayers on Hg Surfaces. *Langmuir*, (9), pp.1046–1050.
- Ehler, T.T., Malmberg, N. & Noe, L.J., 1997. Characterization of Self-Assembled Alkanethiol Monolayers on Silver and Gold Using Surface Plasmon Spectroscopy. *The journal of physical chemistry B*, 101(8), pp.1268–1272.
- Emets, V.V. & Damaskin, B.B., 2009. The relation between the potential of zero charge and work function for *sp*-metals. *Russian Journal of Electrochemistry*, 45(1), pp.45–57.
- Fafarman, A.T. et al., 2010. Decomposition of vibrational shifts of nitriles into electrostatic and hydrogen-bonding effects. *Journal of the American Chemical Society*, 132(37), pp.12811–3.
- Fafarman, A.T. et al., 2012. Quantitative, directional measurement of electric field heterogeneity in the active site of ketosteroid isomerase. *Proceedings of the National Academy of Sciences of the United States of America*, 109(6), pp.E299–308.
- Fafarman, A.T. et al., 2006. Site-specific conversion of cysteine thiols into thiocyanate creates an IR probe for electric fields in proteins. *Journal of the American Chemical Society*, 128(41), pp.13356–7.
- Fafarman, A.T. & Boxer, S.G., 2010. Nitrile bonds as infrared probes of electrostatics in Ribonuclease S. *The journal of physical chemistry B*, 114(42), pp.13536–44.
- Franzen, S., 2002. An electrostatic model for the frequency shifts in the carbonmonoxy stretching band of myoglobin: correlation of hydrogen bonding and the Stark tuning rate. *Journal of the American Chemical Society*, 124(44), pp.13271–81.
- Frey, S. et al., 2001. Structure of Thioaromatic Self-Assembled Monolayers on Gold and Silver. *Langmuir*, 17(8), pp.2408–2415.
- Gershevit, O. & Sukenik, C.N., 2004. In situ FTIR-ATR analysis and titration of carboxylic acid-terminated SAMs. *Journal of the American Chemical Society*, 126(2), pp.482–3.
- Ghosh, A. et al., 2009. 2D IR photon echo spectroscopy reveals hydrogen bond dynamics of aromatic nitriles. *Chemical physics letters*, 469(4-6), pp.325–330.
- Goormaghtigh, E., Raussens, V. & Ruysschaert, J., 1999. Attenuated total reflection infrared spectroscopy of proteins and lipids in biological membranes. *Biochimica et Biophysica Acta*, 1422, pp.105-185.
- Hallmann, L. et al., 2008. Self-assembled monolayers of benzylmercaptan and p-cyanobenzylmercaptan on Au(111) surfaces: structural and spectroscopic characterization. *Langmuir*, 24(11), pp.5726–33.
- Hamoudi, H. et al., 2011. Orbital-Dependent Charge Transfer Dynamics in Conjugated Self-Assembled Monolayers. *Physical Review Letters*, 107(2), pp.1–5.

- Han, S.W., Lee, S.J. & Kim, K., 2001. Self-Assembled Monolayers of Aromatic Thiol and Selenol on Silver: Comparative Study of Adsorptivity and Stability. *Langmuir*, 17(22), pp.6981–6987.
- Haynes, C.L., Mcfarland, A.D. & van Duyne, R.P., 2005. Surface Enhanced Raman Spectroscopy. *Analytical chemistry*, pp. 338A-346A.
- Heimel, G. et al., 2008. The interface energetics of self-assembled monolayers on metals. *Accounts of chemical research*, 41(6), pp.721–9.
- Heimel, G. et al., 2007. Toward control of the metal-organic interfacial electronic structure in molecular electronics: a first-principles study on self-assembled monolayers of pi-conjugated molecules on noble metals. *Nano letters*, 7(4), pp.932–40.
- Hoffmann, F.M., 1983. Infrared Reflection-Absorption Spectroscopy of Adsorbed Molecules. *Surface Science Reports*, 3, pp.107–192.
- Jiang, P. et al., 2009. STM imaging ortho- and para-fluorothiophenol self-assembled monolayers on Au(111). *Langmuir*, 25(9), pp.5012–7.
- Jo, H. et al., 2010. Selective incorporation of nitrile-based infrared probes into proteins via cysteine alkylation. *Biochemistry*, 49(49), pp.10354–6.
- Käfer, D. et al., 2007. Interplay of Anchoring and Ordering in Aromatic Self-Assembled Monolayers. *The Journal of Physical Chemistry C*, 111, pp.10546–10551.
- Friedrich Siebert & Peter Hildebrandt, 2008, *Vibrational Spectroscopy in Life Science*, Weinheim: Wiley VCH Verlag.
- Laibnis, P.E. et al., 1991. Comparison of the Structures and Wetting Properties of Self-Assembled Monolayers of *n*-Alkanethiols on the Coinage Metal Surfaces, Cu, Ag, Au. *Journal of American Chemical Society*, 113, pp.7152–7167.
- Lebioda, L. et al., 1999. An enzymatic globin from a marine worm. *Nature*, 401, p.445.
- Lecomte, J.T.J., Vuletich, D.A. & Lesk, A.M., 2005. Structural divergence and distant relationships in proteins: evolution of the globins. *Current opinion in structural biology*, 15(3), pp.290–301.
- Leopold, M.C., 2000. *Interfacial investigations of a biological electron transfer model: cytochrome c adsorbed on gold electrodes modified with self-assembled monolayers*. PhD dissertation, North Carolina State University.
- Levinson, N.M., Fried, S.D. & Boxer, S.G., 2012. Solvent-Induced Infrared Frequency Shifts in Aromatic Nitriles Are Quantitatively Described by the Vibrational Stark Effect. *The journal of physical chemistry B*, 116 (35), pp.10470–10476.
- Lorenz, L., 2004. Schwingungsspektroskopische Untersuchung von selbstorganisierten Monoschichten aus bifunktionellen Thiolen. Master's thesis, Technische Universitaet Berlin.
- Love, J.C. et al., 2005. Self-assembled monolayers of thiolates on metals as a form of nanotechnology. *Chemical reviews*, 105(4), pp.1103-1169.

- Lu, G.Q. et al., 2000. In Situ FTIR Spectroscopic Studies of Adsorption of CO, SCN⁻, and Poly(o-phenylenediamine) on Electrodes of Nanometer Thin Films of Pt, Pd, and Rh: Abnormal Infrared Effects (AIREs). *Langmuir*, 16(2), pp.778–786.
- Ly, H.K. et al., 2011. Surface-enhanced vibrational spectroscopy for probing transient interactions of proteins with biomimetic interfaces: electric field effects on structure, dynamics and function of cytochrome *c*. *The FEBS journal*, 278(9), pp.1382–90.
- Ma, F. & Lennox, R.B., 2000. Potential-Assisted Deposition of Alkanethiols on Au : Controlled Preparation of Single- and Mixed-Component SAMs. *Langmuir*, (16), pp.6188–6190.
- Ma, H. et al., 2010. Kinetic analysis of a naturally occurring bioremediation enzyme: dehaloperoxidase-hemoglobin from *Amphitrite ornata*. *The journal of physical chemistry B*, 114(43), pp.13823–9.
- Mathews, C.K., van Holde, K.E., Appling, 2012. *Biochemistry*, Prentice Hall.
- Meunier-Prest, R. et al., 2010. Potential-assisted deposition of mixed alkanethiol self-assembled monolayers. *Electrochimica Acta*, 55(8), pp.2712–2720.
- Miyake, H., Ye, S. & Osawa, M., 2002. Electroless deposition of gold thin films on silicon for surface-enhanced infrared spectroelectrochemistry. *Electrochemistry Communications*, 4(12), pp.973–977.
- Murgida, D.H. & Hildebrandt, P., 2001. Heterogeneous Electron Transfer of Cytochrome *c* on Coated Silver Electrodes. Electric Field Effects on Structure and Redox Potential. *The Journal of Physical Chemistry B*, 105, pp.1578–1586.
- Murgida, D.H. & Hildebrandt, P., 2005. Redox and redox-coupled processes of heme proteins and enzymes at electrochemical interfaces. *Physical chemistry chemical physics*, 7(22), pp.3773–84.
- Natan, A. et al., 2007. Electrostatic Properties of Ideal and Non-ideal Polar Organic Monolayers: Implications for Electronic Devices. *Advanced Materials*, 19(23), pp.4103–4117.
- Natan, A. et al., 2006. Cooperative effects and dipole formation at semiconductor and self-assembled-monolayer interfaces. *Physical Review B*, 73(19), pp.1–4.
- Natan, A., Kuritz, N. & Kronik, L., 2010. Polarizability, Susceptibility, and Dielectric Constant of Nanometer-Scale Molecular Films: A Microscopic View. *Advanced Functional Materials*, 20(13), pp.2077–2084.
- Oklejas, V. & Harris, J.M., 2003. In-Situ Investigation of Binary-Component Self-Assembled Monolayers: A SERS-Based Spectroelectrochemical Study of the Effects of Monolayer Composition on Interfacial Structure. *Langmuir*, 19(14), pp.5794–5801..
- Osawa, M., 2001. Surface-Enhanced Infrared Absorption. In S. Kawata. (Ed.): *Near-Field Optics and Surface Plasmon Polaritons*, pp. 163–187. Springer-Verlag Berlin.

- Osawa, M., Ataka, K.I. Yoshii, K. & Nishikawa, Y., 1993. Surface-Enhanced Infrared Spectroscopy: The Origin of the Absorption Enhancement and Band Selection Rule in the Infrared Spectra of Molecules Adsorbed on Fine Metal Particles. *Applied Spectroscopy*, 47(9), pp.1497–1502.
- Paoli, M., Marles-Wright, J. & Smith, A., 2002. Structure-function relationships in heme-proteins. *DNA and cell biology*, 21(4), pp.271–80.
- Pflaum, J. et al., 2002. Structure and electronic properties of CH₃- and CF₃- terminated alkanethiol monolayers on Au (111): a scanning tunneling microscopy, surface X-ray and helium scattering study. *Surface Science*, 498, pp.89–104.
- Ramírez, P. et al., 2007. Determination of the potential of zero charge of Au(111) modified with thiol monolayers. *Analytical chemistry*, 79(17), pp.6473–9.
- Reimers, J.R. & Hush, N.S., 1999. Vibrational Stark Spectroscopy 3. Accurate Benchmark ab Initio and Density Functional Calculations for CO and CN-. *The Journal of Physical Chemistry A*, 103(49), pp.10580–10587.
- Samanta, D. & Sarkar, A., 2011. Immobilization of bio-macromolecules on self-assembled monolayers: methods and sensor applications. *Chemical Society reviews*, 40(5), pp.2567–92.
- Schalnat, M.C. & Pemberton, J.E., 2010. Comparison of a fluorinated aryl thiol self-assembled monolayer with its hydrogenated counterpart on polycrystalline Ag substrates. *Langmuir*, 26(14), pp.11862–9.
- Schkolnik, G., Utesch, T., et al., 2012. Mapping local electric fields in proteins at biomimetic interfaces. *Chemical communications*, 48(1), pp.70–2.
- Schkolnik, G., Salewski, J., et al., 2012. Vibrational Stark Effect of the Electric-Field Reporter 4-Mercaptobenzonitrile as a Tool for Investigating Electrostatics at Electrode/SAM/Solution Interfaces. *International journal of molecular sciences*, 13(6), pp.7466–82.
- Schlenoff, J.B., Li, M. & Ly, H., 1995. Stability and Self-Exchange in Alkanethiol Monolayers. *Journal of American Chemical Society*, 117(23), pp.12528–12536.
- Schmidt, M., 2006. Surface-enhanced infrared absorption spectroscopy of self-assembled protein monolayers on gold nano-structures. Diploma thesis, Albert-Ludwigs-Universitaet Freiburg.
- Sezer, M. et al., 2012. Analyzing the catalytic processes of immobilized redox enzymes by vibrational spectroscopies. *IUBMB life*, 64(6), pp.455–64.
- Shaw, S.K. et al., 2009. Sum-frequency spectroscopy of molecular adsorbates on low-index Ag surfaces: effects of azimuthal rotation. *Analytical chemistry*, 81(3), pp.1154–61.
- Sivanesan, A. et al., 2011. Functionalized Ag nanoparticles with tunable optical properties for selective protein analysis. *Chemical communications*, 47(12), pp.3553–5.

- Smith, C.P. & White, H.S., 1992. Theory of the interfacial potential distribution and reversible voltammetric response of electrodes coated with electroactive molecular films. *Analytical chemistry*, 64(20), pp.2398–405.
- Stein, S.E., 2003. Infrared Spectra. In W. G. Linstrom, P.J., Mallard, ed. *NIST Chemistry WebBook, NIST Standard Reference Database Number 69*. National Institute of Standards and Technology: Gaithersburg, MD, USA.
- Stoner, E.C., 1945. The demagnetizing factors for ellipsoids. *Philosophical Magazine*, 36(263), pp.803–821.
- Suydam, I.T. et al., 2006. Electric fields at the active site of an enzyme: direct comparison of experiment with theory. *Science*, 313, pp.200–4.
- Suydam, I.T. & Boxer, S.G., 2003. Vibrational Stark effects calibrate the sensitivity of vibrational probes for electric fields in proteins. *Biochemistry*, 42(41), pp.12050–5.
- Thompson, M.K., Franzen, S., et al., 2010. Compound ES of Dehaloperoxidase Decays via Two Distal Histidine. *Journal of American Chemical Society*, 132, pp.17501–17510.
- Thompson, M.K. et al., 2011. Dehaloperoxidase-hemoglobin from *Amphitrite ornata* is primarily a monomer in solution. *The journal of physical chemistry B*, 115(14), pp.4266–72.
- Thompson, M.K., 2011. Distal Histidine Flexibility as the Key to Reactivity in Dehaloperoxidase-Hemoglobin from *Amphitrite ornata*. PhD thesis, State University of North Carolina.
- Thompson, M.K., Davis, M.F., et al., 2010. Internal binding of halogenated phenols in dehaloperoxidase-hemoglobin inhibits peroxidase function. *Biophysical journal*, 99(5), pp.1586–95.
- Trasatti, S., 1971. Work function, electronegativity, and electrochemical behaviour of metals ii. Potentials of zero charge and "electrochemical" work functions. *Electroanalytical Chemistry and Interfacial Electrochemistry*, 33, pp.351–378.
- Trasatti, S., 1984. Prediction of double layer parameters the case of silver I. *Journal of Electroanalytical Chemistry*, 172, pp.27–48.
- Tucker, M.J. et al., 2004. A new method for determining the local environment and orientation of individual side chains of membrane-binding peptides. *Journal of the American Chemical Society*, 126(16), pp.5078–9.
- Valette, G., 1982. Hydrophilicity of metal surfaces - Silver, Gold and Copper electrodes. *Journal of Electroanalytical Chemistry*, 139, pp.285–301.
- Walczak, M.M. et al., 1991. Structure and Interfacial Properties of Spontaneously Adsorbed n-Alkanethiolate Monolayers on Evaporated Silver Surfaces. *Journal of American Chemical Society*, 113, pp.2370–2378.
- Wan, L.J. et al., 2000. Molecular Orientation and Ordered Structure of Benzenethiol Adsorbed on Gold(111). *The Journal of Physical Chemistry B*, 104(15), pp.3563–3569.

- Wang, L. et al., 2009. Electronic Structure of Self-Assembled Monolayers on Au(111) Surfaces: The Impact of Backbone Polarizability. *Advanced Functional Materials*, 19(23), pp.3766–3775.
- White, H.S. et al., 1998. Voltammetric Measurement of Interfacial Acid/Base Reactions. *The Journal of Physical Chemistry B*, 102, pp.2930–2934.
- Wisitruangsakul, N. et al., 2008. Redox-linked protein dynamics of cytochrome c probed by time-resolved surface enhanced infrared absorption spectroscopy. *Physical chemistry chemical physics*, 10(34), pp.5276–86.
- Xu, J. & Bowden, E.F., 2006. Determination of the orientation of adsorbed cytochrome C on carboxyalkanethiol self-assembled monolayers by in situ differential modification. *Journal of the American Chemical Society*, 128(21), pp.6813–22.
- Xu, L., Cohen, A.E. & Boxer, S.G., 2011. Electrostatic fields near the active site of human aldose reductase: 2. New inhibitors and complications caused by hydrogen bonds. *Biochemistry*, 50(39), pp.8311–22.
- Zhao, J. et al., 2012. Study of the electrostatic effects of mutations on the surface of dehaloperoxidase-hemoglobin A. *Biochemical and biophysical research communications*, 420(4), pp.733–7.